

Fluctuation Driven Phenomena in Ultracold Spinor Bose Gas

by

Junliang Song

B. Sc., Peking University, 2004

M. Phil., The Chinese University of Hong Kong, 2006

A THESIS SUBMITTED IN PARTIAL FULFILLMENT OF
THE REQUIREMENTS FOR THE DEGREE OF

DOCTOR OF PHILOSOPHY

in

The Faculty of Graduate Studies

(Physics)

THE UNIVERSITY OF BRITISH COLUMBIA

(Vancouver)

April 2010

© Junliang Song 2010

Abstract

In this thesis, we have investigated several fluctuation-driven phenomena in ultracold spinor Bose gases. In Bose-Einstein condensates of hyperfine spin-two ($F=2$) atoms, it is shown that zero-point quantum fluctuations completely lift the accidental continuous degeneracy in quantum spin nematic phases predicted by mean field analysis, and these fluctuations select out two distinct spin nematic states with higher symmetries. It is further shown that fluctuations can drive a novel type of coherent spin dynamics which is very sensitive to the variation of quantum fluctuations controlled by magnetic fields or potential depths in optical lattices. These results have indicated fundamental limitations of precision measurements based on mean field theories. In addition, fluctuation-driven coherent spin dynamics studied here is a promising tool to probe correlated fluctuations in many body systems. In another system – a two-dimension superfluid of spin-one ($F=1$) ^{23}Na atoms – we have investigated spin correlations associated with half quantum vortices. It is shown that when cold atoms become superfluid below a critical temperature a unique nonlocal topological order emerges simultaneously due to fluctuations in low dimensional systems. Our simulation have indicated that there exists a nonlocal softened π -spin disclination structure associated with a half-quantum vortex although spin correlations are short ranged. We have also estimated fluctuation-dependent critical frequencies for half-quantum vortex nucleation in rotating optical traps. These results indicate that the strongly fluctuating ultracold spinor system is a promising candidate for studying topological orders that are the focus of many other fields.

Table of Contents

Abstract	ii
Table of Contents	iii
List of Tables	vi
List of Figures	vii
Acknowledgements	ix
Dedication	x
1 Introduction	1
1.1 Fluctuations in a Harmonic Oscillator and Beyond	3
1.2 Fluctuation-Driven Phenomena	6
1.3 Bose-Einstein Condensates of Ultracold Atoms	9
1.4 Ultracold Spinor Condensates	13
1.5 Organization of the Thesis	20
2 Interatomic Interactions and Low-Energy Scattering	21
2.1 Interatomic Interactions	21
2.2 Low Energy Scattering	24
2.3 Interactions with Hyperfine Spin Degrees of Freedom	25
2.4 Vector and Tensor Algebra and Representations	27
2.4.1 $F=1$	28
2.4.2 $F=2$	29
2.5 Linear and Quadratic Zeeman Shift	32
3 Fluctuation-Induced Uniaxial and Biaxial Nematic States in $F = 2$ Spinor Condensates	35
3.1 Introduction	35
3.2 Mean Field Theory of $F=2$ Condensates	36
3.2.1 Ferromagnetic States	38

Table of Contents

3.2.2	Cyclic States	38
3.2.3	Nematic States	40
3.3	Zero-Point Quantum Fluctuations	42
3.4	Uniaxial and Biaxial Spin Nematic States	45
3.5	Discussion and Conclusion	46
4	Quantum Fluctuation Controlled Coherent Spin Dynamics in $F=2$ ^{87}Rb Condensates	48
4.1	Introduction	48
4.2	Microscopic Hamiltonian for $F = 2$ ^{87}Rb in Optical Lattices	50
4.3	Range of Interaction Parameters for the Lattice Hamiltonian	51
4.4	Mean Field Nematic States and Coherent Dynamics	54
4.5	Effective Hamiltonian for QFCSD	55
4.5.1	Nematic Manifold	55
4.5.2	Collective Coordinates and Conjugate Momentum	57
4.5.3	Spectra of Collective Modes	58
4.5.4	Effective Hamiltonian	59
4.6	Potentials Induced by Quantum Fluctuations	61
4.7	Oscillations Induced by Quantum Fluctuations	64
4.8	Effects of Thermal Fluctuations	70
4.9	Effects of Spin Exchange Losses	72
4.10	Estimates of Condensate Fraction	77
4.11	Conclusion	79
5	Half Quantum Vortex (HQV) in $F = 1$ Superfluids of Ultra- cold Atoms	81
5.1	Introduction	81
5.2	HQV in Spinor Bose-Einstein Condensates	82
5.2.1	Magnetic Properties and Energetics of HQV	83
5.2.2	HQV Lattice in Rotating Traps	89
5.3	HQV in 2D Superfluid of Ultracold $F = 1$ Atoms	93
5.3.1	Effective Hamiltonian	93
5.3.2	HQV and Topological Order - A Gauge Field Description	95
5.3.3	HQV and Topological Order - Monte Carlo Simulations	101
5.3.4	Critical Frequency for HQV Nucleation	104
5.4	Conclusion	107
6	Conclusion	108

Table of Contents

Bibliography 110

Appendices

A Band Structure in Optical Lattices 124

B The β -function of the Nonlinear Sigma Model 127

List of Tables

2.1	Scattering lengths (in atomic units) of various alkali atoms. . .	26
3.1	Magnetic orderings in mean field ground states of $F = 2$ spinor condensates.	37
3.2	Scattering lengths (in atomic units) of various alkali isotopes with hyperfine spin $F = 2$	38
3.3	Collective modes of nematic states specified by ξ	43

List of Figures

2.1	Interaction energy of two ^{85}Rb atoms as a function of inter-nuclear distance r	23
2.2	Hyperfine energy levels of a ^{87}Rb atom in its electronic ground state.	33
3.1	Wavefunctions of spin nematics and phase diagram of $F = 2$ spinor condensates	39
3.2	The zero-point energy of spin nematics per lattice site as a function of ξ	44
4.1	Coupling constants in optical lattices.	52
4.2	An artistic view of the five-dimension manifold of spin nematics.	56
4.3	Barrier height B_{qf} (in units of pK) as a function of optical potential depth V	62
4.4	Effective potential as a function of ξ for various experimental parameters.	63
4.5	Fluctuation-driven coherent spin dynamics when the quadratic Zeeman coupling is absent.	64
4.6	Fluctuation-driven coherent spin dynamics around various spin nematic states at the presence of the quadratic Zeeman coupling.	67
4.7	Fluctuation-driven coherent spin dynamics around biaxial spin nematic states at the presence of the quadratic Zeeman coupling.	68
4.8	Stability of fluctuation-driven coherent spin dynamics	69
4.9	Induced free energy barrier height as a function of temperature for different lattice potentials.	73
4.10	Estimated time evolution of rubidium population at $ 2, 0\rangle$ hyperfine spin state when the quadratic Zeeman coupling or Zeeman field varies.	74
4.11	Estimated time evolution of population at $ 2, 0\rangle$ state at different temperatures.	76

List of Figures

4.12	Condensation fraction versus optical lattice potential depth V (in units of E_R).	78
5.1	Two quantum vortices separated at a distance of d	84
5.2	Magnetic structure of an individual half quantum vortex and interaction energy between two half quantum vortices	86
5.3	Creation of a half quantum vortex in rotating traps	90
5.4	Dynamical creation of half quantum vortex lattice in rotating traps	92
5.5	Numerical solution to the self-consistent equation Eq.5.34	98
5.6	A half quantum vortex in the Z_2 lattice gauge field model.	100
5.7	Correlations and loop integrals in 2D nematic superfluids	102
5.8	Free energy and creation of half quantum vortex in rotating traps	105

Acknowledgements

First and foremost, I would like to thank my supervisor Fei Zhou for his constant guidance and patience over the past four years. He has led me into this fascinating research field of cold atomic gases. I have been fortunate to work with someone with ability and integrity as Fei. He has always been my source of inspiration and encouragement for research and life.

I would like to thank the members of my committee: Kirk Madison, David Jones, Moshe Rozali and George Sawatzky for their helpful suggestions of improving the thesis and my oral presentation. I owe particular thanks to Kirk Madison for his careful proofreading of my thesis and thoughtful comments on experimental issues.

I would like to thank my collaborators: Gordon Semenoff, Wu-Min Liu, An-Chun Ji for their important contributions to this thesis. I would also like to thank Tin-Lun Ho, Xiaoling Cui, Michiel Snoek, Hui Zhai for their valuable suggestions and stimulating discussions. I am grateful to the people in the Physics and Astronomy department at University of British Columbia, for providing a pleasant and supportive atmosphere to work in.

I would like to thank my loving family and my wonderful friends. As always, my deepest thanks are owed to my parents, who have supported me throughout my years of education.

During the workshop on condensed matter physics of cold atoms at Beijing in 2009, I was supported by the Kavli Institute for Theoretical Physics China under the visiting graduate student fellowship.

Dedication

To my parents

Chapter 1

Introduction

Fluctuation, or to shift back and forth irregularly, is one the most common phenomena in the physical world. For example, the sea level rises and falls every day, the temperature of our earth varies wildly in the last decade. It seems that nothing stands still and everything fluctuates. According to the laws of modern physics, this is indeed the case since fluctuation is believed to be an intrinsic nature of all physical systems. For example, the density at any point inside a cup of hot water can not remain constant, although the amount of variation might be small. The density fluctuation is caused by the thermal movement of the constituent molecules and can only be suppressed by decreasing the water's temperature. One would expect that fluctuations can be eliminated when the temperature goes down to the absolute zero where everything is supposed to be still. However, even in this limit the molecules, as well as any other particles, are never at rest: they are in a seemingly random motion called "zero-point motion", as a direct consequence of the Heisenberg uncertainty principle of quantum mechanics[1]. Not only particles fluctuate as their positions and velocities are not definite, the vacuum which assumed to be empty of matter and energy also fluctuates. Physicists picture the vacuum as a sea with fluctuating foam of virtual particles which are repeatedly created and annihilated spontaneously. And according to modern cosmology, even our whole universe is fluctuating.

What causes the fluctuation, especially the mysterious quantum fluctuation associated with the "zero-point motion"? This is a deep and controversial question in fundamental physics. Some physicists insist that the fluctuation is a result of an incompleteness or a drawback of the quantum theory(for example [2]). They believe that a more fundamental theory beyond the quantum theory should be a deterministic one in which predictions of physical quantities should be definite, as Einstein once put it "God does not play dice"[3]. Others, perhaps more and more, believe that this fluctuation is not due to any correctable flaws in measurement, but rather reflects an intrinsic quantum fuzziness in the very nature of energy and matter springing from the wave nature of various quantum fields.

Regardless of the controversies about the origin of fluctuations, the cur-

rent theory turns out to be rather successful. Fluctuation-driven phenomena have attracted a lot of research interests in a variety of areas. One famous example is the Brownian motion[4] – the seemingly random movement of particles suspended in a fluid. This random movement of the suspended particle is driven by thermal fluctuations of the constituent molecules in the fluid and can be explained by the kinetic theory of thermal equilibrium. The importance of the Brownian motion is many-fold: it indirectly confirms the atomic nature of matter that atoms or molecules do exist; it reveals a deep and general relation between thermal fluctuations and dissipation, as the Brownian motion is related to the viscosity of the fluid; practically it can be used for measurement of the pulling force on a single DNA molecule shown recently. Another example is the Casimir force[5], a physical force arising from the quantum fluctuations of electromagnetic fields between two reflecting bodies placed in vacuum. The Casimir force is the physical manifestation of the zero-point energy and can be measured quite accurately between metallic objects separated at a distance of a few micrometers or nanometers. It has been suggested that the Casimir force has applications in micro-technology and nano-technology. Besides, the Casimir force serves as an important conceptual tool for in modern theoretical physics. It is believed that the origin of the dark matter and the cosmology constant is related to the zero-point fluctuations of gravitons. The concept of the Casimir effect can be also applied to emergent degrees of freedom in condensed matter physics, resulting in the “order by disorder” phenomena in quantum magnetism and more exotic phenomena in the strongly coupling regime.

In this thesis, we are interested in the fluctuation-driven phenomena in ultracold atomic gases, in particular the Bose-Einstein condensates (BEC) of ultracold atoms with spin degrees of freedom. BEC is a novel form of matter which has attracted a lot of research interests since the early days of quantum mechanics. Many fascinating quantum phenomena can be observed in a BEC, such as superfluidity and macroscopic coherent dynamics, because the majority of the constituent atoms in a BEC occupy the same microscopic state. Atoms that are not in that particular microscopic state give rise to fluctuations in density correlations, which is related to energy and momentum dissipation, low dimensional phases, and superfluid-insulator phase transitions, among which many have been observed and studied in ultracold atoms.

However, spin fluctuations are less studied and not well understood in Bose-Einstein condensates. These fluctuations can be studied in spinor BEC systems – Bose-Einstein condensates of atoms with spin degrees of freedom.

The coherence and interplay between different spin components within the spinor BEC have promised a wealth of interesting and rich phenomena, such as spin correlated states, macroscopic coherent spin dynamics, spin domains and spin textures, and a variety of topological defects. However, for a long time the accessibility of spinor BEC has been restricted to a small number of physical systems such as superfluid helium-3. The spinor Bose gas of ultracold atoms created in recent experiments provides us new opportunities to study spin correlated matter and especially the spin fluctuations. Spin fluctuations have several interesting and unique effects which can not be studied in the single-component BEC. These effects are the main topics of this thesis, such as fluctuation-driven spin correlations, macroscopic coherent dynamics and fractionalization of topological defects. They are also connected to a number of fluctuation driven phenomena found in other physical systems. The studies of fluctuations in spinor ultracold atoms here can improve our general understanding of fluctuations and may shed light on open problems related to fluctuations.

In the following sections of this chapter, I give a more specific introduction to the topics mentioned above. In Sec.1.1, I go over the fluctuations in a harmonic oscillator, which is an important and useful conceptual tool to illustrate the zero-point motion; then I examine the fluctuations of lattice vibrations based on the picture of harmonic oscillators. In Sec.1.2, I list a number of fluctuation-driven phenomena that people were and are interested in. In Sec.1.3, I go over Bose gas of ultracold atoms with an emphasis on many-body physics. In Sec.1.4, I present a brief survey of the spinor Bose gas. In the last section of this chapter, I provide an outline of the thesis's main contents.

1.1 Fluctuations in a Harmonic Oscillator and Beyond

The harmonic oscillator is one of the simplest models, yet turns out to be one of the most useful models in theoretical physics. With very few exceptions almost any mass or effective mass that subjects to a force in a stable equilibrium acts as a harmonic oscillator in small vibrations. The energy E of a harmonic oscillator is given by

$$E = \frac{p^2}{2m} + \frac{m\omega^2 x^2}{2}. \quad (1.1)$$

Here p is the momentum of the oscillator, x is the position of the oscillator, m is the mass or the effective mass and ω is the angular oscillation frequency.

1.1. Fluctuations in a Harmonic Oscillator and Beyond

According to the classical theory, in the ground state the oscillator sits still at the center with zero momentum and zero energy. The oscillator has a definite position and velocity without any fluctuations.

However, the quantum theory suggests a different picture. According to the Heisenberg's uncertainty principle, the oscillator can not have definite values for both position and momentum at the same time. If one tries to pin the oscillator to the center exactly, its momentum will fluctuate wildly; if one tries to suppress the kinetic energy by keeping $p = 0$, then the position will fluctuate wildly leading to a huge potential energy cost. The state with the lowest energy in the quantum mechanics is called the zero-point motion. The energy associated with the zero-point motion is called zero-point energy which is first proposed by Einstein and Stern in 1913[6]. The zero-point energy of a quantum harmonic oscillator is

$$E = \frac{1}{2}\hbar\omega. \quad (1.2)$$

And the fluctuations in the oscillator's position and momentum are given by

$$\delta x = \sqrt{\frac{\hbar}{2m\omega}} \quad (1.3)$$

$$\delta p = \sqrt{\frac{\hbar m\omega}{2}}. \quad (1.4)$$

The simple picture and even the above equations can be extended to a large number of systems, where the whole system can be viewed as one effective harmonic oscillator or a set of uncoupled effective harmonic oscillators. For example let's look at the zero-point motion of phonons, which are quantized oscillations of the crystal lattices. In the simplest picture, a solid can be described by the displacement U_R of each constituent atom around the lattice site R from their equilibrium positions.

$$r_R = R + U_R. \quad (1.5)$$

The total energy includes the kinetic energy and the elastic potential energy:

$$E = \sum_R \frac{P_R^2}{2m} + \frac{m\omega^2}{2} \sum_{\langle R,R' \rangle} |U_R - U_{R'}|^2. \quad (1.6)$$

Here we assume a quadratic form of the elastic potential which is a reasonable approximation for small vibrations. And without loss of generality we

1.1. Fluctuations in a Harmonic Oscillator and Beyond

also restrict the elastic potential energy to exist only between nearest neighbor sites. In this picture, the solid is not different from a set of coupled harmonic oscillators. One can find out the normal modes of the oscillating system by introducing collective coordinates U_Q and P_Q , in which Q is the crystal momentum of the lattice.

$$U_R = \frac{1}{\sqrt{N_T}} \sum_Q U_Q e^{-iQ \cdot R} \quad (1.7)$$

$$P_R = \frac{1}{\sqrt{N_T}} \sum_Q P_Q e^{iQ \cdot R}. \quad (1.8)$$

Here N_T is the total number of the lattice sites. One can rewrite the energy in the following form

$$E = \sum_Q \left[\frac{P_Q^2}{2m} + \frac{1}{2} m \Omega_Q^2 U_Q^2 \right]. \quad (1.9)$$

Here Ω_Q is a function of ω , Q . In this picture, we have a set of uncoupled harmonic oscillators with different frequencies. The quantized version of each oscillator is called a phonon with momentum Q and energy Ω_Q .

The zero-point of motion of phonons has an important effect: the translational symmetry cannot be spontaneously broken in a one-dimension infinite chain described by Eq.1.6. If the translational symmetry was broken and the crystalline order existed, Ω_Q would vanish linearly when $|Q| \rightarrow 0$. The fluctuation of U_R would become divergence due to the fluctuations at long wavelengths:

$$\langle U_R^2 \rangle = \frac{1}{N_T} \sum_Q \langle |U_Q|^2 \rangle = \frac{1}{N_T} \sum_Q \frac{\hbar}{2m\Omega_Q} \quad (1.10)$$

$$= \frac{1}{2\pi a} \int dQ \frac{\hbar}{2m\Omega_Q} \sim \frac{\hbar}{4\pi a m} \int_0^\Lambda \frac{dQ}{Q}. \quad (1.11)$$

In the second line of the above equation, the summation is replaced by an integral in the continuum limit where $N_T \rightarrow \infty$. Here a is the lattice spacing. The integral includes fluctuations of wave vectors from zero to the Debye cutoff Λ . The infrared divergence of the average displacement indicates that the crystalline order can not exist in this case. In fact, this is an example of the more general Mermin-Wagner theorem, which states that continuous symmetry can not be spontaneously broken in dimension $d \leq 2$ at the zero temperature.

1.2 Fluctuation-Driven Phenomena

Fluctuation is one the most profound and rudimentary concepts in modern physics. The origin of fluctuation is deeply rooted in the fundamental laws of modern physics. It can be found in quantum mechanics, in particular the Heisenberg uncertainty principle; it can also be found in statistical physics that sets the limit of chaotic and thermal motion or usually known as thermal fluctuations. In the strict sense, everything is more or less related to fluctuations according the first principles in quantum mechanics. Still, there are some phenomena which are explicitly related to fluctuations, or even driven by fluctuations. Some of the fluctuation-driven phenomena have played an important role in the development of the quantum theory and statistical mechanics. Some of them still attract interests as they are related to unresolved problems. In the following I will provide a number of well known examples.

- *Lamb shift in atomic physics*

Lamb shift is a small energy difference between the two energy levels $^2S_{1/2}$ and $^2P_{1/2}$ in the hydrogen atom. These two levels are supposed to have the same energy according to the Dirac theory. The experimental discovery of the Lamb shift by Lamb and Retherford in 1947[7] provided a stimulus for the renormalization theory of quantum electrodynamics(QED) in which zero-point fluctuations of electromagnetic fields must be taken into account. In the picture of QED, the physical vacuum is not empty anymore. It is filled with photons, the quantized objects of electromagnetic waves, in the zero-point motion. The Lamb shift can be interpreted as the influence of virtual photons that have been emitted and absorbed by the atom (see, for example, the textbook by Peskin and Schroeder[8]).

- *Casimir effect*

The Casimir force[5] is one of the best known examples of fluctuation-driven phenomena. Consider two uncharged metallic plates in a vacuum separated by a few micrometers. According to the classical theory of fields there should be no forces between two plates since there are simply no sources of electric fields. When zero-point motion or quantum fluctuation of vacuum is taken into account, the above classical picture is changed and there is either attractive or repulsive net forces between two plates, depending on the the geometry and placement of the two plates. This mechanism can be explained again by using virtual photons in quantum electrodynamics. An alternative simple

explanation is that the energy of quantum fluctuations or zero-point motion depends on the specific arrangement of the two plates and thus produces an effective potential for the two plates. The Casimir effect is very general and finds applications in various fields of physics. Accurate measurements were made recently by using nano-scale metallic and semiconductor devices of different geometries[9]. In particular, ultracold atoms turned out to be natural candidates for measuring Casimir-Polder effects at considerably large distances, i.e. a few micrometers. For example, in an experiment by Obrecht *et al.*[10], the frequency of the dipole oscillations is shifted by the Casimir-Polder force between the rubidium atoms and a dielectric substrate separated a micrometers away.

- *Coleman–Weinberg mechanism of spontaneous symmetry breaking*
In 1972, Coleman and Weinberg[11] considered the electrodynamics of massless mesons. They pointed out that quantum fluctuations of electromagnetic fields, or more specifically radiative corrections in this case, may produce spontaneous symmetry breaking and may lead to a mass generation of mesons. In the terminology of quantum field theory, it is a form of spontaneous symmetry breaking which does not show up at the tree level. Equivalently one may say that the Coleman-Weinberg model possesses a first-order phase transition. The Coleman-Weinberg mechanism is very general and finds applications in high energy physics as well as condensed matter physics.
- *Order by disorder in quantum magnetism*
Fluctuation effects in frustrated magnetism have attracted a lot of interest in recent years. The frustration, either of geometrical origin or as a result of competition between different couplings, usually lead to a family of degenerate classical ground states. Fluctuations will lift the accidental degeneracy and select out a particular type of classical ground states, usually with higher symmetries. In the condensed matter community, this mechanism is commonly known as “order by disorder” [12, 13, 14]. For example, let’s consider spins in an anti-ferromagnetic body-cubic-centered lattice with strong next-nearest neighbor couplings and weaker nearest neighbor couplings. In this case, one has two simple cubic anti-ferromagnetic sublattices. In the classical version or the mean field approximation the system’s energy is independent of relative orientations of the two sublattices. In the quantum version, one must consider the fluctuations (spin waves

in this case) around different classical ground states. It is shown that quantum fluctuations favour a collinear alignment of the sublattices. Examples of ground state selection via quantum fluctuation have been demonstrated in a number of frustrated magnetic systems such as frustrated Heisenberg model, body-centered tetragonal model, and Kagomé lattices (see [15] for a review).

- *The Mermin–Wagner–Hohenberg theorem and fluctuations in low dimensional systems*

The Mermin–Wagner–Hohenberg theorem [16, 17] (also known as Mermin–Wagner theorem) states that continuous symmetries cannot be spontaneously broken at finite temperature in systems with sufficiently short-range interactions in dimensions $d \leq 2$. Strong fluctuations in low dimensional systems will destroy those ordered states that could exist in the higher dimensional counterparts. For example, gapless fluctuations of scalar fields lead to a logarithmic divergent correlation function. Excitations of gapless long-range fluctuations are always favored because they can increase the entropy at very low energy cost. The entropy of a gapless mode with momentum k scales as $k^{d-1} \log k$ and it always dominates the energy cost (scaling as $|k|$) for any finite temperatures in $d \leq 2$ systems. This theorem points out the importance of fluctuations in low dimensional systems and finds applications in many systems. In the context of spinor ultracold atoms, there is no true long-range two-dimension condensate at finite temperatures; and the fluctuations can destroy the long-range coherence of spin correlations in 2d, leading to short-range spin correlations.

- *The Fluctuation-dissipation theorem*

The fluctuation-dissipation theorem is a simple, yet quite deep, concept originated from statistical physics. It reveals a remarkably simple relation between the dynamical system’s response to small external perturbations and its inherent thermal noise. The underlying principle of the fluctuation-dissipation theorem is that a non-equilibrium state may have been reached either as a result of a random fluctuation or of an external force, and that the evolution toward equilibrium is the same in both cases. One example is the Brownian motion of tiny particles suspended in fluids. It was realized that random forces or fluctuations that resulted in thermal motions of molecules or atoms composing the fluid are responsible for both driving the particle into the Brownian motion and also dragging the particle if pushed through

the fluid. Einstein pointed out the underlying link with his famous Einstein-relation[18] that the diffusion constant D is related to temperature T and particle's mobility μ_p as $D = \mu_p k_B T$. The fluctuation-dissipation theorem enables transport coefficients to be calculated in terms of response to external fields.

1.3 Bose-Einstein Condensates of Ultracold Atoms

The successful experimental realization of the long-predicted Bose-Einstein condensates (BEC) in dilute alkali atomic gases[19, 20, 21] in 1995 has opened up a new era in which many-body physics has become one of the primary concerns in ultracold atomic gases. Breakthrough technologies in cooling, trapping and manipulating methods have enabled us to explore quantum many-body phenomena in which statistics, interactions, correlations and collective behaviors of a large number of atoms rather than properties of single atoms or photons are of main interest. Remarkable progress has been made in the past decade in this fast-evolving field as a large number of ultracold atomic systems have been created and a wide range of many-body phenomena have been realized and studied in experiments.

Attaining a sufficiently cold temperature is a crucial prerequisite and a great technical challenge for the study of quantum many-body effects in dilute atomic gases. This is because the quantum degeneracy temperature, the threshold below which quantum statistics become important, is extremely low in dilute atomic gases as compared to other condensed matter systems. The degeneracy temperature of atomic gases of typical densities $\sim 10^{13}\text{cm}^3$ is of order 100nK, which is seven orders of magnitude smaller than that of the superfluid helium, and ten orders of magnitude smaller than the electronic Fermi energy in metals. Such a low temperature scale is needed to realize BEC, superfluidity, degenerate Fermi gas. For more subtle many-body phenomena such as superconductivity or quantum magnetism, the relevant temperature scale crucially depends on the interaction strength and may be even far below the quantum degeneracy temperature. Efforts of cooling atomic gases in pursuit of atomic BEC began in the late 1970s, when people first realized that lasers could be used to trap and cool atoms[22]. However, the lowest temperature in laser cooling is set by the recoil energy (about $1\mu\text{K}$), which is the kinetic energy an atom acquires through the spontaneous emission of a single photon. It turns out that to go beyond the laser cooling limits and reach the ultracold regime, one needs new technologies

such as evaporative cooling with magnetic or magneto-optical trappings. These breakthrough technologies have finally amounted to the realization of BEC in alkali atomic gases, with a temperature of 50nK that is one third of the condensate transition temperature[19]. Up to now, a large number of atomic systems have been cooled to close to or even below the degeneracy temperatures. Atomic BEC was created in a number of isotopes of alkali elements as well as other elements of ^1H [23], ^4He [24] in the lowest triplet state, ^7Li [20], ^{23}Na [21], ^{41}K [25], ^{52}Cr [26], ^{84}Sr [27], ^{85}Rb [28, 29], ^{87}Rb [19], and ^{133}Cs [30]. Degenerate fermionic gas as well as Bose-Fermi mixtures were created in ^{40}K [31], ^{40}K - ^{87}Rb [32], ^6Li - ^7Li [33, 34], ^6Li - ^{23}Na [35]. In particular, all-optical trapping allows us to create quantum degenerate gas with internal degrees of freedom arising from hyperfine spins: hyperfine spin $F = 1$ [36] and $F = 2$ [37] ^{23}Na , $F = 1$ [38] and $F = 2$ [39] ^{23}Rb , $F = 3$ ^{52}Cr [26], and a pseudo-spin one-half (two hyperfine levels are involved) systems such as $|F = 1, m = 2\rangle$ and $|F = 1, m = -1\rangle$ in ^{87}Rb BEC[40], and $|F = \frac{1}{2}, m = \pm\frac{1}{2}\rangle$ in ^6Li Fermi gas[41]. Cold molecules were also created in experiments using Feshbach resonance (see review articles [42] and [43]).

Besides being ultracold, a number of other features have made dilute atomic gases a perfect playground for studying many-body quantum physics. From theorists' point of view, the dilute atomic gas is "pure" and "clean" in a sense that the interatomic interactions, at least the relevant low-energy properties, are clearly understood and accurately modeled. Besides, dilute gases in experiments are well isolated from environment; thus they are free from uncontrolled disorder, defects or noise that are ubiquitous in traditional materials studied in condensed matter physics. Furthermore, highly developed and sophisticated technologies of atomic, molecular and optical physics have enabled us to prepare, manipulate and measure ultracold atomic gases with unprecedented control and precision. A large number of controlling parameters, including those that are hard to change in traditional experiments, can be easily and independently tuned. Examples include geometries of trapping potentials, dimensionality of quantum gases, interaction strength between atoms, tunneling rates between arrays of localized atoms, population and relative phase of atoms in different species, total momentum as in moving condensates, angular momentum as in rotating gas and disorders.

Early experimental studies were focused on quantum Bose gases and were aimed at investigating the important consequences of Bose-Einstein condensation. Major achievements of these studies have been, among others, the hydrodynamic nature of the collective oscillations [44, 45, 46], Josephson-like effects [47, 48], the realization of quantized vortices [49, 50, 51], the observation of interference of matter waves [52], the study of coherence phe-

nomena in atom laser configurations [53, 54, 55, 56], the observation of four-wave mixing [57] the realization of spinor condensates [38] and coherent spin dynamics[58, 39]; the propagation of solitons [59, 60, 61, 62].

On the theoretical side, these phenomena can be well understood in the framework of mean field theory in which one assumes the existence of a macroscopic wavefunction $\Psi(r)$ (also known as order parameter) and a nonlinear Schrodinger-like equation that governs the macroscopic wavefunction. This mean field theory is an analogue of the Ginzburg-Landau theory of superconductors(see the book by Tinkham [63] for a reference), in which the macroscopic wavefunction describes the bosonic fluid made up of Cooper pairs of electrons. Here the macroscopic wavefunction $\Psi(r)$ is directly related to the superfluid of bosonic atoms. The superfluid density ρ_s and the super-current's velocity \mathbf{v}_s are related to $\Psi(r) = |\Psi(r)|e^{i\Theta(r)}$ as

$$\rho_s = |\Psi(r)|^2 \quad (1.12)$$

$$\mathbf{v}_s = \frac{\hbar}{m} \nabla \Theta \quad (1.13)$$

In weakly-interacting Bose gases at zero temperature, the order parameter coincides with one of the eigen-states of the one-body density matrix. The eigenvalue associated with this eigen-state is exactly the fraction of the total atoms in the Bose-Einstein condensate. Spatial structures and temporal evolutions of the macroscopic wavefunction are governed by the Gross-Pitaevskii equation[64, 65]:

$$i \frac{\partial \Psi}{\partial t} = -\frac{\hbar^2}{2m} \nabla^2 \Psi + g|\Psi|^2 \Psi + V(r)\Psi \quad (1.14)$$

This nonlinear Schrodinger-like equation includes the effects of interaction in its nonlinear term, as well as the consequences of trapping potentials $V(r)$. The mean field theory has provided a complete description of low energy degrees of freedom in weakly-interacting Bose gases. It has proven capable of accounting for most of the relevant experimentally measured quantities in Bose-Einstein condensed gases such as density profiles, collective oscillations, structure of vortices, etc. (see review papers and books[66, 67, 68, 69]).

The realization of superfluid-insulator phase transition in Bose gas confined in optical lattices[70, 71] opens up opportunities to go beyond the mean field picture and to reach the strongly coupling limit in quantum gases. Experimental developments such as Feshbach resonance and optical lattices have substantially extended the range of many-body physics that can be explored in ultracold gases.

Optical lattices are made up of several pairs of counter-propagating laser beams. The standing wave pattern provides an periodic potential which mimics the crystalline lattice in solids. In deep optical lattices, the local wells (local minimum in the periodical potential) have an effective confining frequency of order 10kHz which is 10 – 100 times larger than the typical frequency in atomic traps. The strong confinement not only enhances the interaction energy via increasing the overlap of two atoms occupying the same well, but also reduces the effective hopping of atoms between different wells. These two effects can both increase the fluctuations in Bose-Einstein condensates, leading a quantum phase transition. In a seminal paper Jaksch *et al.* [70] proposed to realize a quantum phase transition from superfluid phase to Mott-insulator phase by loading cold bosonic atoms in optical lattices and increasing the optical potential depth. The experimental observation of superfluid-insulator transition first reported by Bloch's group [71] marked the beginning of exploring strongly correlated quantum gases in optical lattices. Several other groups have observed superfluid-insulator transitions in clean bosonic systems, disordered bosonic systems, boson-fermion mixtures.

In particular, optical lattices can be used to create low dimensional atomic gases. For example, a two-dimension configuration (in the xy plane) can be obtained by applying a strong confinement in the z direction. In this configuration the spatial degree freedom in the z direction is actually “frozen” in the low temperature regime, while atoms can still move around in the other two directions. Using similar methods one can create one-dimension gas. The one-dimension hardcore Bose gas was created and observed in ultracold atoms loaded in one-dimension tubes made by optical lattices by Paredes *et al.*[72] and Kinoshita*et al.*[73]. These experiments are the first experimental realization of Tonks-Girardeau gas after its prediction [72, 73] 40 years ago. The Berezinskii-Kosterlitz-Thouless phase transition [74, 75]in two dimensional superfluid was also observed in experiments, in particular the vortex-anti vortex confinement-proliferation transition are examined [75].

Another, or perhaps more direct way to reach the strongly interacting regime is tuning two-body scattering properties via Feshbach resonance. Feshbach resonances refer to an energy-dependent enhancement of interparticle collision cross sections due to the existence of a metastable bound state. Such phenomena have been thoroughly studied in nuclear physics[76, 77, 78]. In ultracold atomic gases, the associated resonance energy depend on the strength of magnetic fields via Zeeman energy of different hyperfine levels. Near these magnetic field tuned resonances, the values of two-body scattering lengths become comparable to or even larger than average interatomic

distances, leading to strongly-correlated atomic gases. In Bose gases, Feshbach resonance was first observed in Bose-Einstein condensates in 1997 by Cornish *et al.*[79]. On one side of resonance where scattering lengths are negative, collapse growth cycles due to thermal clouds and collapsing-exploding dynamics due to mechanical instabilities have been observed by Bradley *et al.*[20], Donley *et al.*[80] and Roberts *et al.*[81]. Despite the reduced lifetime of Bose gases near Feshbach resonance due to enhanced three body recombination, quite remarkable progress[82, 83] has been made recently to explore the physics of Bose gases at large scattering lengths where quantum fluctuations can no longer be accounted for by perturbations around mean field theories. On the few-body level, evidence of fascinating three-body Efimov states and universal four-body states near resonance are observed in recent compelling experiments[84, 85, 86].

In these strongly-coupling quantum systems, mean field theories don't suffice, sometimes even break down, due to the strong fluctuations arising from strong optical confinement, resonant interactions and other methods.

1.4 Ultracold Spinor Condensates

In early experiments, Bose-Einstein condensates were usually confined in magnetic traps. The confining potential in magnetic traps is produced by Zeeman energy of hyperfine spins. One limitation of magnetic trapping is that only “low field seekers” - atoms with particular spins that favor low magnetic field - can be trapped. During inelastic scattering processes, “low field seekers” can flip into “high field seekers” resulting in a decrease in the number of atoms confined in the trap (trap loss). When atoms with different hyperfine spins are simultaneously confined, trap loss may dramatically increase through spin relaxation collisions, restricting experimental studies of spinor condensates. Alternatively, one can say that the spin degrees of freedom are “frozen” in magnetic traps.

This limitation is overcome by using optical trapping methods in which the spin independent confining potential is produced by couplings between laser lights and atoms' electrical dipoles. The spinor Bose-Einstein condensates were first created in hyperfine $F = 1$ ^{23}Na atoms [38, 36] in optical traps. In these experiments, spinor condensates of $F = 1$ ^{23}Na atoms were prepared in several steps. Laser cooling and evaporative cooling was used to produce sodium condensates in the $m_F = -1$ state in a cloverleaf magnetic trap. The condensates were then transferred into an optical dipole trap consisting of a single focused infrared laser beam. In the final step of prepa-

ration, desired hyperfine levels were then populated by transferring atoms in $m_F = -1$ via Rabi oscillations. Linear superposition of hyperfine levels such as $\frac{1}{\sqrt{2}}(|m_F = 1\rangle + |m_F = -1\rangle)$ was prepared by tuning frequencies and durations of the driving fields in Rabi oscillations. The evolution and lifetime of the spinor condensate were measured by the standard time-of-flight method, in which hyper levels were separated by applying a Stern-Gerlach magnetic gradient field. It turns out the spinor condensate in this case had a relatively long lifetime of 1 – 10 seconds, which made itself a perfect experimental candidate for studying rich physics predicted in spinor condensates. Spinor condensates were later created in other systems, including hyperfine $F = 2$ ^{23}Na [37], hyperfine $F = 1$ and $F = 2$ ^{87}Rb [58, 87, 39, 88]. Although bosons with half integer spins are prohibited by quantum statistics, spinor condensates with pseudo-spin 1/2 were created in binary mixtures of $F = 1$ and $F = 2$ Rb atoms with the help of Rabi oscillations driven by external microwave fields [40, 89, 90].

The successful creation of stable spinor condensates have led to fruitful experimental studies covering different topics: magnetic orderings and associated quantum phase transitions [91, 92, 93, 94], coherent spin dynamics [49, 95, 39, 88, 58, 87, 96, 97, 98, 99, 100, 101, 102, 103], exotic topological defects [104].

The central theme of these phenomena in the spinor condensates is the interplay between coherence and spin dependent interaction. Coherence is the hallmark of Bose-Einstein condensates in which most of the particles share the same wavefunction. In spinor condensates, coherence is further extended to internal degrees of freedom such that atoms in different hyperfine levels have stationary phase differences. Coherence of internal degrees of freedom is also the distinction between spinor condensates and fragmented condensates[105, 106]. For example, let's consider a nematic spin condensate of N atoms: $|\Psi_s\rangle \sim (\psi_{+1}^\dagger + \psi_{-1}^\dagger)^N |0\rangle$ and a fragmented condensate as $|\Psi_f\rangle \sim (\psi_{+1}^\dagger)^{\frac{N}{2}} (\psi_{-1}^\dagger)^{\frac{N}{2}} |0\rangle$. Although these two states have the same average atom number in each hyperfine level, their physical properties are very different. Ψ_s depends on the relative phase between two components such that by shifting ψ_{+1} to $e^{i\theta}\psi_{+1}$ one would have another condensate which is related to the original one by a rotation; for fragmented condensates, such a phase shift merely leads to a global gauge phase shift, leaving the state unchanged.

Interatomic interactions between atoms with internal degrees of freedom are more complicated, leading to a variety of structures and dynamics in spinor condensates. The structure and symmetry of the magnetic ordered

ground states depend on details of interatomic interactions. Rich phase diagrams of a variety of magnetic ordered states are mapped out for hyperfine spin $F = 1$, $F = 2$ [107, 108], and arbitrary F spinor condensates[109] in principle. When magnetic fields are present, a competition between Zeeman energy and inter-atomic interaction will lead to more complicated and rich phase diagrams and quantum phase transitions which are experimentally accessible by tuning external magnetic fields [38, 99, 93, 100, 94].

On the two-body level, spin-dependent interaction is responsible for spin-changing scattering processes. Two atoms can change their hyperfine spins during elastic scattering processes. For example, two $|m_F = 0\rangle$ atoms can become $|m_F = +1\rangle$ and $|m_F = -1\rangle$ and vice versa. Rabi-like oscillations of spins due to the elastic spin-changing scattering are observed and studied in the few-body limit[96, 97]. These oscillations are driven by the interatomic interactions rather than external driving forces. The inter-convertibility of different internal degrees of freedom is the distinction between spinor systems and interspecies mixtures(although spinor condensates can be treated as a binary mixture in some cases).

In spinor condensates, coherent spin-changing scattering can drive coherent spin dynamics, which is a class of macroscopic quantum phenomena similar to Josephson oscillations between coupled superconductors[110]. When the spinor condensate are prepared in a state other than its ground state, the condensate will change its spin as a whole, resulting in a time-reversible macroscopic spin dynamics that could be observed in experiments. Coherent spin dynamics are the focus of a number of experimental studies in spinor condensates of ^{23}Na atoms with hyperfine spin $F = 1$ [100, 58] and $F = 2$ [58], and of ^{87}Rb atoms with hyperfine spin $F = 1$ [87, 98] and $F = 2$ [39, 99, 95, 102].

Spin coherent dynamics is studied in many theoretical investigations[111, 112, 113, 114, 94, 115, 116, 117, 118, 119, 120, 121, 122]. Simply speaking, coherent spin dynamics can be roughly described by a classical pendulum living in the internal spin space[58]. In this analogy, the spatial position of the pendulum represents the spin population and relative phases between different spin levels. The oscillation of the pendulum is driven by an external force, and spin dynamics is driven by interaction energy differences of spinor condensates. The initial potential energy can convert into the kinetic energy of a pendulum, corresponding to the kinetic spin energy with an effective mass determined by interactions. In Chap.4, I will present the equation of motion of spin coherent dynamics which makes this analogy more transparent. Note that although the condensate and the formation of the order parameter depends on quantum mechanics, the dynamics of the

order parameter is classical in many spinor condensates. As shown later in some cases, such a classical treatment of order parameter is not sufficient as fluctuations set in.

The interplay of coherence and spin-dependent interaction can also lead to exotic topological defects such as fractionalized quantum vortices in spinor condensates. In conventional quantum superfluids, the circulation of super-current along any closed loop must be integer times of a basic quanta, i.e. $\oint \mathbf{v}_s \cdot d\mathbf{l} = C \frac{2\pi\hbar}{m}$, $C = 0, \pm 1, \pm 2, \dots$ (m is the mass of the atom). This quantization rule is related to the phase coherence throughout the condensate or single-valuedness of the wavefunction, requiring that the phase winding along any closed loop must be multiples of 2π . Fractionalized quantum vortices with circulation quanta $|C| < 1$ are energetically forbidden, as the energy cost for a phase discontinuity is proportional to the size of the whole condensate. In spinor condensates, fractionalized quantum vortices can be stabilized by additional structures brought in by spin degrees of freedom. For example, a half quantum vortex[123] composed of a π spin dislocation and $C = 1/2$ phase winding is an energetically stable topological defect in $F = 1$ nematic spinor condensates. The phase discontinuity of π brought by phase winding $C = 1/2$ is annihilated by superimposing a spin rotation which generates a Berry phase π . $C = 1/2$ quantum vortices are also predicted in biaxial nematic $F = 2$ spinor condensates[124], and $C = 1/3$ quantum vortices are predicted in cyclic phase in $F = 2$ spinor condensates[125]. High dimensional topological defects such as skyrmions and monopoles are possible stable topological defects in spinor condensates. A systematic way to classify topological defects is to analyze the topology and symmetry of the ground states' manifold (the geometrical space in which the order parameter lives)[126]. For example, the ground state manifold of single-component BEC is $U(1)$ or S_1 or a unit circle, representing the phase. The ground state manifold of nematic condensate is more complicated: $\frac{(S_1 \times S_2)}{Z_2}$, where S_1 is a unit circle for the phase, S_2 is a unit sphere for the spin nematic vector, the gauge group Z_2 is for the gauge symmetry [123] in the $S_1 \times S_2$ representation and is closely related to the half quantum vortices. Similarly, a discrete gauge symmetry group of the $C = 1/3$ quantum vortex was predicted in cyclic phase[125].

From the theoretical point of view, the coherence with spin degrees of freedom can be well understood in the mean field theory. Ground state properties, low-energy excitations as well as spin dynamics can be described by the Gross-Pitaevskii equation (see Sec.1.3 in this chapter) in which a multi-component order parameter is introduced to account for internal degrees of

freedom. The validity of mean field theory relies on the assumption that fluctuations around mean field solutions are small and have little effects on physical properties. This is indeed the case in many experiments of dilute spinor Bose gas, in which fluctuations only provide a small correction to the mean field result.

However, there are certain cases when fluctuations are important and the mean field picture will not suffice.

1. *Broken symmetry restoring*

In early theoretical investigations of spinor condensates, it was noticed that the ground state predicted by the quantum rotor model method [118] is different from the mean field ground states.

In $F = 1$ spinor gas with anti-ferromagnetic interactions, the mean field ground state [107, 108] is a nematic state. They are rotational symmetry broken states and are hugely degenerate. The broken symmetry is specified by a nematic vector \mathbf{n} such that all the atoms are in the hyperfine $m_F = 0$ levels if \mathbf{n} is the projection axis.

On the other hand, the quantum rotor model [113] predicted a spin-singlet ground state which is rotationally invariant and non-degenerate. The state vector in the Zeeman basis is given by $\left(\frac{1}{2}, \frac{1}{\sqrt{2}}, \frac{1}{2}\right)$. Furthermore, the quantum rotor model predicts spin dynamics that would mix nematic states with different \mathbf{n} . This dynamics is absent in the mean field theory.

It turns out that results obtained by the quantum rotor model can be reproduced by including quantum fluctuations in the mean field nematic states. The broken rotational symmetry is restored by quantum fluctuations at wavelengths of the condensate size through the nematic-mixing dynamics. In fact, the spin singlet state can be viewed as a state with fluctuating nematic vectors:

$$\Psi_s = \int d\mathbf{n} |\mathbf{n}\rangle. \quad (1.15)$$

More importantly, the effects of fluctuations at wavelengths of the condensate size will eventually vanish in the thermodynamic limit $N \rightarrow \infty$, thus making mean field description exact. For example (pointed out in [123]), the nematic-mixing dynamics takes place at a time scale proportional to N , and the energy difference between spin singlet state and nematic state is proportional to $\frac{1}{N}$ of the total energy.

The degeneracy in ground states predicted in the mean field theory is also exact in the thermodynamic limit, in a sense that there are numerous low-lying states with excitation energies of $\sim \frac{1}{N}$ in a condensate of N atoms. In the thermodynamic limit, mean field theory provides an accurate and convenient theoretical description for ground states and low energy degrees of freedom. On the other hand the quantum rotor model is a more natural choice to describe few-body systems, as the quantum fluctuations in nematic states are strong in these systems. The size-dependent nematic-mixing dynamics is a good example to reveal the difference and connection between few-body physics and many-body physics. It also clearly demonstrates that spontaneous symmetry breaking is a many-body effect that only happens in the thermodynamic limit.

On the theoretical side, full numerical simulations [113, 118, 116, 120, 114] showed that fluctuations lead to slow dynamics in mean field ground states as well as damping or de-phasing in mean field spin dynamics. These results are also obtained in [119, 115] by introducing an effective quantum Hamiltonian in which the spin population and condensate phase forms a canonical conjugate pair. Peculiar behaviors in long-time spin dynamics due to fluctuations are studied by Diener *et al.* [117] who pointed out the “quantum carpet” spin-time structure with self-similar properties in spin dynamics.

On the experimental side, the observation of fluctuation-driven dynamics is a challenging task, because these dynamics such as damped oscillations take place at timescales > 10 s under usual conditions, which is beyond the lifetime of the condensate. Besides, damped oscillations observed in experiments may be attributed to other factors such as the breakdown of single mode approximation [119, 115], and dissipative dynamics[94]. It is suggested to make observations in relatively small condensates loaded in high-finesse optical cavities, which can detect spin changes with precision[127]. In a recent experiment on spin coherent dynamics in $F = 1$ sodium condensate, Liu *et al.*[94] directly measured the atom number fluctuation or “shot-noise” in spin projections, and revealed the dissipative nature of the spin dynamics.

2. Spinor gas in optical lattices

Quantum fluctuations in single-component Bose-Einstein condensates can be greatly enhanced in optical lattices, leading to a superfluid-insulator quantum phase transition [71] in which the phase coherence

is completely destroyed by quantum fluctuations. For a spinor gas in the optical lattice, similar quantum phase transitions would take place when the optical potential is increased, except here interactions between spin degrees freedom give rise to richer and more subtle phase diagrams and transitions. On the Mott insulator side, additional possible quantum phase transitions between spin-ordered Mott insulating and spin-disordered Mott insulating states are predicted and studied in $F = 1$ cold atoms [128, 129, 130, 131, 132, 133], and $F = 2$ atoms[134, 135]. On the superfluid side, coherent spin dynamics predicted in the mean field theory is greatly modified by enhanced quantum fluctuations, especially approaching the phase transition[136]. In Chap. 4, I am going to examine in detail another type of coherent spin dynamics driven solely by fluctuations in the optical lattice.

Optical lattices can also be used to study low dimensional ultracold gases where fluctuations are strong and differ from the high dimensional cases qualitatively. For example, Mott insulating phases and exotic spin correlations are studied in $F = 1$ antiferromagnetic spinor gas confined in low dimensional geometries[128, 129, 131, 130]. In Chap.5 and [137], half quantum vortices in two-dimension topologically ordered superfluids are examined in details. On the experimental side, disk and wave-guide confinement can be realized via optical lattices. Strongly repulsive one-dimension Bose gas (Tonks-Girardeau gas)[72, 73] and BKT[74, 75] phase transition in two-dimension Bose gas have been observed and are the focus of many recent experimental studies.

3. Order by disorder phenomena

In $F = 2$ nematic spinor condensates, the accidental degeneracy of a family of nematic states predicted in the mean field theory is lifted by quantum fluctuations and thermal fluctuations, giving rise to nematic states with higher symmetries such as the uniaxial nematic state which is rotationally invariant along its easy-axis or the bi-axial nematic state with dihedral-4 symmetry. This mechanism is an analogue of “order by disorder” in quantum magnetism or the Lamb shift in electronic spectrum of hydrogen atoms where fluctuations around the mean field “vacuum” lead to observable effects. Fluctuation can also drive a coherent spin dynamics which is otherwise absent in the mean field theory. This novel type of dynamics can be controlled in optical lattice and is highly sensitive to fluctuations. I will examine this topic in detail

in Chap.3.

1.5 Organization of the Thesis

The rest of the thesis is organized as follows. In Chap.2, I briefly discuss some of the atomic properties of alkaline atoms with an emphasis on spin-dependent low-energy scattering. In particular, vector or tensor basis are introduced. The following chapters are divided into two parts, for two kinds of fluctuation-driven phenomena in spinor systems. The first part consists of Chap. 3 and Chap.4, which focus on $F = 2$ nematic spinor condensates. In Chap.3, I present one of the major results in this thesis — fluctuation-driven spin nematic states in spinor condensates. After examining the mean field phase diagram of spin correlated phases in the first section, the collective excitations of spin nematic states are examined in detail. Effective potential of different nematic states at zero temperature is obtained, leading to the main conclusion of this chapter. In the following chapter, I study the coherent spin dynamics driven and controlled by fluctuations in the same system. An effective Hamiltonian including the leading order of fluctuations is obtained for spin dynamics in the first several sections of this chapter. Using this Hamiltonian, coherent spin dynamics under various experimental conditions are examined in details in the following section. Effects of finite temperatures and spin loss are also discussed at the end of the chapter. In Chap.5, I turn to the second part of the thesis — fractionalized quantum vortices in $F = 1$ nematic spinor superfluid. In the first several sections of this chapter I present the spatial and magnetic structures of half quantum vortices and dynamical creation of vortex lattice in spinor condensates where the order parameter is well defined. In the following sections, I turn to the half quantum vortex in the strongly fluctuating limit — $2D$ spinor superfluids. A heuristic argument using gauge field formulation is carried out to illustrate the basic ideas which are later confirmed in Monte Carlo simulations. Nucleation of half quantum vortices in rotating traps is discussed later as one of the experimental signatures of the topological order. In the conclusion, I summarize the main results and list some related topics in the future. In the appendix, I include some calculations that are not presented in the main text for reference.

Chapter 2

Interatomic Interactions and Low-Energy Scattering

Atomic properties of alkaline atoms play an key role in both theory and experiment of atomic gases. In this chapter I will briefly discuss some of the atomic properties of alkaline atoms with an emphasis on spin-dependent low-energy scattering processes. In Sec.2.1, I describe the interatomic interactions between alkaline atoms. In Sec.2.2, I go over the low-energy scattering theory in which the s-wave scattering length is introduced. In Sec.2.3, I describe the effects of hyperfine spin degrees of freedom on scattering. Atoms may change their hyperfine spins during the elastic scattering processes due to the exchange effects of electronic spins. The elastic spin-changing scattering is exactly the microscopic origin of spin fluctuations coherent spin dynamics in spinor condensates. In the low-energy scattering theory, spin-changing collisions can be modeled by introducing spin-dependent scattering lengths. In Sec.2.3, I describe the vector and the tensor representations of the spins. Compared to the standard Zeeman basis, the vector and tensor representations are more convenient for theoretical analysis when rotational symmetries are concerned. In the last section of this chapter I describe the quadratic Zeeman shift, which is the leading order nontrivial effect of magnetic fields on spinor gases.

2.1 Interatomic Interactions

Fig.2.1 is the interatomic interaction energy of two ^{85}Rb atoms, which is a typical example of interatomic potential of alkali atoms. The long-range part of interatomic interaction between two alkali atoms is of van der Waals type ($\simeq -C_6r^{-6}$), due to an induced dipole-dipole attractive interaction between two unpolarized atoms. At short distances, a strong repulsion arises due to the large overlapping of the electrons' wavefunction. The crossover between the repulsion at small distances and attraction at long distances is marked by an equilibrium position r_{min} , with a typical value of $1 - 10a_B$ in alkali

2.1. Interatomic Interactions

atoms.

The long-range van der Waals interaction defines another length scale l_{vdW} , at which the strength of interaction energy $\frac{C_6}{r^6}$ is equal to the kinetic energy $\frac{\hbar^2}{2mr^2}$. The van der Waals characteristic length scale l_{vdW} is of order $\sim 100a_B$ in alkali atoms, which roughly sets the scale for scattering lengths.

The interatomic interaction depends on the spin states of the electrons. For two alkali atoms, two electrons outside the closed shells can form either a spin singlet $S = 0$ or a spin triplet $S = 1$. The spin triplet state usually has a higher energy as a result of its anti-symmetric spatial wavefunction. Therefore, two electrons in the triplet state are not likely to reduce their total energy by occupying the same orbital as in the singlet case.

For atoms with definite hyperfine spins, the electronic spin state is a linear combination of spin singlet and spin triplet, leading to a hyperfine spin dependent interaction. For example in Fig.2.1, when two atoms are far apart, there is an energy difference between atoms with different F . Such a spin dependent interaction is the source of spin-dependent low-energy collisions and spin-changing scattering processes that are going to be examined later.

Besides spin-exchange interactions, another type of spin-dependent interaction in ultracold gases is magnetic dipole-dipole interaction. The nuclear dipole moment is three orders of magnitude smaller than electronic dipole moment and is neglected. The dipole-dipole interaction between two atoms is

$$U_d = \frac{1}{2} \frac{4\pi\hbar^2 a_d}{m} \int dr_1 dr_2 \frac{\mathbf{S}_1 \cdot \mathbf{S}_2 - 3(\mathbf{S}_1 \cdot \hat{\mathbf{r}}_{12})(\mathbf{S}_2 \cdot \hat{\mathbf{r}}_{12})}{r_{12}^3}, \quad (2.1)$$

where the dipole length a_d is introduced to represent the strength of dipole-dipole interaction [138] as

$$a_d = \frac{\mu_0 g_F^2 \mu_B^2 m}{12\pi\hbar^2}. \quad (2.2)$$

The scattering length which characterizes the strength of the interaction for Rb⁸⁷ is around 5nm, which is about two orders of magnitude larger than the dipole length $a_d = 0.01\text{nm}$ [139]. In ⁸⁷Rb, the effective scattering length for the hyperfine spin dependent exchange interaction is about -0.03nm for $F = 1$ and 0.08nm for $F = 2$ [97], which marginally dominates the dipole-dipole interaction in the latter case. For spinor condensates with ferromagnetic correlations, the dipole-dipole interaction can lead to observable effects such as spin textures as recently reported by [139].

For spinor condensates with antiferromagnetic interactions as considered in this thesis, the effects due to the dipole-dipole interaction are suppressed

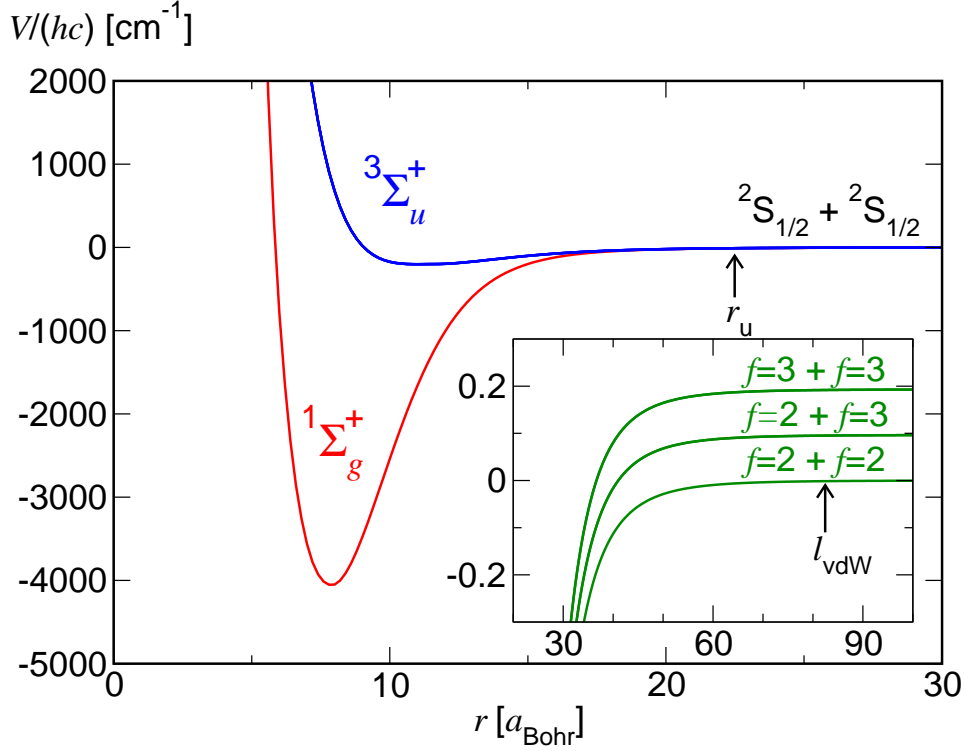


Figure 2.1: (Color online) Interaction energy of two ^{85}Rb atoms as a function of internuclear distance r [42]. The interaction energy in the electronic spin singlet state $1\Sigma_g^+$ (in red) and triplet state $3\Sigma_u^+$ (in blue). The inset shows the hyperfine structures at large distances. The hyperfine splitting between $F = 2$ and $F = 3$ is 3GHz for the ^{85}Rb isotope. The ^{87}Rb isotope has a similar curve, but the hyperfine spin structure is different. The values of hyperfine spin are $F = 1$ and $F = 2$, with a splitting 6.8 GHz. An energy associated with wave number unit 1cm^{-1} corresponds to 30 GHz or 1.44K.

because the local spin moment S_α vanishes in nematic spinor BECs. To induce a nonzero local spin moments, one need considerably large magnetic fields. For the cases considered in Chap.4 one needs around 400mG to match the energy difference between the ferromagnetic states and nematic spin states in optical lattices. Hence, for nematic spinor condensates under small magnetic fields, one can neglect the dipole-dipole interactions.

2.2 Low Energy Scattering

In this section, we briefly review the scattering theory, which provides a theoretical framework to describing low energy collisions. Spin dependent interaction lead to spin-changing processes that can be described in multi-channel scattering theory.

Let's first consider two spinless bosons scattering in 3D space through a short-range isotropic interaction $V(|r|)$. Potentials falling faster than r^{-3} at long distance can also be treated as short-range potential[1]. Thus van der Waals potential decaying at r^{-6} can be treated as short-range potential with an effective range $\sim l_{vdW}$.

The asymptotic behavior of the total wavefunction in the center of motion frame is given by

$$\psi(r) = e^{ikz} + f(\theta) \frac{e^{ikr}}{r}. \quad (2.3)$$

Here the relative velocity in the incoming wave is along z direction. $f(\theta)$ is the scattering amplitude as a function of the angle between the incoming wave and the scattering wave.

For isotropic potentials, scattering waves can be decomposed into uncoupled partial waves according to their angular momentum.

$$f(\theta) = \sum_{l=0}^{\infty} f_l P_l(\cos(\theta)). \quad (2.4)$$

It turns out that for low energy scattering in Bose gas, s-wave ($l = 0$) scattering dominates partial waves with higher angular momentum. Therefore we only consider s-wave scattering throughout the following chapters.

The general s-wave solution (up to a phase) to the Schrodinger equation in 3D is given by

$$\psi(r) = \frac{\sin(kr + \delta_k)}{r}, \quad (2.5)$$

2.3. Interactions with Hyperfine Spin Degrees of Freedom

Here δ_k is the s-wave phase shift which is determined by the details of the potential and the energy of scattering atoms. In the low energy limit, the phase shift δ_k can be expanded in a series of k^2 [1],

$$k \cot \delta_k = -1/a_s + \frac{1}{2}r_s k^2 + \dots \quad (2.6)$$

Here a_s is the scattering length of the potential and r_s is the effective range of the interaction potential.

By comparing Eq.2.5 and Eq.2.3, one can express the scattering amplitude in terms of the scattering length:

$$f_k = \frac{1}{k \cot \delta_k - ik} \quad (2.7)$$

$$\simeq -\frac{1}{a_s^{-1} + ik} \quad (2.8)$$

$$\rightarrow -a_s, \text{ when } k \rightarrow 0. \quad (2.9)$$

Thus the scattering amplitude is a constant $-a_s$ in low energy collisions, when the relevant energy in the question is much less than $\frac{\hbar^2}{ma_s^2}$. This condition is usually met in dilute gases except that a_s become divergent near resonances.

In theory it is often useful to replace the real and complicated interaction potential (as in Fig.2.1) by a simpler and analytical trackable potential, as long as these two potentials have the same scattering length. The new simple potential is often called effective potential, which can reproduce all the low energy physics as the original one. One simple choice of effective potential is the δ -function:

$$U(r) = \frac{4\pi\hbar a}{m} \delta(\mathbf{r}). \quad (2.10)$$

In first order Born approximation, the scattering matrix element is a constant $-a$, which coincides with the physical interaction with scattering length a .

2.3 Interactions with Hyperfine Spin Degrees of Freedom

Let's consider scattering problems with spin degrees of freedom. The hyperfine spin $\mathbf{F} = \mathbf{I} + \mathbf{S}$ is the sum of the nuclear spin I and the electronic spin S (electronic orbital angular momentum L is zero in our consideration). In

2.3. Interactions with Hyperfine Spin Degrees of Freedom

Table 2.1: Scattering lengths (in atomic units) of various alkali atoms. (Data sources: [140, 141, 142, 143, 68, 137])

isotopes	a_0	a_2	a_4
$F = 1, {}^{23}\text{Na}$	50.0 ± 1.6	55.0 ± 1.7	N.A.
$F = 1, {}^{87}\text{Rb}$	101.8 ± 0.2	100.4 ± 0.1	N.A.
$F = 2, {}^{23}\text{Na}$	34.9 ± 1.0	45.8 ± 1.1	64.5 ± 1.3
$F = 2, {}^{87}\text{Rb}$	89.4 ± 3.0	94.5 ± 3.0	106.0 ± 4.0
$F = 2, {}^{85}\text{Rb}$	-445.0^{+100}_{-300}	-440.0^{+150}_{-225}	-420.0^{+100}_{-140}
$F = 2, {}^{83}\text{Rb}$	83.0 ± 3.0	82.0 ± 3.0	81.0 ± 3.0

alkali atoms the electronic spin is always $1/2$, therefore the hyperfine spin F can be only in two sectors: $F = I \pm 1/2$. The coupling between nuclear and electronic magnetic moments will split these two sectors by a energy separation of several gigahertz or several millikelvins in many alkali atoms. This hyperfine splitting energy is three or four orders of magnitude larger than the typical temperature in ultracold experiments. Therefore the individual atom's hyperfine spin can be consider to be conserved in elastic scattering.

Note that in inelastic scattering processes atoms in the higher hyperfine spin sectors can be gradually brought to the lower hyperfine sectors, resulting in a relatively short lifetime of spinor gas in its higher hyperfine sector. In this case, the conservation of individual atom's hyperfine spin is still meaningful before severe spin loss takes place.

The total hyperfine spin of the two atoms is also conserved due to the rotational invariance of the central interaction. The selection rule arising from the rotational invariance is that two atoms's total spin \bar{F} and its zeeman components $m_{\bar{F}}$ is conserved. For example, two $F = 1$ bosons can have total spin $\bar{F} = 0, 2$ ($\bar{F} = 1$ is forbidden by the symmetry of Bose's statistics). Two atoms with total spin $\bar{F} = 2, m_{\bar{F}} = 0$ can not be scattered into $\bar{F} = 0$ or $\bar{F} = 2, m_{\bar{F}} = 1$ and vice versa.

As shown above, scattering channels labeled by $\bar{F}, m_{\bar{F}}$ are independent in low energy collisions, and we can introduce scattering amplitudes $-a_{\bar{F}, m_{\bar{F}}}$ for each channel. These scattering amplitudes should be independent of $m_{\bar{F}}$ since all the channels with the same \bar{F} can be transformed to each other by rotations.

Spin-mixing scattering can be understood in this framework, for example, let's consider two $F = 1$ bosonic atoms initially in $m_F = +1$ and $m_F = -1$ state. It is a linear superposition of two channels as $\alpha|\bar{F} = 2, m_{\bar{F}} = 0\rangle + \beta|\bar{F} = 0, m_{\bar{F}} = 0\rangle$. Since these two channels usually scatter

2.4. Vector and Tensor Algebra and Representations

with different scattering lengths, the states after scattering will be $\alpha'|\bar{F} = 2, m_{\bar{F}} = 0\rangle + \beta'|\bar{F} = 0, m_{\bar{F}} = 0\rangle$ with $\frac{\alpha'}{\beta'} \neq \frac{\alpha}{\beta}$, including different spin states such as $|m_F = 0\rangle \otimes |m_F = 0\rangle$.

Physically, the hyperfine spin-mixing scattering is due to the electronic spin exchange effects, in particular at short distances. From Fig.2.1 one can see that at short distances the energy difference between electronic spin singlet and electronic spin triplet is of order of 10^3K which is large compared to hyperfine splitting of order 10^{-3}K . When two atoms are close enough, the electronic spin exchange energy dominates the hyperfine splitting interaction, resulting in a coupling of different hyperfine levels.

These spin-dependent scattering lengths contain the complete information of low energy collisions. Actually one can construct an effective interaction that serves as the starting point of many theoretical analysis. The two-body effective interaction can be expressed in the following form,

$$U(r) = \frac{4\pi}{m} \delta(\mathbf{r}) \sum_{\bar{F}} a_{\bar{F}} \mathcal{P}_{\bar{F}}. \quad (2.11)$$

Here $\mathcal{P}_{\bar{F}}$ is the operator that projects out the total spin \bar{F} . It is also more useful to write spin projection operator explicitly by using second quantization forms, especially when F is specified.

2.4 Vector and Tensor Algebra and Representations

For a given F , one can introduce annihilation and creation operators $\hat{\psi}_m$ and $\hat{\psi}_m^\dagger$ associated with each zeeman level $m = -F, -F + 1, \dots, F - 1, F$. They satisfy the following commutation rules:

$$[\hat{\psi}_m(r), \hat{\psi}_{m'}(r')] = [\hat{\psi}_m^\dagger(r), \hat{\psi}_{m'}^\dagger(r')] = 0 \quad (2.12)$$

$$[\hat{\psi}_m(r), \hat{\psi}_{m'}^\dagger(r')] = \delta_{m,m'} \delta(r - r') \quad (2.13)$$

The key to write down the effective interaction with hyperfine spins is the rotational symmetry. A general form of two-body contact interaction is

$$A_{\alpha\beta\gamma\delta} \hat{\psi}_\alpha^\dagger \hat{\psi}_\beta^\dagger \hat{\psi}_\gamma \hat{\psi}_\delta. \quad (2.14)$$

Here $\alpha, \beta, \gamma, \delta$ are hyperfine sub-states. The rotational symmetry has put a strong constraint on the form of $A_{\alpha\beta\gamma\delta}$ such that after a rotation R in

2.4. Vector and Tensor Algebra and Representations

which $\hat{\psi}_\alpha \rightarrow R_{\alpha\alpha'}\hat{\psi}_{\alpha'}$, the effective interaction should be in the same form as Eq.2.14. It requires that

$$A_{\alpha\beta\gamma\delta} = R_{\alpha\alpha'}R_{\beta\beta'}R_{\gamma\gamma'}R_{\delta\delta'}A_{\alpha'\beta'\gamma'\delta'} \quad (2.15)$$

The number of invariant interactions under the above constraint is limited, compared to situations without such a constraint. Actually the number of possible interaction terms is $F + 1$, which is exactly the number of independent scattering channels that two hyperfine spin F atoms can have. For example it can be shown there are only two terms for $F = 1$ atoms and only three terms for $F = 2$ atoms.

In the following, I will present the second quantization form of the effective interaction for hyperfine spin $F = 1$ and $F = 2$, which are frequently used in later chapters. For $F = 3$ (^{53}Cr) and even higher hyperfine spins, similar formulas can be obtained (see [144, 145]).

2.4.1 F=1

The effective interaction can be written as:

$$\hat{U}(r) = \frac{1}{2} \left[c_0(\hat{\rho}^2 - \hat{\rho}) + c_2(\hat{F}^2 - 2\hat{\rho}) \right]. \quad (2.16)$$

Here $\hat{\rho}$ and \hat{F}^2 is the total density and total spin operator:

$$\hat{\rho} = \psi_{-1}^\dagger\psi_{-1} + \psi_0^\dagger\psi_0 + \psi_1^\dagger\psi_1 \quad (2.17)$$

$$\hat{F}^2 = 2\hat{\rho} + 2\hat{\psi}_0^\dagger\hat{\psi}_0(\hat{\psi}_1^\dagger\hat{\psi}_1 + \hat{\psi}_{-1}^\dagger\hat{\psi}_{-1}) + (\hat{\psi}_1^\dagger\hat{\psi}_1 - \hat{\psi}_{-1}^\dagger\hat{\psi}_{-1})^2 \quad (2.18)$$

$$+ 2(\hat{\psi}_0^\dagger\hat{\psi}_0^\dagger\hat{\psi}_1\hat{\psi}_{-1} + \text{h.c.}). \quad (2.19)$$

The second line in the above expansion of F^2 clearly shows the spin-mixing coupling as $|0, 0\rangle \rightleftharpoons | + 1, -1\rangle$.

Sometimes it is more convenient to introduce a vector representation via which one can write a compact form of interaction:

$$\begin{pmatrix} \hat{\psi}_x^\dagger \\ \hat{\psi}_y^\dagger \\ \hat{\psi}_z^\dagger \end{pmatrix} = \begin{pmatrix} \frac{1}{\sqrt{2}} & \frac{1}{\sqrt{2}} & 0 \\ \frac{-i}{\sqrt{2}} & \frac{i}{\sqrt{2}} & 0 \\ 0 & 0 & 1 \end{pmatrix} \begin{pmatrix} \hat{\psi}_1^\dagger \\ \hat{\psi}_{-1}^\dagger \\ \hat{\psi}_0^\dagger \end{pmatrix}, \quad (2.20)$$

and

$$\begin{pmatrix} \hat{\psi}_1^\dagger \\ \hat{\psi}_{-1}^\dagger \\ \hat{\psi}_0^\dagger \end{pmatrix} = \begin{pmatrix} \frac{1}{\sqrt{2}} & \frac{i}{\sqrt{2}} & 0 \\ \frac{1}{\sqrt{2}} & \frac{-i}{\sqrt{2}} & 0 \\ 0 & 0 & 1 \end{pmatrix} \begin{pmatrix} \hat{\psi}_x^\dagger \\ \hat{\psi}_y^\dagger \\ \hat{\psi}_z^\dagger \end{pmatrix}. \quad (2.21)$$

2.4. Vector and Tensor Algebra and Representations

The total density $\hat{\rho}$ and spin operator \hat{F}_α along $\alpha = x, y, z$ can be written as:

$$\hat{\rho} = \hat{\psi}_\alpha^\dagger \hat{\psi}_\alpha \quad (2.22)$$

$$\hat{F}_\alpha = -i\epsilon_{\alpha\beta\gamma} \hat{\psi}_\beta^\dagger \hat{\psi}_\gamma \quad (2.23)$$

$$\hat{F}^2 = \hat{F}_\alpha \hat{F}_\alpha = \hat{\rho}^2 - \hat{\psi}_\alpha^\dagger \hat{\psi}_\alpha^\dagger \hat{\psi}_\beta \hat{\psi}_\beta + 2\hat{\rho}. \quad (2.24)$$

Here $\epsilon_{\alpha\beta\gamma}$ is the antisymmetric unit tensor.

The coupling constant appearing in the interaction c_0 and c_2 can be expressed in terms of spin-dependent scattering lengths:

$$c_0 = \frac{4\pi\hbar^2}{m} \frac{a_0 + 2a_2}{3} \quad (2.25)$$

$$c_2 = \frac{4\pi\hbar^2}{m} \frac{a_2 - a_0}{3}. \quad (2.26)$$

2.4.2 F=2

The effective interaction can be written as

$$\hat{U} = \frac{a}{2}(\hat{\rho}^2 - \hat{\rho}) + \frac{b}{2}(\hat{F}^2 - 6\hat{\rho}) + 5c\hat{\mathcal{D}}^\dagger \hat{\mathcal{D}} \quad (2.27)$$

Here $\hat{\rho}$ is the total density, \hat{F} is the total spin, and $\hat{\mathcal{D}}^\dagger$ is the spin dimer creation operator which creates a spin singlet dimer (with total spin zero).

One can write down explicitly in terms

$$\hat{\rho} = \sum_{m=-2}^{+2} \hat{\psi}_m^\dagger \hat{\psi}_m \quad (2.28)$$

$$\hat{\mathcal{D}} = \frac{1}{\sqrt{10}} \left(2\hat{\psi}_{+2}\hat{\psi}_{-2} - 2\hat{\psi}_{+1}\hat{\psi}_{-1} + \hat{\psi}_0\hat{\psi}_0 \right) \quad (2.29)$$

$$\hat{F}^2 = (2\hat{\psi}_{+2}^\dagger \hat{\psi}_{+1} + \sqrt{6}\hat{\psi}_{+1}^\dagger \hat{\psi}_0 + \sqrt{6}\hat{\psi}_0^\dagger \hat{\psi}_{-1} + 2\hat{\psi}_{-1}^\dagger \hat{\psi}_{-2}) \quad (2.30)$$

$$\cdot (2\hat{\psi}_{+1}^\dagger \hat{\psi}_{+2} + \sqrt{6}\hat{\psi}_0^\dagger \hat{\psi}_{+1} + \sqrt{6}\hat{\psi}_{-1}^\dagger \hat{\psi}_0 + 2\hat{\psi}_{-2}^\dagger \hat{\psi}_{-1}) \quad (2.31)$$

$$+ (2\hat{\psi}_{+2}^\dagger \hat{\psi}_{+2} + \hat{\psi}_{+1}^\dagger \hat{\psi}_{+1} - \hat{\psi}_{-1}^\dagger \hat{\psi}_{-1} - 2\hat{\psi}_{-2}^\dagger \hat{\psi}_{-2})^2 \quad (2.32)$$

$$- (2\hat{\psi}_{+2}^\dagger \hat{\psi}_{+2} + \hat{\psi}_{+1}^\dagger \hat{\psi}_{+1} - \hat{\psi}_{-1}^\dagger \hat{\psi}_{-1} - 2\hat{\psi}_{-2}^\dagger \hat{\psi}_{-2}) \quad (2.33)$$

As one can see, there are spin-mixing matrix elements corresponding to $|0, 0\rangle \rightleftharpoons | +1, -1\rangle \rightleftharpoons | +2, -2\rangle$ and also $| +1, +1\rangle \rightleftharpoons | +2, 0\rangle$. These matrix elements can be directly studied and measured in few-body spin-mixing dynamics in experiments[96, 97].

2.4. Vector and Tensor Algebra and Representations

It is convenient to introduce a tensor representation[146] As one can see later, this representation is useful when discussing magnetic structures in rotational symmetry breaking states.

$$\hat{\psi}_{xx}^\dagger = \frac{1}{\sqrt{2}}(\hat{\psi}_{-2}^\dagger + \hat{\psi}_2^\dagger) - \frac{1}{\sqrt{3}}\hat{\psi}_0^\dagger, \quad (2.34)$$

$$\hat{\psi}_{yy}^\dagger = -\frac{1}{\sqrt{2}}(\hat{\psi}_{-2}^\dagger + \hat{\psi}_2^\dagger) - \frac{1}{\sqrt{3}}\hat{\psi}_0^\dagger, \quad (2.35)$$

$$\hat{\psi}_{zz}^\dagger = \frac{2}{\sqrt{3}}\hat{\psi}_0^\dagger, \quad (2.36)$$

$$\hat{\psi}_{xy}^\dagger = \frac{i}{\sqrt{2}}(\hat{\psi}_{-2}^\dagger - \hat{\psi}_2^\dagger) \quad (2.37)$$

$$\hat{\psi}_{xz}^\dagger = \frac{1}{\sqrt{2}}(\hat{\psi}_{-1}^\dagger - \hat{\psi}_1^\dagger) \quad (2.38)$$

$$\hat{\psi}_{yz}^\dagger = -\frac{i}{\sqrt{2}}(\hat{\psi}_{-1}^\dagger + \hat{\psi}_1^\dagger), \quad (2.39)$$

The corresponding annihilation operators can be introduced in the same way. These operators have the following properties [134]:

$$[\hat{\psi}_{\alpha\beta}, \hat{\psi}_{\alpha'\beta'}^\dagger] = \delta_{\alpha\alpha'}\delta_{\beta\beta'} + \delta_{\alpha\beta'}\delta_{\beta\alpha'} - \frac{2}{3}\delta_{\alpha\beta}\delta_{\alpha'\beta'} \quad (2.40)$$

$$\sum_{\alpha} \hat{\psi}_{\alpha\alpha} = 0. \quad (2.41)$$

This last property puts a constraint on the constructions of linear operators. For operators

$$\text{Tr}[\Delta\hat{\psi}] = \sum_{\alpha,\beta} \Delta_{\alpha\beta}\hat{\psi}_{\beta\alpha}, \quad (2.42)$$

the tensor Δ can be always reduced to a traceless one, i.e.,

$$\text{Tr}[\Delta] = \sum_{\alpha} \Delta_{\alpha\alpha} = 0. \quad (2.43)$$

This constraint is needed, because when introducing this new basis we have enlarged the Hilbert space by constructing six operators out of five. This constraint brings the size of the physical Hilbert space back to the original one.

The density operator $\hat{\rho}$ in terms of the new operators can be derived as:

$$\hat{\rho} = \sum_m \hat{\psi}_m^\dagger \hat{\psi}_m = \frac{1}{2} \text{Tr}[\hat{\psi}^\dagger \hat{\psi}] = \frac{1}{2} \sum_{\alpha,\beta} \hat{\psi}_{\alpha\beta}^\dagger \hat{\psi}_{\beta\alpha}. \quad (2.44)$$

2.4. Vector and Tensor Algebra and Representations

The factor $\frac{1}{2}$ appears here because the trace involves a double sum over the operator $\hat{\psi}_{\alpha\beta}$. This same factor will appear later when deriving the hopping term in the Hamiltonian.

The spin operator is straightforwardly derived as:

$$\hat{F}_\alpha = -i\epsilon_{\alpha\beta\gamma}\hat{\psi}_{\beta\eta}^\dagger\hat{\psi}_{\eta\gamma}. \quad (2.45)$$

It has the following properties:

$$[\hat{F}_\alpha, \hat{F}_\beta] = i\epsilon_{\alpha\beta\gamma}\hat{F}_\gamma, \quad (2.46)$$

$$[\hat{F}_\alpha, \hat{\rho}] = 0 \quad (2.47)$$

$$[\hat{F}_\alpha, \text{Tr}[(\hat{\psi}^\dagger)^n]] = 0. \quad (2.48)$$

The total spin operator is then given by:

$$\hat{F}^2 = \hat{F}_\alpha\hat{F}_\alpha \quad (2.49)$$

$$= \hat{\psi}_{\beta\eta}^\dagger\hat{\psi}_{\eta\gamma}\hat{\psi}_{\gamma\xi}^\dagger\hat{\psi}_{\xi\beta} - \hat{\psi}_{\beta\eta}^\dagger\hat{\psi}_{\eta\gamma}\hat{\psi}_{\beta\xi}^\dagger\hat{\psi}_{\xi\gamma} \quad (2.50)$$

The dimer creation operator in the new representation is:

$$\hat{\mathcal{D}}^\dagger = \frac{1}{\sqrt{40}}\text{Tr}[(\hat{\psi}^\dagger)^2], \quad (2.51)$$

which has the following properties:

$$[\hat{\mathcal{D}}, \hat{\mathcal{D}}^\dagger] = 1 + \frac{2}{5}\hat{\rho}. \quad (2.52)$$

This operator creates two particles which together form a spin singlet. In the same way one can construct an operator which creates three particles which together form a singlet. This is called the trimer operator and defined as

$$\hat{\mathcal{T}}^\dagger = \frac{1}{\sqrt{140}}\text{Tr}[(\hat{\psi}^\dagger)^3]. \quad (2.53)$$

The coupling constants a , b and c in Eq.2.27 can be related to scattering lengths a_F in total spin $F = 0, 2, 4$ channels as:

$$a = \frac{4\pi\hbar^2}{m} \frac{4a_2 + 3a_4}{7} \quad (2.54)$$

$$b = \frac{4\pi\hbar^2}{m} \frac{a_4 - a_2}{7} \quad (2.55)$$

$$c = \frac{4\pi\hbar^2}{m} \left(\frac{a_0 - a_4}{5} - 2\frac{a_2 - a_4}{7} \right). \quad (2.56)$$

2.5. Linear and Quadratic Zeeman Shift

These equations are obtained by matching a_F to the scattering amplitudes calculated from from Eq. 2.27. For example for the spin-single state $\Psi_0 = \mathcal{D}^\dagger|0\rangle$, one can have

$$\frac{4\pi\hbar^2 a_0}{m} = \langle \Psi_0 | \hat{U} | \Psi_0 \rangle = a - 6b + 5c \quad (2.57)$$

Similarly, for the $F = 4$ state such as $\Psi_4 = \frac{1}{\sqrt{2}}\hat{\psi}_2^\dagger\hat{\psi}_2^\dagger|0\rangle$, and the $F = 2$ state such as $\Psi_2 = \frac{1}{10}(\sqrt{6}\hat{\psi}_2^\dagger\hat{\psi}_0^\dagger - \hat{\psi}_1^\dagger\hat{\psi}_1^\dagger)|0\rangle$ one can have

$$\frac{4\pi\hbar^2 a_4}{m} = \langle \Psi_4 | \hat{U} | \Psi_4 \rangle = a + 4b \quad (2.58)$$

$$\frac{4\pi\hbar^2 a_2}{m} = \langle \Psi_2 | \hat{U} | \Psi_2 \rangle = a - 3b. \quad (2.59)$$

By solving the three equations above Eq.2.57-2.59, one can immediately obtain the relations shown above.

2.5 Linear and Quadratic Zeeman Shift

Let's consider an atom with nuclear spin I and electronic spin S in the presence of a magnetic field along the z direction. Here we assume that the atom is in its electronic ground state so the orbital angular momentum is zero.

$$H_s = \mathbf{A}\mathbf{I} \cdot \mathbf{S} + CS_z + DI_z. \quad (2.60)$$

For ^{87}Rb , $|I| = \frac{3}{2}$ and $|S| = \frac{1}{2}$. A is the hyperfine coupling constant and is equal to one half of the hyperfine splitting Δ_{hf} between $F = 1$ and $F = 2$ states. Constants C and D are given by

$$C = 2\mu_B B, D = -\frac{\mu}{I}B, \quad (2.61)$$

where μ is the nuclear magnetic moment and is equal to $2.7\mu_N$ for ^{87}Rb . We have $C \simeq 2\text{MHz}$ and $D \simeq 1\text{kHz}$ when $B = 1\text{G}$. Since $|\frac{C}{D}| \sim \frac{m_p}{m_e} \simeq 2000$, for most applications D can be neglected. The eigenstates of the above spin Hamiltonian can be labeled by their total spin F and F_z . $E(F, F_z)$ as a function of A, C are given by:

$$E(2, +2) = \frac{3}{4}A + \frac{1}{2}C,$$

2.5. Linear and Quadratic Zeeman Shift

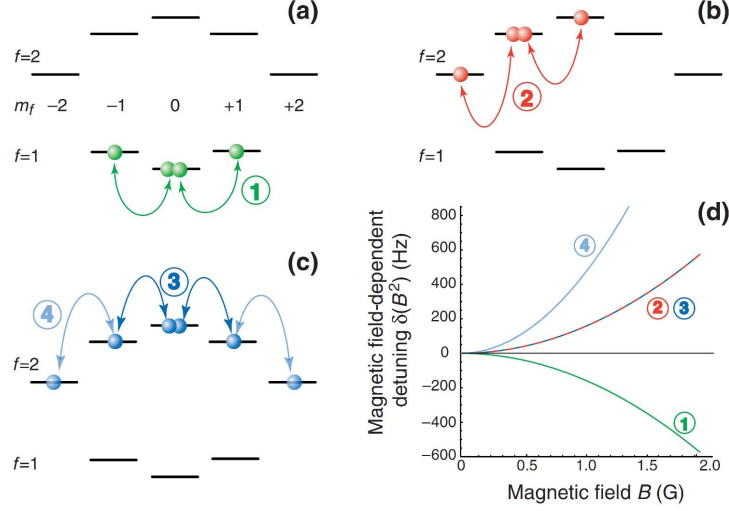


Figure 2.2: (a)-(c) Shift of hyperfine spin energy levels due to the quadratic Zeeman effects in hyperfine $F = 1$ and $F = 2$ ^{87}Rb atoms. (d) Corresponding Zeeman energy for selected combinations of two-particle states versus magnetic fields[97].

$$\begin{aligned}
 E(2, -2) &= \frac{3}{4}A - \frac{1}{2}C, \\
 E(2, +1) &= -\frac{1}{4}A + \sqrt{\frac{3}{4}A^2 + \frac{1}{4}(A + C)^2}, \\
 E(1, +1) &= -\frac{1}{4}A - \sqrt{\frac{3}{4}A^2 + \frac{1}{4}(A + C)^2}, \\
 E(2, -1) &= -\frac{1}{4}A + \sqrt{\frac{3}{4}A^2 + \frac{1}{4}(A - C)^2}, \\
 E(1, -1) &= -\frac{1}{4}A - \sqrt{\frac{3}{4}A^2 + \frac{1}{4}(A - C)^2}, \\
 E(2, 0) &= -\frac{1}{4}A + \sqrt{A^2 + \frac{1}{4}C^2}, \\
 E(1, 0) &= -\frac{1}{4}A - \sqrt{A^2 + \frac{1}{4}C^2}.
 \end{aligned} \tag{2.62}$$

When the zeeman coupling C is much less than the hyperfine coupling A (which is true for many experiments), one can make an expansion in terms

2.5. Linear and Quadratic Zeeman Shift

of $\frac{C}{A}$ and keeping terms to the second order:

$$\begin{aligned}
 E(2, \pm 2) &= \frac{3}{4}A \pm \frac{1}{2}C, \\
 E(2, \pm 1) &= \frac{3}{4}A \pm \frac{1}{4}C + \frac{3C^2}{32A}, \\
 E(2, 0) &= \frac{3}{4}A + \frac{C^2}{8A}, \\
 E(1, \pm 1) &= -\frac{5}{4}A \mp \frac{1}{4}C - \frac{3C^2}{32A}, \\
 E(1, 0) &= -\frac{5}{4}A - \frac{C^2}{8A}.
 \end{aligned} \tag{2.63}$$

We can rewrite the energy levels in a more compact form as

$$\begin{aligned}
 E(2, m_F) &= \frac{3}{4}A + \frac{C^2}{8A} + \frac{C}{4}m_F - \frac{C^2}{32A}m_F^2 \\
 E(1, m_F) &= -\frac{5}{4}A - \frac{C^2}{8A} - \frac{C}{4}m_F + \frac{C^2}{32A}m_F^2.
 \end{aligned} \tag{2.64}$$

The linear Zeeman effects are not important in spin-changing collisions. Although the m_F for each spin is changed during the collision, the total spin moment is conserved. As a result, the linear Zeeman energy does not change in these collisions. In this case the leads effect of magnetic fields is thus coming from the second order Zeeman effects or the quadratic Zeeman effects.

In the second quantization form introduced in the previous section, second order Zeeman effects can be cast

$$H_{QB} = \delta_B \sum_{m=-F}^{+F} m^2 \psi_m^\dagger \psi_m. \tag{2.65}$$

$$\delta_B = \pm \frac{C^2}{32A} = \pm \frac{(\mu_B B)^2}{4\Delta_{hf}}, \quad F = 1 \text{ or } 2 \tag{2.66}$$

We can also write the H_B in the vector representation. For $F = 1$

$$H_{QB} = \delta_B \left(\rho - \psi_z^\dagger \psi_z \right); \tag{2.67}$$

and for $F = 2$

$$H_{QB} = \delta_B \left(2\rho - 2\psi_{zz}^\dagger \psi_{zz} + \sum_{\eta=x,y} \psi_{z\eta}^\dagger \psi_{\eta z} \right). \tag{2.68}$$

Chapter 3

Fluctuation-Induced Uniaxial and Biaxial Nematic States in $F = 2$ Spinor Condensates

3.1 Introduction

The spin nematic condensate is a state that breaks the rotational symmetry but not the translational symmetry, in which most of the spins align themselves along a particular axis. Spin nematic states are fascinating because of the rich topology of their order parameter space (also known as “manifold”), which gives rise to exotic topological defects such as quantum vortices with fractional circulation integrals. Although spin nematics haven’t been successfully realized in conventional solid state systems, it is widely believed that at least some of them are likely to be created and observed in cold atomic gases. For example, nematic states are predicted to be the ground state in the spin-one condensates with anti-ferromagnetic interactions[107, 108], and they have also been studied in experiments[38]. For spin-two condensates a family of degenerate nematic states with d-wave symmetries[147] are predicted by the mean field theory[107, 108].

In this chapter I will examine the effects of zero-point fluctuations on nematic correlations. Zero-point fluctuations are known to lead a wide range of physical phenomena, including the Lamb shift[7], the Coleman-Weinberg mechanism of spontaneously symmetry breaking[11], fluctuation-induced first order transitions in liquid crystals and superconductors[148], and “order-by-disorder” in magnetic systems[12, 13, 14]. It turns out that the zero-point spin fluctuations in $F = 2$ nematic condensates can lift the accidental degeneracy and select out two states with distinct symmetries: a uniaxial nematic state which is rotational invariant along its symmetry axis, and a biaxial nematic state with D_{2h} symmetry.

In Sec.3.2, I present the results obtained previously in mean field theories. In Sec.3.3, I examine the quantum fluctuations in the nematic states. The

quantum fluctuations studied here can be viewed as zero-point motion of mean field collective modes. Bogoliubov quasi-particles, quantized version of the mean field modes, are also analyzed. In Sec.3.4, I examine the topology of the uniaxial and biaxial nematic states. In Sec.3.5, I conclude the chapter by a brief discussion of the amplitude of fluctuations, which will be studied in more detail in the next chapter.

3.2 Mean Field Theory of $F=2$ Condensates

In this section, we will examine spontaneous magnetic ordering of mean field ground states, without the presence of Zeeman fields. These results are obtained previously in [141, 112]. It is shown that there are three types of possible phases for a spin-two spinor Bose condensate. These phases are spontaneous rotation symmetry broken states characterized by their magnetizations, spin quadrupole moments and singlet pair amplitudes (summarized in Tab.3.1). We will also look at the topology of ground state manifolds which are possible to host fractionalized quantum vortices.

We consider atoms loaded in optical lattices described by the following Hamiltonian:

$$\begin{aligned} \mathcal{H} = & \sum_k \left(\frac{a_L}{2} (\hat{\rho}_k^2 - \hat{\rho}_k) + \frac{b_L}{2} (\hat{\mathcal{F}}_k^2 - 6\hat{\rho}_k) + 5c_L \mathcal{D}_k^\dagger \mathcal{D}_k \right) \\ & - t_L \sum_{\langle kl \rangle} \left(\psi_{k,\alpha\beta}^\dagger \psi_{l,\beta\alpha} + \text{h.c.} \right) - \mu \sum_k \hat{\rho}_k. \end{aligned} \quad (3.1)$$

Here k is the lattice site index and $\langle kl \rangle$ are the nearest neighbor sites, μ is the chemical potential and t_L is the one-particle hopping amplitude; a_L , b_L and c_L are three interaction constants that are dependent both on optical lattices and atomic species.

In the mean field approximation, one can replace the operator by their expectation values or the associated condensates amplitudes. The amplitude of a condensate is a traceless symmetric tensor,

$$\tilde{\chi}_{\alpha\beta} = \langle \hat{\psi}_{k,\alpha\beta} \rangle. \quad (3.2)$$

In this condensate, atoms occupy a one-particle spin state $|\tilde{\chi}\rangle$ that is defined as a linear superposition of five $F = 2$ hyperfine states $|2, m_F\rangle$ or ψ_{m_F}

$$\begin{aligned} |\tilde{\chi}\rangle &= \sum_{\alpha\beta, m_F} \tilde{\chi}_{\alpha\beta} \mathcal{C}_{\alpha\beta, m_F} \psi_{m_F}, \\ \mathcal{C}_{\alpha\beta, m_F} &= \sqrt{\frac{15}{4\pi}} \int d\Omega \left(n_\alpha n_\beta - \frac{1}{3} \delta_{\alpha\beta} \right) Y_{2, m_F}^*(\theta, \phi). \end{aligned} \quad (3.3)$$

3.2. Mean Field Theory of $F=2$ Condensates

Table 3.1: Magnetic orderings in mean field ground states of $F = 2$ spinor condensates. \mathcal{D}_k , $\hat{\mathcal{F}}_k$ and $\hat{\mathcal{O}}_k$ are spin single annihilation operator, spin operator and spin quadrupole moment respectively. Their definition can be found in Sec.2.4.2 of Chap.2 and in Eq.3.15.

	Nematic	Cyclic	Ferromagnetic
$\langle \psi_{m_F} \rangle \sim$	$(\sin \xi, 0, \sqrt{2} \cos \xi, 0, \sin \xi)$	$(1, 0, -3\sqrt{2}i, 0, 1)$	$(1, 0, 0, 0, 0)$
$\langle \mathcal{D}_k \rangle$	$\neq 0$	0	0
$\langle \hat{\mathcal{F}}_k \rangle$	0	0	$\neq 0$
$\langle \hat{\mathcal{O}}_k \rangle$	$\neq 0$	0	$\neq 0$

Here n_α , $\alpha = x, y, z$, are components of a unit vector $\mathbf{n}(\theta, \phi)$; $n_x = \sin \theta \cos \phi$, $n_y = \sin \theta \sin \phi$ and $n_z = \cos \theta$. Y_{2,m_F} , $m_F = 0, \pm 1, \pm 2$ are five spherical harmonics with $l = 2$.

The mean field energy per site as a function of $\tilde{\chi}$ can be obtained as

$$E_{MF} = \frac{a_L}{8} \text{Tr}(\tilde{\chi}^* \tilde{\chi}) \text{Tr}(\tilde{\chi}^* \tilde{\chi}) + \frac{c_L}{8} \text{Tr}(\tilde{\chi}^* \tilde{\chi}^*) \text{Tr}(\tilde{\chi} \tilde{\chi}) + \frac{b_L}{4} \text{Tr}[\tilde{\chi}^*, \tilde{\chi}]^2 - z t_L \text{Tr}(\tilde{\chi}^* \tilde{\chi}) - \frac{\mu}{2} \text{Tr}(\tilde{\chi}^* \tilde{\chi}), \quad (3.4)$$

where z is the coordination number.

Minimization of E_{MF} with respect to the tensor $\tilde{\chi}$ yields nematic, cyclic and ferromagnetic phases. In the following sections we will examine these states and their magnetic properties in detail.

Here, we plot the wavefunctions of various spin nematic states in Fig.3.1(a) and also the mean field phase diagram including all three types of phases in Fig.3.1(b). Spin wavefunctions Ψ_S are represented by the usual spherical harmonics. For example, from a spinor condensate with condensate amplitude ψ_m one can construct the following spin wavefunction

$$\Psi_S(\theta, \phi) = \sum_{m=-l}^l \psi_m Y_{l,m}(\theta, \phi). \quad (3.5)$$

One can also use the tensor form of condensate amplitude ξ to get a compact expression

$$\Psi_S = \sqrt{\frac{15}{4\pi}} \sum_{\alpha\beta} \chi_{\alpha\beta} n_\alpha n_\beta. \quad (3.6)$$

Here n_α , $\alpha = x, y, z$ are components of a unit vector $\mathbf{n}(\theta, \phi)$.

3.2. Mean Field Theory of $F=2$ Condensates

Table 3.2: Scattering lengths (in atomic units) of various alkali isotopes with hyperfine spin $F = 2$. (Data sources: [141, 68, 137])

isotopes	a_0	a_2	a_4
^{23}Na	34.9 ± 1.0	45.8 ± 1.1	64.5 ± 1.3
^{87}Rb	89.4 ± 3.0	94.5 ± 3.0	106.0 ± 4.0
^{85}Rb	-445.0^{+100}_{-300}	-440.0^{+150}_{-225}	-420.0^{+100}_{-140}
^{83}Rb	83.0 ± 3	82.0 ± 3	81.0 ± 3

Note that the coordinates θ and ϕ represent the spin degrees of freedom, not the spatial orientations. However, these spin wavefunctions transform the same way as spatial orbital wavefunction under an $\text{SO}(3)$ rotation, providing an intuitive picture of symmetry properties of nematic states.

3.2.1 Ferromagnetic States

In the ferromagnetic phase (when $b_L < 0, c_L > 4b_L$), the spinor condensate breaks the rotation symmetry spontaneously through its non-zero magnetization.

$$\begin{aligned} \langle \hat{\mathcal{F}}_k \rangle &\neq 0 \\ \langle \hat{\mathcal{D}}_k \rangle &= 0 \end{aligned} \quad (3.7)$$

The condensate amplitude is specified by the following matrix up to an $\text{SO}(3)$ rotation and phase.

$$\tilde{\chi} = \sqrt{\frac{M}{2}} \begin{pmatrix} 1 & -i & 0 \\ -i & -1 & 0 \\ 0 & 0 & 0 \end{pmatrix}$$

Here M is the average number of atoms per site or $M = \langle \hat{\rho}_k \rangle$. In the representation of Zeeman spin levels, we have

$$\langle \hat{\psi}_{m_F} \rangle = \sqrt{M} (1, 0, 0, 0, 0) \quad (3.8)$$

One can see only integer quantum vortices are allowed in ferromagnetic states.

3.2.2 Cyclic States

The cyclic state (when $b_L > 0, c_L > 0$) also breaks the rotation symmetry through a nonzero spin quadrupole moment $\langle \hat{O}_{k,\alpha\beta} \rangle = \langle \hat{\mathcal{F}}_{k,\alpha} \hat{\mathcal{F}}_{k,\beta} \rangle -$

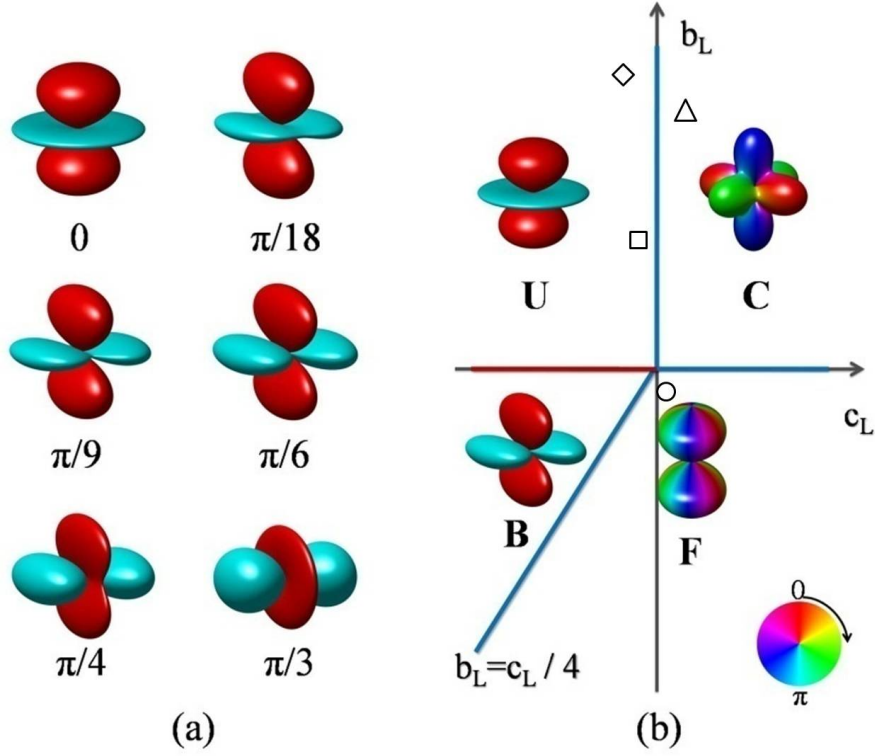


Figure 3.1: (Color online) (a) Wavefunctions of spin nematics at various ξ . $\xi = 0, \frac{\pi}{3}, \frac{2\pi}{3}, \dots$ are wavefunctions of uniaxial spin nematics (labeled as ‘U’), and $\xi = \frac{\pi}{6}, \frac{5\pi}{6}, \frac{9\pi}{6}, \dots$ are biaxial spin nematics (labeled as ‘B’) with D_{2h} symmetries. These spin wavefunctions Ψ_S are represented by spherical harmonic functions (see text). Colors indicate the phase of wavefunctions. (b) Ferromagnetic (labeled as ‘F’), cyclic (labeled as ‘C’) and nematic states in the mean field theory are separated by blue boundaries; uniaxial and biaxial nematics when taking into account of quantum fluctuations are separated by red lines. The locations of various isotopes on this diagram are located as: $\diamond = ^{23}\text{Na}$, $\triangle = ^{85}\text{Rb}$, $\square = ^{87}\text{Rb}$ and $\circ = ^{83}\text{Rb}$ (see Tab.3.2).

3.2. Mean Field Theory of $F=2$ Condensates

$$\frac{1}{3}\delta_{\alpha\beta}\langle\hat{\mathcal{F}}^2\rangle.$$

$$\begin{aligned}\langle\hat{\mathcal{F}}_k\rangle &= 0 \\ \langle\mathcal{D}_k\rangle &= 0 \\ \langle\hat{\mathcal{O}}_k\rangle &\neq 0\end{aligned}\tag{3.9}$$

The condensate amplitude up to a $\text{SO}(3)$ rotation and a phase is:

$$\tilde{\chi} = \sqrt{\frac{2M}{3}} \begin{pmatrix} 1 & 0 & 0 \\ 0 & e^{\frac{2\pi i}{3}} & 0 \\ 0 & 0 & e^{\frac{4\pi i}{3}} \end{pmatrix}$$

or

$$\psi_{m_F} = \sqrt{\frac{M}{20}} e^{-\frac{\pi}{6}i} (1, 0, -3\sqrt{2}i, 0, 1)\tag{3.10}$$

It is pointed out that $\frac{1}{3}$ quantum vortex is possible in the cyclic states due to the special topology of the submanifold[125]. A detailed analysis shows that the manifold of the cyclic states have the structure: $\frac{\text{SO}(3)\times\text{U}(1)}{T}$. Here $\text{U}(1)$ is for the phase, $\text{SO}(3)$ is the rotation, and T is the Tetrahedral group composed of all twelve rotations that keep a tetrahedral invariant. Distinct quantum vortices then can be identified with their free homotopy classes, which coincide with conjugacy classes of the based homotopy group [126, 149].

In a more physically transparent way, the fractionalized quantum vortex here is possible due to the Berry phase associated with rotations. Note that the cyclic state specified by Eq.3.10 is invariant up to a Berry phase under an $\text{SO}(3)$ rotation \mathcal{R} around $x = y = z$ of $\frac{2\pi}{3}$,

$$\tilde{\chi} \rightarrow \mathcal{R}\tilde{\chi}\mathcal{R}^T = e^{-\frac{2\pi}{3}i}\tilde{\chi}, \quad \mathcal{R} = \begin{pmatrix} 0 & 0 & 1 \\ 1 & 0 & 0 \\ 0 & 1 & 0 \end{pmatrix}$$

Therefore, a $1/3$ quantum vortex is constructed by arranging the spinor condensates along a closed loop such that the total phase winding is $\frac{2\pi}{3}$ and total spin rotation is \mathcal{R} given above.

3.2.3 Nematic States

Particularly when $c_L < 0, c_L < 4b_L$, minimization of energy in Eq.(3.4) requires that $\tilde{\chi}$ be a real symmetric tensor (up to a phase). An arbitrary

3.2. Mean Field Theory of $F=2$ Condensates

solution $\tilde{\chi}$ can be obtained by applying an $SO(3)$ rotation and a $U(1)$ gauge transformation to a real diagonal matrix χ ,

$$\tilde{\chi} = \sqrt{4M} e^{i\phi} \mathcal{R} \chi \mathcal{R}^{-1}; \quad (3.11)$$

\mathcal{R} is an $SO(3)$ rotation matrix, and χ is a normalized real diagonal traceless matrix[134],

$$\chi = \begin{pmatrix} \chi_{xx} & 0 & 0 \\ 0 & \chi_{yy} & 0 \\ 0 & 0 & \chi_{zz} \end{pmatrix}, \quad \text{Tr}(\chi\chi) = \frac{1}{2}. \quad (3.12)$$

The matrix elements can be parameterized by $\xi \in [0, 2\pi]$:

$$\begin{aligned} \chi_{xx} &= \frac{1}{\sqrt{3}} \sin\left(\xi - \frac{\pi}{6}\right), \\ \chi_{yy} &= \frac{1}{\sqrt{3}} \sin\left(\xi - \frac{5\pi}{6}\right), \\ \chi_{zz} &= \frac{1}{\sqrt{3}} \sin\left(\xi - \frac{9\pi}{6}\right). \end{aligned} \quad (3.13)$$

In the mean field approximation, all of the quantum spin nematics specified by different diagonal matrices Eq.(3.12) or different ξ have the same energy, i.e. are exactly degenerate. For instance, when $\xi = 0$ or $2\chi_{xx} = 2\chi_{yy} = -\chi_{zz} = 1/\sqrt{3}$, up to an overall $SO(3)$ rotation, all atoms are condensed in the hyperfine state $|2, 0\rangle$. This choice of χ represents a uniaxial spin nematic. When $\chi_{xx} = -\chi_{yy} = 1/2$, $\chi_{zz} = 0$ or $\xi = \frac{\pi}{2}$, the atoms are condensed in the state $\frac{1}{\sqrt{2}}(|2, 2\rangle + |2, -2\rangle)$. In the Zeeman basis, the nematic states are:

$$\psi_{m_F} = \sqrt{\frac{M}{2}} \left(\sin \xi, 0, \sqrt{2} \cos \xi, 0, \sin \xi \right) \quad (3.14)$$

It is worth pointing out that spin nematics here are time-invariant; the expectation value of the hyperfine spin operator \mathcal{F}_k in these states is zero. However, all nematics have the following nonzero quadrupole spin order (up to an $SO(3)$ rotation),

$$\begin{aligned} \mathcal{O}_{\alpha\beta} &= \langle \mathcal{F}_{k\alpha} \mathcal{F}_{k\beta} \rangle - \frac{1}{3} \delta_{\alpha\beta} \langle \mathcal{F}_k^2 \rangle, \\ \mathcal{O}_{\alpha\beta} &= 2M \sin(2\xi + \xi_\alpha) \delta_{\alpha\beta}. \end{aligned} \quad (3.15)$$

Two kinds of nematic states have higher symmetries than other nematic states, namely the uniaxial nematic states and biaxial nematic states. These states will be selected out by quantum fluctuations and will be discussed in the next two sections.

3.3 Zero-Point Quantum Fluctuations

Quantum fluctuations of mean field nematic states can be viewed as the zero-point motion of mean field collective modes. These modes can be treated as a set of decoupled oscillations with definite frequencies and wavefunctions, which are the eigen-modes of the linearized Gross-Pitaevskii equation. They have been thoroughly studied in single-component condensates in experiments. For example, various shape oscillations including breathing modes and quadrupole modes were created by modulating the trapping potentials and were measured by monitoring time evolution of density profiles[45, 44]. The propagation of sound waves created by laser pulses were also studied in a similar way[150]. The Bogoliubov quasi-particles have also been studied using Bragg spectroscopy[46], in which one can read out wavefunctions of Bogoliubov excitations from a condensate's response to optically imprinted phonons. However, these mean field modes in spinor condensates haven't been fully explored in experiments yet. In principle they can be detected and identified by the time evolution of spin populations. For example, normal modes in different branches usually have distinctive spin wavefunctions, as summarized in Tab.3.3 for spin-two nematic states.

To study zero-point quantum fluctuations, we first examine the energy spectra of collective modes. For this, we expand ψ^\dagger about the mean field $\tilde{\chi}$,

$$\hat{\psi}_{k,\alpha\beta}^\dagger = \sqrt{4M}\chi_{\alpha\beta}(\xi) + \sum_{\nu} L_{\alpha\beta}^{\nu}(\xi)\hat{\theta}_{k,\nu}^\dagger \quad (3.16)$$

where the superscript $\nu = x, y, z, t, p$ labels zero-point motions of χ along five orthogonal directions: three SO(3) spin modes (x -, y -, z -mode) for rotations about the x , y and z axes, respectively, a spin mode (t -mode) for the motion along the unit circle of ξ , and a phase mode (p -mode) describing fluctuations of the condensate's overall phase. The corresponding matrices are

$$\begin{aligned} L^x &= \begin{pmatrix} 0 & 0 & 0 \\ 0 & 0 & 1 \\ 0 & 1 & 0 \end{pmatrix}, \\ L^y &= \begin{pmatrix} 0 & 0 & 1 \\ 0 & 0 & 0 \\ 1 & 0 & 0 \end{pmatrix}, \\ L^z &= \begin{pmatrix} 0 & 1 & 0 \\ 1 & 0 & 0 \\ 0 & 0 & 0 \end{pmatrix}, \end{aligned}$$

3.3. Zero-Point Quantum Fluctuations

Table 3.3: Collective modes of nematic states specified by ξ . Distinctive spin waves functions of collective modes are listed in the Zeeman basis. v_ν is the velocity of the ν -th mode. The uniaxial nematics are specified by $\xi = 0, \pi/3, \dots$ and the biaxial nematics are specified by $\xi = \pi/6, \pi/2, \dots$.

mode(ν)	spin wavefunctions	$v_\nu^2/(4Mt_L d_L^2)$
phase(p)	$(\sin \xi, 0, \sqrt{2} \cos \xi, 0, \sin \xi)$	$a_L + c_L$
deformation(t)	$(\cos \xi, 0, -\sqrt{2} \sin \xi, 0, \cos \xi)$	$-c_L$
spin(x)	$(0, +1, 0, +1, 0)$	$4b_L \sin^2(\xi - 2\pi/3) - c_L$
spin(y)	$(0, +1, 0, -1, 0)$	$4b_L \sin^2(\xi + 2\pi/3) - c_L$
spin(z)	$(+1, 0, 0, 0, -1)$	$4b_L \sin^2 \xi - c_L$

$$\begin{aligned}
 L^t &= \frac{2}{\sqrt{3}} \begin{pmatrix} \sin(\xi + \frac{\pi}{3}) & 0 & 0 \\ 0 & \sin(\xi - \frac{\pi}{3}) & 0 \\ 0 & 0 & \sin(\xi - \frac{2\pi}{3}) \end{pmatrix}, \\
 L^p &= \frac{2}{\sqrt{3}} \begin{pmatrix} \sin(\xi - \frac{\pi}{6}) & 0 & 0 \\ 0 & \sin(\xi - \frac{5\pi}{6}) & 0 \\ 0 & 0 & \sin(\xi - \frac{9\pi}{6}) \end{pmatrix}. \quad (3.17)
 \end{aligned}$$

These matrices are mutually orthogonal, $\text{Tr}(L^\mu L^\nu) = 2\delta_{\mu\nu}$. The five modes are decoupled and the corresponding operators obey the bosonic commutation relations, $[\theta_{k,\mu}, \theta_{l,\nu}^\dagger] = \delta_{kl}\delta_{\mu\nu}$.

We expand the Hamiltonian in Eq. (3.1) using Eq. (3.16) and keep the lowest order non-vanishing terms. The result is a Hamiltonian for the fluctuations which is bilinear in $\theta_{k,\nu}^\dagger, \theta_{k,\nu}$. It can be diagonalized by a Bogoliubov transformation. The result can be expressed in terms of Bogoliubov operators, $\tilde{\theta}_{\mathbf{q},\nu}^\dagger$ and $\tilde{\theta}_{\mathbf{q},\nu}$,

$$\mathcal{H} = \sum_{\mathbf{q},\nu} \sqrt{\epsilon_{\mathbf{q}}(2m_{BN}v_\nu^2 + \epsilon_{\mathbf{q}})} \left(\tilde{\theta}_{\mathbf{q},\nu}^\dagger \tilde{\theta}_{\mathbf{q},\nu} + \frac{1}{2} \right). \quad (3.18)$$

Here $\epsilon_{\mathbf{q}} = 4t_L \sum_{\alpha} (1 - \cos q_{\alpha} d_L)$ is the kinetic energy of an atom with crystal quasi-momentum $\mathbf{q} = (q_x, q_y, q_z)$; d_L is the lattice constant. $m_{BN} = 1/4t_L d_L^2$ is the effective band mass. v_ν ($\nu = x, y, z, t, p$) is the sound velocity of the ν -mode in the small- $|\mathbf{q}|$ limit; $v_{\alpha=x,y,z}^2 = 4Mt_L d_L^2 (b_L G^{\alpha\alpha} - c_L)$, $v_t^2 = 4Mt_L d_L^2 (-c_L)$, $v_p^2 = 4Mt_L d_L^2 (a_L + c_L)$. The velocities of three spin modes depend on a $\tilde{\chi}$ -dependent 3×3 symmetric matrix $G^{\alpha\beta}$, $G^{\alpha\beta} = -(1/2)\text{Tr}([L^\alpha, L^p][L^\beta, L^p])$. More explicitly, $G^{\alpha\beta}$ is a diagonal matrix with elements: $G^{xx} = 4\sin^2(\xi - \frac{2\pi}{3})$, $G^{yy} = 4\sin^2(\xi + \frac{2\pi}{3})$, $G^{zz} = 4\sin^2 \xi$. Notice that the velocity of the phase mode v_p can be written as $\sqrt{\mu_L/m_{BN}}$,

3.3. Zero-Point Quantum Fluctuations

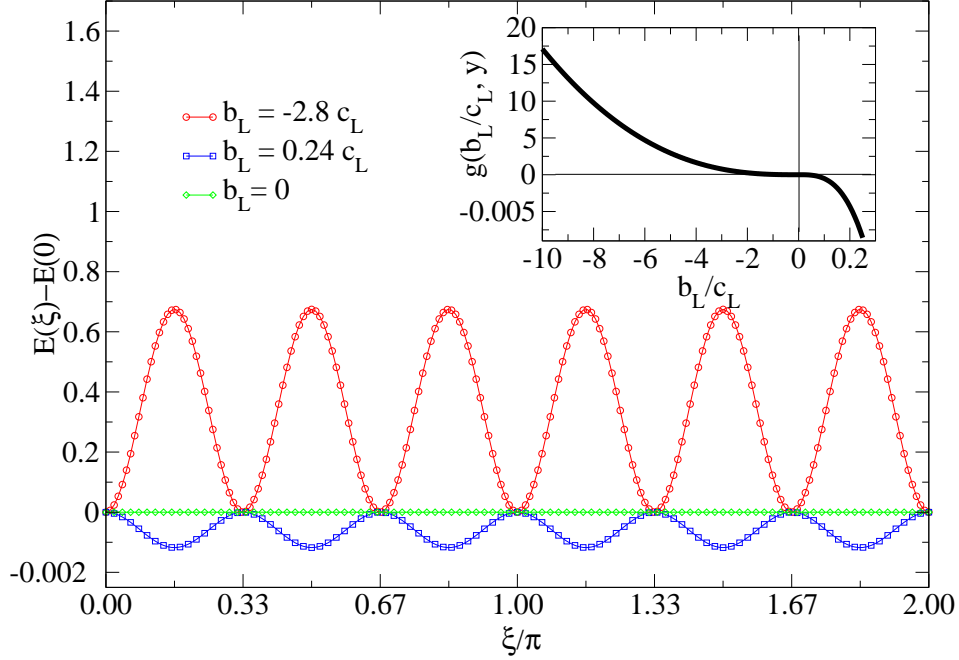


Figure 3.2: (Color online) The zero-point energy of spin nematics per lattice site as a function of ξ (in units of $|Mc_L|^{5/2}/t_L^{3/2}$, $c_L < 0$). Inset is $g(x, y)$, the amplitude of $E(\xi = \frac{\pi}{6}) - E(0)$ as a function of $x(= b_L/c_L)$. $y(= |c_L|/t_L)$ has been set to be 8×10^{-3} . A quantum first order phase transition occurs at $b_L = 0$ as a result of zero-point quantum fluctuations. For a positive b_L , the energy minima correspond to uniaxial spin nematics while the maxima to biaxial spin nematics with Dih_4 symmetries.

only depending on the band mass m_{BN} and the chemical potential μ_L ; it is independent of ξ .

Unlike the mean field energy E_{MF} that is independent of ξ , the zero-point energy of spin nematics per lattice site E is ξ -dependent (α summed over x, y, z),

$$E(\xi) = \frac{1}{2N_T} \sum_{\mathbf{q}, \alpha} \sqrt{\epsilon_{\mathbf{q}}(2m_{BN}v_{\alpha}^2(\xi) + \epsilon_{\mathbf{q}})}. \quad (3.19)$$

Here N_T is the number of lattice sites. The main contribution to the ξ -dependence of energy is from fluctuations of wave vector $|\mathbf{q}| \sim m_{BN}v_{\alpha}(\xi)$; for condensates, this characteristic momentum is much smaller than \hbar/d_L .

3.4. Uniaxial and Biaxial Spin Nematic States

The ξ -dependent energy is proportional to $\sum_{\alpha} v_{\alpha}^5 / (d_L^5 t_L^4)$; the amplitude of it can be expressed as $|M c_L|^{5/2} / t_L^{3/2} g(b_L/c_L, |c_L|/t_L)$, where $g(x, y)$ is a dimensionless function that is studied numerically. In Fig. 3.2, we plot the energy as a function of ξ . We find that there are two distinct phases when the parameters occur in the region $c_L < 0$ and $b_L > c_L/4$. They are separated by $b_L = 0$ line. When b_L is positive, $\xi = 0, \pi/3, 2\pi/3, \dots$ are ground states. These are uniaxial nematic states which are rotationally invariant along an easy axis (see Fig. (3.1 a)). When b_L is negative, the points of $\xi = \pi/6, \pi/2, 5\pi/6, \dots$ are the stable ground states while the uniaxial nematics are unstable.

The energy as a function of ξ has following symmetries

$$E(\xi) = E(-\xi), \quad (3.20)$$

$$E(\xi) = E\left(\frac{\pi}{3} + \xi\right). \quad (3.21)$$

These are a result of the rotation and gauge invariance of the energy function. They are found by examining the mean field solutions in Eq.(3.11),(3.13). A rotation \mathcal{R} of 120° around the $x = y = z$ line effectively transforms a solution at ξ to $\xi + \pi/3$, or $\mathcal{R}^T \chi(\xi) \mathcal{R} = -\chi(\xi + \frac{\pi}{3})$. And because the energy is invariant under $SO(3)$ rotations and is an even function of χ , one finds that $E(\xi) = E(\xi + \pi/3)$. In addition, a rotation of 180° around the $x + y = 0$ line in the xy -plane transforms $\chi(\xi)$ to $\chi(-\xi)$, i.e. $\mathcal{R}^T \chi(\xi) \mathcal{R} = \chi(-\xi)$; so similarly one finds that $E(\xi) = E(-\xi)$. These symmetries only depend on rotational and gauge invariance and are exact. So the energy is an even and periodic function of ξ , with the period equal to $\pi/3$. For an analytic function with these symmetries, $\xi = 0, \pi/6$ and $\pi/3$ are always extrema. Our calculations of the zero-point energy are consistent with this. The above observation also indicates that up to an $SO(3)$ rotation and a phase factor, states at ξ and at $\xi + \pi/3$ are equivalent.

3.4 Uniaxial and Biaxial Spin Nematic States

We now examine the topology of the manifold of fluctuation-induced spin nematics. Without loss of generality, we first consider the uniaxial nematic state at $\xi = 0$, i.e., $\chi_{xx} = \chi_{yy} = -1/2\sqrt{3}$ and $\chi_{zz} = 1/\sqrt{3}$; in this case, the nematic easy axis specified by a unit vector \mathbf{e} is pointing along the z -direction (See Fig. 3.1 (a)). Such a uniaxial state is invariant under an arbitrary rotation around the nematic axis \mathbf{e} ; it is further invariant under an inversion of the nematic axis $\mathbf{e} \rightarrow -\mathbf{e}$ which is evident in the plot for the

wavefunction. The vacuum manifold for the uniaxial nematic is therefore simply $\frac{S^2}{Z_2} \otimes S^1$; here S^2/Z_2 is where the nematic director lives and S^1 is the unit circle of condensate phase variable. Unlike in uniaxial spin nematics of $F = 1$ atoms [123], here the spin orientation and condensate phase are not entangled.

For the biaxial nematic state at $\xi = \pi/2$, $\chi_{xx} = -\chi_{yy} = 1/2$ and $\chi_{zz} = 0$. The state is invariant under the eight element *dihedral*-four group Dih_4 . The seven rotations that leave the state invariant (up to a phase shift) are 90^0 , 180^0 and 270^0 rotations about the z -axis, 180^0 rotations about the x - and y -axes and about the $x \pm y = 0$ lines in the xy -plane. Four of these rotations, the 90^0 , 270^0 rotations around z -axis, and 180^0 rotation around $x \pm y = 0$ lines must be accompanied by a shift of the phase of the condensate by π . The manifold therefore is $[SO(3) \times S^1]/Dih_4$, where the Dihedral elements in the denominator contain the rotations mentioned plus the π -phase shifts. These nematics contain half-vortices.

On the other hand, a generic biaxial spin nematic (with no accidental symmetries) is only invariant under a rotation of 180^0 around x -, or y - or z -axis and the invariant subgroup is the Klein-four or dihedral-two group; it has lower symmetries than either of the spin nematics selected by zero-point quantum fluctuations.

3.5 Discussion and Conclusion

The perturbative calculation carried out here is valid when fluctuations of the order parameter χ are small. Here we estimate the fluctuations along each of the five directions $\nu = x, y, z, t, p$. Using Eq. 3.16, we evaluate the amplitude of local fluctuations in an orthogonal mode, $A_1(\nu) = \langle 0 | \theta_{k,\nu}^\dagger \theta_{k,\nu} | 0 \rangle$. Taking into account the expression for v_ν , we have the following estimate for the relative amplitude of fluctuations,

$$\frac{A_1(\nu)}{M} \sim M^{1/2} \left(\frac{\tilde{a}_\nu}{\tilde{a}_p} \frac{a_L + c_L}{t_L} \right)^{3/2}. \quad (3.22)$$

\tilde{a}_ν is the effective scattering length of each mode which is a linear combination of scattering lengths in $F = 0, 2, 4$ channels:

$$\tilde{a}_\alpha = \frac{2 - G^{\alpha\alpha}}{7} (a_2 - a_4) - \frac{1}{5} (a_0 - a_4), \quad (3.23)$$

$$\tilde{a}_t = \frac{2}{7} (a_2 - a_4) - \frac{1}{5} (a_0 - a_4), \quad (3.24)$$

$$\tilde{a}_p = \frac{1}{7} (2a_2 + 5a_4) + \frac{1}{5} (a_0 - a_4). \quad (3.25)$$

3.5. Discussion and Conclusion

For ^{87}Rb atoms in optical lattices, $\tilde{a}_\alpha/\tilde{a}_p \sim 10^{-2}$, $a_L \sim 50nk$ and when $t_L \sim 300nk$, the relative amplitude of fluctuations in x -, y -, z -, or t -mode is typically less than one percent (see next chapter (Chap.4) for numerical estimations of in spin-two ^{87}Rb).

One of experimental signatures of quantum fluctuations is number fluctuations in spin populations. The microscopic origin of spin-population fluctuation is the two-body spin-changing scattering processes. For example atoms in the uniaxial nematic condensate ($|2, 0\rangle$) are possible to be scattered into other spins via these channels $|2, 0\rangle + |2, 0\rangle \rightleftharpoons |2, +2\rangle + |2, -2\rangle$ and $|2, 0\rangle + |2, 0\rangle \rightleftharpoons |2, +1\rangle + |2, -1\rangle$. The relative amplitude of the spin-population fluctuations is directly related to the expression in Eq.3.22.

In this chapter, we have found that zero-point quantum fluctuations lift a continuous degeneracy in spin nematics. Only uniaxial spin nematics or biaxial nematics with dihedral-four symmetries are selected as the true ground states. For Rb^{87} atoms in the hyperfine spin-two manifold, b_L is between $-3c_L$ and $-10c_L$. According to the above analysis, the ground state should be a uniaxial spin nematic. The fluctuation-induced energy landscape can be experimentally mapped out by investigating the *macroscopic quantum dynamics* of condensates prepared in certain initial states. A condensate of rubidium atoms initially prepared at state $\frac{1}{\sqrt{2}}(|2, 2\rangle + |2, -2\rangle)$ (corresponding to $\xi = \pi/2$ point), because of the fluctuation-induced potential shown in Fig.3.2, could evolve towards a condensate with atoms at state $\frac{1}{2}|2, 0\rangle + \frac{\sqrt{3}}{2\sqrt{2}}(|2, 2\rangle + |2, -2\rangle)$ (corresponding to $\xi = \pi/3$ point). This leads to a temporal oscillation of the population of atoms at state $|2, 0\rangle$, which is the main topic of the following chapter.

Chapter 4

Quantum Fluctuation Controlled Coherent Spin Dynamics in $F=2$ ^{87}Rb Condensates

4.1 Introduction

Temporal evolution of a macroscopic condensate of ultra-cold atoms is usually driven by mean field potentials, either due to scattering between atoms or due to coupling to external fields; and coherent quantum dynamics of this type have been observed in various cold atom experiments. In this chapter, we report results of studies of a class of quantum spin dynamics which are purely driven by zero-point quantum fluctuations of spin collective coordinates. Unlike the usual mean-field coherent dynamics, quantum fluctuation-controlled spin dynamics or *QFCSD* studied here are very sensitive to variation of quantum fluctuations and the corresponding driving potentials induced by zero-point motions can be tuned by four to five orders of magnitude using optical lattices. These dynamics have unique dependence on optical lattice potential depths and quadratic Zeeman fields. We also find that thermal fluctuations generally can further enhance the induced potentials although the enhancement in deep optical lattices is much less substantial than in traps or shallow lattices. *QFCSD* can be potentially used to calibrate quantum fluctuations and investigate correlated fluctuations and various universal scaling properties near quantum critical points.

Spin correlated macroscopic quantum dynamics have also been a focus of many cold atom experiments carried out recently. Spin ordering and spin-relaxation collisions were first investigated in condensates of sodium atoms by Inouye *et al.* and Miesner *et al.* from Ketterle's group at MIT[38, 151]. Coherent spin dynamics driven by various mean field interactions or external fields were later demonstrated in condensates of hyperfine spin-two rubid-

ium atoms [39], and hyperfine spin-one rubidium atoms[87, 92]. Ordering in spinor gases is usually induced by hyperfine spin dependent two-body scattering[107, 108]. Coherent spin dynamics observed in experiments are related to the coherent quantum dynamics explored in solid state superconductors, and earlier experiments on ultra cold gases of atoms[152, 54]. They are explicit manifestations of fascinating macroscopic quantum states and can be potentially applied towards constructing high precision interferometers. Remarkably, coherent dynamics also provide a unique direct measure of interaction energies or scattering lengths as emphasized before [152, 39, 87].

Quantum fluctuation-controlled spin dynamics or *QFCSD* we are going to study in this chapter on the other hand are a direct measure of quantum fluctuations; they can be potentially used to calibrate quantum fluctuations and investigate correlated fluctuations near quantum critical points or universal scaling properties. Furthermore, *QFCSD* of cold atoms can be designed to simulate many other quantum-fluctuation-induced phenomena such as Coleman-Weinberg mechanism of spontaneous symmetry breaking[11], and order due to disorder in antiferromagnets[13, 14].

The system we are examining to understand *QFCSD* is a condensate of rubidium atoms (^{87}Rb) in hyperfine spin-two ($F = 2$) states. The two-body scattering lengths between rubidium atoms have been estimated using both photoassociation data[153, 28, 154, 143], and elastic scattering data near Feshbach resonances[29, 142]. Most recently, Rabi oscillations between different two-spin states have also been used to measure spin dependent interactions[96].

However it is quite challenging to probe *QFCSD* in traps without optical lattices, if not impossible. For dilute gases in the absence of optical lattices, the effective driving potential induced by quantum fluctuations is about 10^{-5}pK per particle (see section III for more discussions) because the relative amplitude of fluctuations is very small. The corresponding dynamics driven by such a small potential are only visible at a time scale of a few thousand seconds, too slow to be observed in current cold atom experiments. In addition, a tiny external magnetic field of strength 1mG can result in a quadratic Zeeman coupling of order of $6 \times 10^{-3}\text{pk}$ for rubidium atoms which is three orders of magnitude larger than the induced potential in dilute gases. In most experiments because of noises in lasers, the effective quadratic Zeeman coupling can be controlled only up to an uncertainty that is equivalent to a magnetic field of an order of 1mG . This further complicates future experimental studies of *QFCSD*. To resolve these difficulties, we propose to enhance the effect of *QFCSD* using optical lattices. To vary the amplitude of quantum fluctuations and optimize the effect of fluctua-

tions, we study *QFCSD* in optical lattices where the optical potential depth V is a convenient tunable parameter[70, 71, 155, 156, 157].

The rest of the chapter is organized as follows. In Sec.4.2 and Sec.4.3, we introduce a lattice Hamiltonian to study dynamics of ^{87}Rb atoms in optical lattices and discuss the range of parameters we have used to investigate this phenomenon. In Sec.4.4, we briefly discuss the structure of spin nematic states. In Sec.4.5, we derive an effective Hamiltonian for *QFCSD* by introducing low energy collective coordinates and their conjugate momentum. In Sec.4.6 and Sec.4.7, we present our main numerical results on quantum-fluctuation induced potentials, frequencies of coherent dynamics, and how potentials and frequencies depend on optical lattice potential depth. We also study the dynamical stabilities of coherent oscillations when a quadratic Zeeman coupling is present. In Sec.4.8, we discuss effects of thermal fluctuations and analyze the potential-depth dependence of thermal enhancement of induced driving potential. In Sec.4.9, we further investigate effects of spin exchange losses and propose how to observe quantum-fluctuation-controlled spin dynamics within a relatively short life time of $F = 2$ rubidium atoms. In Sec.4.10, we estimate the condensation fraction or depletion fraction to verify the validity of our perturbative calculations. In the last section, we conclude our studies of *QFCSD*.

4.2 Microscopic Hamiltonian for $F = 2$ ^{87}Rb in Optical Lattices

We are considering the following Hamiltonian for $F = 2$ atoms in optical lattices:

$$\begin{aligned} \mathcal{H} = & \sum_k \left(\frac{a_L}{2} (\hat{\rho}_k^2 - \hat{\rho}_k) + \frac{b_L}{2} (\hat{\mathcal{F}}_k^2 - 6\hat{\rho}_k) + 5c_L \mathcal{D}_k^\dagger \mathcal{D}_k \right) \\ & - t_L \sum_{\langle kl \rangle} \left(\psi_{k,\alpha\beta}^\dagger \psi_{l,\beta\alpha} + \text{h.c.} \right) - \mu \sum_k \hat{\rho}_k + q_B \sum_k \mathcal{Q}_{k,zz}. \quad (4.1) \end{aligned}$$

Here k is the lattice site index and $\langle kl \rangle$ are the nearest neighbor sites, μ is the chemical potential and t_L is the one-particle hopping amplitude, q_B is the quadratic Zeeman coupling constant. a_L , b_L and c_L are three interaction constant which we will discuss later.

We have employed the traceless symmetric matrix operator ψ^\dagger that was introduced previously in Sec.2.4.2 of Chap.2. Components $\psi_{\alpha\beta}^\dagger$, $\alpha, \beta = x, y, z$ are linear superpositions of five spin-two creation operators, $\psi_{m_F}^\dagger$,

4.3. Range of Interaction Parameters for the Lattice Hamiltonian

$m_F = 0, \pm 1, \pm 2$. It is advantageous to use this tensor representation if one is interested in rotational symmetries of condensate wavefunctions, or construction of rotationally invariant operators. We use it to analyze collective spin modes that correspond to small rotations around various axes. The number operator $\hat{\rho}_k$, the dimer or singlet pair creation operator \mathcal{D}_k^\dagger , the total spin operator $\hat{F}_{k,\alpha}$ are defined as $\hat{\rho}_k = \frac{1}{2}\text{Tr}(\psi_k^\dagger \psi_k)$, $\mathcal{D}_k^\dagger = \frac{1}{\sqrt{40}}\text{Tr}(\psi_k^\dagger \psi_k^\dagger)$, $\hat{F}_{k,\alpha} = -i\epsilon_{\alpha\beta\gamma}\psi_{k,\beta\eta}^\dagger \psi_{k,\eta\gamma}$ (See Chap.2 for details). The quadratic Zeeman operator $\mathcal{Q}_{k,zz}$ is defined as

$$\begin{aligned}\mathcal{Q}_{k,zz} &= \text{Tr}(\psi_k^\dagger Q \psi_k) \\ Q &= \begin{pmatrix} 0 & 0 & 0 \\ 0 & 0 & 0 \\ 0 & 0 & 1 \end{pmatrix}.\end{aligned}\quad (4.2)$$

4.3 Range of Interaction Parameters for the Lattice Hamiltonian

Spin correlations between hyperfine spin-two rubidium atoms are determined by three two-body s-wave scattering lengths a_F , $F = 0, 2, 4$. In optical lattices, local spin-dependent interactions contain two contributions as shown in Eq.(4.1); one is, $b_L \mathcal{F}_k^2/2$, the energy of having total hyperfine spin \mathcal{F}_k at site k , and the other is the energy of creating spin singlet pairs (*dimers*), $5c_L \mathcal{D}_k^\dagger \mathcal{D}_k$ where \mathcal{D}_k is the dimer creation operator. The usual contact interaction at site k is of the form $a_L(\rho_k^2 - \rho_k)/2$, where ρ_k is the number of atoms. Three effective coupling constants a_L, b_L, c_L which characterize various interactions are functions of two-body scattering lengths a_F , $F = 0, 2, 4$ and on-site orbitals $\psi_0(\mathbf{r})$,

$$a_L(b_L, c_L) = a(b, c) \frac{4\pi\hbar^2}{m} \int d\mathbf{r} (\psi_0^*(\mathbf{r})\psi_0(\mathbf{r}))^2. \quad (4.3)$$

Here

$$\begin{aligned}a &= (4a_2 + 3a_4)/7, \\ b &= (a_4 - a_2)/7, \\ c &= (7a_0 - 10a_2 + 3a_4)/35\end{aligned}\quad (4.4)$$

are three effective scattering lengths; ψ_0 is the localized Wannier function obtained by solving the Schrodinger equation for an atom in periodical potentials. The band structures and Wannier functions are calculated through

4.3. Range of Interaction Parameters for the Lattice Hamiltonian

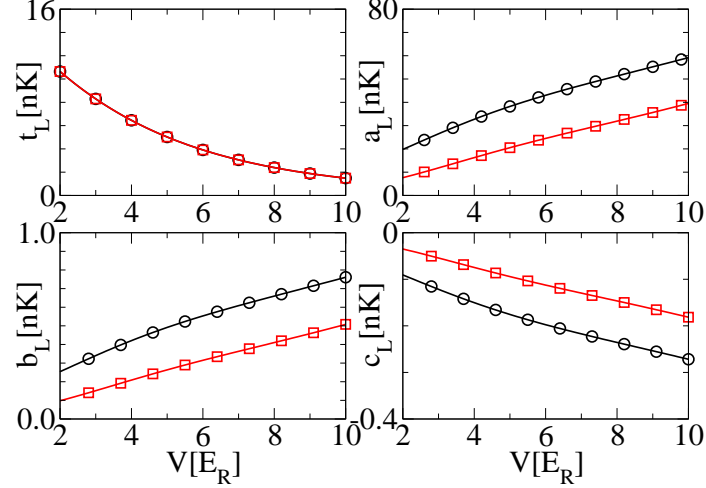


Figure 4.1: (Color online) Coupling parameters a_L , b_L , c_L and hopping integral t_L (all in units of nK) as a function of optical potential depth V (in units of recoil energy E_R) in 3D (black circles) and 2D (red squares) optical lattices. $E_R = 3.18kHz$ for $\lambda = 850nm$ lasers.

standard methods outlined in the Appendix. a_L, b_L, c_L can then be calculated using the estimates of scattering lengths obtained in Ref.[142]. The range of these parameters for rubidium atoms in optical lattices is plotted in Fig.4.1.

The range of lattice potential depth is chosen to be from zero up to ten recoil energy or $10E_R$. ($E_R = h^2/2m\lambda^2$, where λ is the wavelength of lasers.) Below $2E_R$, quantum fluctuations turn out to be too weak to induce substantial potential and dynamics. And also the above Hamiltonian is not valid for shallow optical lattices as a large overlapping of Wannier functions will lead complications such as interaction term between adjacent sites. For these reason, we only show numerical results for V larger than $2E_R$ but less than $10E_R$. Within this range, we find that quantum depletion is usually small, less than twenty percent and our lowest order calculation should suffice. Although quantum fluctuations can be further enhanced above $10E_R$ and a superfluid-Mott phase transition should take place at $13E_R$ [70, 71], close to a critical region we however expect a perturbative calculation like the one carried out in this chapter becomes invalid. The range of atom number density here, or the number of atoms per lattice

4.3. Range of Interaction Parameters for the Lattice Hamiltonian

site M is from zero to three. Most of data are shown for typical values $M = 1.0, 2.0, 3.0$.

The single band Hamiltonian used here is valid when all interaction constants above are much smaller than the energy spacing between centers of two lowest bands. Note that a gap between the first band and higher bands is not necessarily required for the single band Bose model as for the fermionic models. This is because in the condensate phase when depletion is small, most of the bosons are staying at the bottom of the first band that very few atoms are occupying higher levels and can see the gap. On the contrary, properties of fermions in the optical lattice are sensitive to filling factors due to pauli exclusion principles that the existence or absence of a band gap can make a crucial difference.

For $F = 2$ rubidium atoms, the quadratic Zeeman coupling q_B is related to a uniform external magnetic field B via $q_B = 3(\mu_B B/2)^2/\Delta$, $\Delta = 6.8\text{GHz}$ (see Appendix). Here μ_B is the Bohr magneton and Δ is the hyperfine splitting. For the purpose of studying *QFCSD*, we set the range of B to be $70\text{mG} > B > 1\text{mG}$ where effects of quantum fluctuations are most visible; beyond 70mG the dynamics are mainly driven by the mean field quadratic coupling q_B (see section VI for more discussions). The corresponding range for the quadratic Zeeman coupling is then from 10^{-2}pK to 100pK .

Here we assume that the optical lattice potential does not dependent on hyperfine spin levels. Practically, the optical dipole potential has a weak hyperfine spin dependence for alkali atoms in many cases because dipole transitions depend on which hyperfine Zeeman levels are involved. For ^{87}Rb , the hyperfine spin dependent dipole interaction up to the leading order of m_F is given by [158, 159, 160]

$$V(r) = V_0 \left[1 + g_F m_F \frac{\Delta_{1/2} - \Delta_{3/2}}{\Delta_{1/2} + 2\Delta_{3/2}} \sum_{q=-1,0,1} q \frac{I_q(r)}{I(r)} \right] \quad (4.5)$$

Here m_F is the Zeeman state (with gyromagnetic ratio g_F) of the atom; $\Delta_{3/2}$ ($\Delta_{1/2}$) is the detuning relative to the $S \rightarrow P_{3/2}$ ($S \rightarrow P_{1/2}$) transition; q refers to the three possible polarizations of light. I_q is the intensity of laser beams with polarization q and I is the total intensity. The small parameter controlling the strength of hyperfine spin dependent term is $\frac{\Delta_{1/2} - \Delta_{3/2}}{\Delta_{1/2} + 2\Delta_{3/2}}$ which is about 0.07 for ^{87}Rb loaded in optical lattices operating at a wavelength of 850nm. By choosing a suitable polarization of the laser beams[160], one can make the first order term vanish, resulting in an even weaker hyperfine dependence appearing in the quadratic term of m_F . In this case,

the leading contribution is from the residual quadratic term of m_F , which is estimated to be 10^{-1} at maximum of the spin-dependent two-body interaction. More importantly, this residual quadratic term can be absorbed into the quadratic Zeeman term in Eq.4.1 by introducing a small shift in the definition of q_B given in the previous paragraph. For these two reasons, we will neglect the effects of spin dependent optical potential.

4.4 Mean Field Nematic States and Coherent Dynamics

The coherent spin dynamics of a *uniform* condensate can be described by the evolution of a condensate wavefunction $\tilde{\chi}$, i.e. the expectation value of matrix operator ψ^\dagger . The corresponding equation of $\tilde{\chi}$ is

$$\begin{aligned} \frac{i}{2} \frac{\partial \tilde{\chi}}{\partial t} &= \frac{\partial H_{sc}}{\partial \tilde{\chi}^*} + \frac{\partial H_Q}{\partial \tilde{\chi}^*} + \frac{\partial H_{qf}}{\partial \tilde{\chi}^*}; \\ \frac{\partial H_{sc}}{\partial \tilde{\chi}^*} &= \frac{a_L}{4} \tilde{\chi} \text{Tr}(\tilde{\chi}^* \tilde{\chi}) + \frac{c_L}{4} \tilde{\chi}^* \text{Tr}(\tilde{\chi} \tilde{\chi}) \\ &\quad + \frac{b_L}{2} [\tilde{\chi}, [\tilde{\chi}^*, \tilde{\chi}]] - (zt_L + \mu/2) \tilde{\chi}, \\ \frac{\partial H_Q}{\partial \tilde{\chi}^*} &= q_B Q \tilde{\chi}. \end{aligned} \tag{4.6}$$

Here H_{sc} is the mean field (semiclassical) Hamiltonian (of matrix $\tilde{\chi}$, $\tilde{\chi}$) obtained previously[134, 125, 124], H_Q is the quadratic Zeeman coupling term with q_B being the coupling strength. H_{sc} and H_Q (per lattice site) are given by:

$$\begin{aligned} H_{sc} &= \frac{a_L}{8} \text{Tr}(\tilde{\chi}^* \tilde{\chi}) \text{Tr}(\tilde{\chi}^* \tilde{\chi}) + \frac{c_L}{8} \text{Tr}(\tilde{\chi}^* \tilde{\chi}^*) \text{Tr}(\tilde{\chi} \tilde{\chi}) \\ &\quad + \frac{b_L}{4} \text{Tr}[\tilde{\chi}^*, \tilde{\chi}]^2 - (zt_L + \mu/2) \text{Tr}(\tilde{\chi}^* \tilde{\chi}); \end{aligned} \tag{4.7}$$

$$H_Q = q_B \text{Tr}(\tilde{\chi}^* Q \tilde{\chi}). \tag{4.8}$$

z is the coordination number of optical lattices. For a field along the z -direction, matrix Q is defined as $Q_{\alpha\beta} = \delta_{\alpha z} \delta_{\beta z}$. And H_{qf} is the quantum-fluctuation-induced Hamiltonian discussed below.

For rubidium atoms, scattering lengths estimated in Ref.[28, 154, 143] lead to $b_L = -10c_L$ while results in Ref.[29, 142] yield $b_L = -2.8c_L$. Both calculations show that interaction parameters satisfy $c_L < 0$ and $4b_L > c_L$. As pointed out in the previous chapter, in this parameter region without

quadratic Zeeman coupling, ground states are spin nematics characterized by real and symmetric tensor wavefunctions $\tilde{\chi}$ (up to an overall phase). Any condensate that is initially prepared in this submanifold has no mean field dynamics because the potential gradient $\partial H_{sc}/\partial \tilde{\chi}^*$ vanishes.

4.5 Effective Hamiltonian for QFCSD

To investigate the kinetic energy and quantum fluctuation-induced potential energy for dynamics of a condensate initially prepared in this submanifold, we expand tensor $\psi_{\alpha\beta}^\dagger$ about a reference condensate wavefunction $\chi(\xi)$ in terms of five collective coordinates X_ν introduced above and their conjugate operators \hat{P}_ν . We furthermore separate the macroscopic dynamics of condensates ($\mathbf{q} = 0$ -mode) from the microscopic zero-point quantum fluctuations ($\mathbf{q} \neq 0$ mode). And we restrict ourselves to the dynamics of a condensate in a linear regime.

4.5.1 Nematic Manifold

To highlight the structure of degenerate ground states, we consider an arbitrary condensate amplitude $\tilde{\chi}$ in the spin nematic submanifold. It can be parameterized using an $SO(3)$ rotation, \mathcal{R} and a $U(1)$ phase shift ϕ , and a real diagonal traceless matrix χ ; i.e.,

$$\begin{aligned}\tilde{\chi}(X_x, X_y, X_z, \xi, \phi) &= \sqrt{4M} e^{i\phi} \mathcal{R}^T \chi(\xi) \mathcal{R}, \\ \mathcal{R}(X_x, X_y, X_z) &= \exp(T^x X_x + T^y X_y + T^z X_z)\end{aligned}\quad (4.9)$$

where M is the number density or average number of atoms per lattice site. \mathcal{R} is an $SO(3)$ rotation matrix defined by three spin angles X_α , $\alpha = x, y, z$, and antisymmetric generators $T_{\beta\gamma}^\alpha = -\epsilon_{\alpha\beta\gamma}$. $\chi(\xi)$, $\xi \in [0, 2\pi]$, are normalized real diagonal traceless matrices that form a family of solutions specified by a single parameter ξ [124];

$$\chi_{\alpha\alpha} = \frac{\sin(\xi - \xi_\alpha)}{\sqrt{3}}, \quad (4.10)$$

and $\xi_x = \pi/6$, $\xi_y = 5\pi/6$ and $\xi_z = 3\pi/2$. Nematics with different ξ exhibit different spin configurations. Following the definition of tensor operator in Eq.(2.34), one can easily show that these solutions represent condensates of spin-two atoms specified by five-component wavefunctions $\psi^T = (\psi_2, \psi_1, \psi_0, \psi_{-1}, \psi_{-2})$ and

$$\psi^T = \sqrt{M} \left(\frac{\sin \xi}{\sqrt{2}}, 0, \cos \xi, 0, \frac{\sin \xi}{\sqrt{2}} \right). \quad (4.11)$$

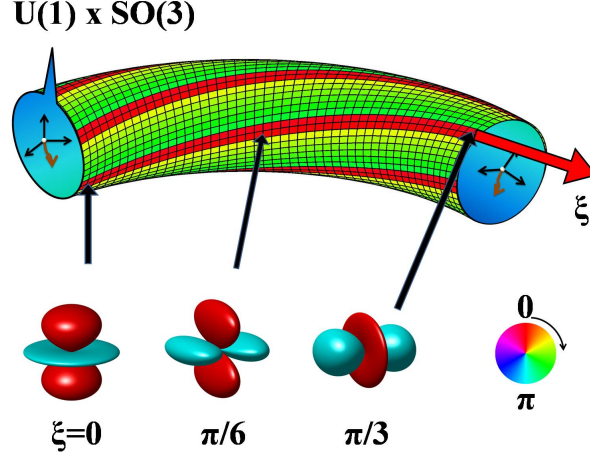


Figure 4.2: (Color online) An artistic view of the five-dimension manifold of spin nematics. Three $SO(3)$ rotation degrees and $U(1)$ -phase degree are represented by a cross section at a given spin deformation angle ξ . We have also plotted the nematic wavefunctions $\psi_S(\theta, \phi) = \sum_{\alpha\beta} \chi_{\alpha\beta} n_\alpha n_\beta$ as a function θ, ϕ in a spherical coordinate. n_α , is the α th component of a unit vector $\mathbf{n}(\theta, \phi)$ and colors indicate phases of wavefunctions.

So in a more conventional representation, these states labeled by value ξ correspond to condensates where all atoms occupy a particular spin-two state,

$$|\xi\rangle = \cos \xi |2, 0\rangle + \frac{\sin \xi}{\sqrt{2}} (|2, 2\rangle + |2, -2\rangle). \quad (4.12)$$

Therefore, the nematic submanifold is effectively a five-dimension space that is characterized by five collective coordinates X_ν , $\nu = x, y, z, \xi, p$: three spin rotational angles X_α ($\alpha = x, y, z$), one spin deformation ξ -angle X_ξ (or ξ) specifying spin configurations and one phase angle $X_p (= \phi)$. Furthermore, it is easy to verify that up to an $SO(3)$ rotation and a phase factor, states at ξ and at $\xi + \pi/3$ are equivalent and the fundamental period of this characterization is $\pi/3$. When the system is rotationally invariant (i.e. no external fields), we also find that $E(\xi) = E(\xi + \pi/3)$ and $E(\xi) = E(-\xi)$ (See previous discussion in Chap.3). $E(\xi)$ is the energy of a state defined by ξ .

4.5.2 Collective Coordinates and Conjugate Momentum

To study QFCSD, we expand ψ^\dagger about a reference condensate χ ,

$$\begin{aligned} \hat{\psi}_{k,\alpha\beta}^\dagger &= \sqrt{4M}\chi_{\alpha\beta}(\xi) \\ &+ \frac{1}{\sqrt{N_T}} \sum_\nu L_{\alpha\beta}^\nu (\hat{\theta}_\nu^\dagger(0) + \sum_{\mathbf{q}\neq 0} e^{i\mathbf{q}\cdot\mathbf{r}_k} \hat{\theta}_\nu^\dagger(\mathbf{q})). \end{aligned} \quad (4.13)$$

Here N_T is the number of lattice sites and M is the number of atoms per site. The superscripts (or subscripts) $\nu = x, y, z, \xi, p$ specify condensate motion along the five orthogonal directions of the submanifold. $\hat{\theta}_\nu(\mathbf{q})$ ($\hat{\theta}_\nu^\dagger(\mathbf{q})$) are annihilation (creation) operators of the collective excitations of mode ν with lattice crystal momentum \mathbf{q} . One can further include bilinear terms in the expansion. The motion along these five orthogonal directions is studied by introducing five mutually orthogonal matrices L^ν , i.e. $\text{Tr}(L^\mu L^\nu) = 2\delta_{\mu\nu}$. Explicit forms of these orthogonal matrices were introduced in the previous chapter.

We are restricting ourselves to the dynamics of a condensate in a linear regime. By expanding the original Hamiltonian in Eq.(4.1) using the decomposition introduced in Eq.(4.13), we obtain an effective Hamiltonian that is bilinear in terms of θ^\dagger and θ . It is convenient to introduce five collective Hermitian operators \hat{X}_ν defined in terms of $\theta_\nu^\dagger(0)$, $\theta_\nu(0)$ for $\mathbf{q} = 0$ modes,

$$\begin{aligned} \hat{X}_p &= \frac{\theta_p^\dagger - \theta_p}{2i\sqrt{N}}, \\ \hat{X}_t &= \frac{\theta_t^\dagger + \theta_t}{2\sqrt{N}}, \\ \hat{X}_x &= \frac{\theta_x^\dagger + \theta_x}{4\sqrt{N}(\chi_{yy} - \chi_{zz})}, \\ \hat{X}_y &= \frac{\theta_y^\dagger + \theta_y}{4\sqrt{N}(\chi_{zz} - \chi_{xx})}, \\ \hat{X}_z &= \frac{\theta_z^\dagger + \theta_z}{4\sqrt{N}(\chi_{xx} - \chi_{yy})} \end{aligned} \quad (4.14)$$

where $N = N_T M$ is the total number of atoms in a lattice with N_T sites. By comparing Eq.(4.13) and the expression for $\tilde{\chi}$ in terms of five spin coordinates X_ν (see discussions before Eq.(4.10)), one identifies the semiclassical collective coordinates X_ν as the expectation value of harmonic oscillator operators \hat{X}_ν . In the following, we do not distinguish between \hat{X}_ν and X_ν .

4.5. Effective Hamiltonian for QFCSD

The conjugate momentum operators \hat{P}_ν can be introduced accordingly so that the usual commuting relations are obeyed, i.e $[\hat{X}_\nu, \hat{P}_\mu] = i\delta_{\nu\mu}$.

$$\begin{aligned}
\hat{P}_p &= \sqrt{N} \left(\hat{\theta}_p^\dagger + \hat{\theta}_p \right), \\
\hat{P}_t &= -i\sqrt{N} \left(\hat{\theta}_t - \hat{\theta}_t^\dagger \right), \\
\hat{P}_x &= -2i\sqrt{N} (\chi_{yy} - \chi_{zz}) \left(\hat{\theta}_x - \hat{\theta}_x^\dagger \right), \\
\hat{P}_y &= -2i\sqrt{N} (\chi_{zz} - \chi_{xx}) \left(\hat{\theta}_y - \hat{\theta}_y^\dagger \right), \\
\hat{P}_z &= -2i\sqrt{N} (\chi_{xx} - \chi_{yy}) \left(\hat{\theta}_z - \hat{\theta}_z^\dagger \right).
\end{aligned} \tag{4.15}$$

4.5.3 Spectra of Collective Modes

Five modes of zero-point motions (microscopic) around $\chi(\xi)$ can also be labeled by the same set of indices. For collective excitations of mode- ν with lattice momentum $\mathbf{q} (\neq 0)$, creation operators are $\theta_\nu^\dagger(\mathbf{q})$. These operators obey the bosonic commutation relations, $[\theta_{k,\mu}, \theta_{l,\nu}^\dagger] = \delta_{kl}\delta_{\mu\nu}$. Note that only the properties of three rotation modes and deformation mode (ξ -mode) depend on the value of ξ . The collective mode dispersion around $\xi = 0$ or $\xi = \pi/2$ has a very simple form,

$$E_{\nu,\mathbf{q}}(\xi, X_\xi, q_B) = \sqrt{\epsilon_{\nu,\mathbf{q}}[2m_{BN}v_\nu^2(\xi + X_\xi) + \epsilon_{\nu,\mathbf{q}}]}. \tag{4.16}$$

And in the expression for $E_{\nu,\mathbf{q}}$,

$$\epsilon_{\nu,\mathbf{q}} = 4t_L \sum_{\alpha} (1 - \cos q_\alpha d_L) + \kappa_\nu q_B \tag{4.17}$$

is the energy of an atom with crystal quasi-momentum $\mathbf{q} = (q_x, q_y, q_z)$; d_L is the lattice constant. $m_{BN} = 1/(4t_L d_L^2)$ is the effective band mass. κ_ν , $\nu = x, y, z, \xi$ are coefficients introduced in Eq.(4.19),(4.20). v_ν is the sound velocity of the ν -mode in the small- $|\mathbf{q}|$ limit,

$$v_\alpha^2(\xi) = \frac{M(4b_L G_{\alpha\alpha}(\xi) - c_L)}{m_{BN}}, \quad \alpha = x, y, z, t \tag{4.18}$$

$G_{\alpha\alpha}(\xi)$ and κ_α are a function of ξ

$$\begin{cases} G_{xx} &= \sin^2 \left(\xi - \frac{2\pi}{3} \right) \\ G_{yy} &= \sin^2 \left(\xi + \frac{2\pi}{3} \right) \\ G_{zz} &= \sin^2 (\xi) \\ G_{tt} &= 0 \end{cases}$$

$$\begin{cases} \kappa_x &= \chi_{xx}^2 - \chi_{zz}^2 \\ \kappa_y &= \chi_{yy}^2 - \chi_{zz}^2 \\ \kappa_z &= 0 \\ \kappa_t &= 4(\dot{\chi}_{zz}^2 - \chi_{zz}^2) \end{cases}$$

Here $\dot{\chi}_{zz} = d\chi_{zz}/d\xi$.

When the quadratic Zeeman coupling is zero, the energy dispersion is also derived in the previous chapter. The dispersion of the t -mode in this case is independent of ξ or X_ξ . And among four gapless spin modes, only the x -, y - and z - spin rotational modes contribute to the ξ -dependence of the quantum fluctuation-induced potential V_{qf} . Substituting Eq.(4.16) into Eq.(4.19), one obtains the quantum-fluctuation-induced potential V_{qf} .

When the quadratic Zeeman coupling is present, we find that for $\xi = 0$, $\kappa_{x,y,z,t}$ are not positive defined and collective spin modes can be unstable. To calculate induced-potential V_{qf} , we only include stable modes ($\mathbf{q} \neq 0$) which contribute to the renormalization of adiabatic condensate dynamics. At $\xi = \pi/2$, all collective modes are stable.

4.5.4 Effective Hamiltonian

In the previous section, using the decomposition introduced in Eq.(4.13) we expand the Hamiltonian in Eq.(4.1) in terms of collective coordinates X_ν , \hat{P}_ν and obtain an effective Hamiltonian for submanifold dynamics. Up to the quadratic order, the Hamiltonian contains two sectors, one involving operators of $\mathbf{q} = 0$ -mode and the other one only involving operators of $\mathbf{q} \neq 0$. The Hamiltonian for the $\mathbf{q} = 0$ sector generates the kinetic energy needed for the dynamics along five orthogonal directions. The corresponding effective masses can be expressed in terms of scattering lengths $a_{0,2,4}$, and quadratic Zeeman coupling q_B . In addition, the expansion of the quadratic Zeeman term H_Q for $\mathbf{q} = 0$ mode also generates a mean field potential V_Q . This potential V_Q as illustrated below always favors a biaxial nematic with $\xi = \pi/2$. The biaxial nematic has dihedral-four (Dih_4) symmetries with easy axes in the xy -plane[124]. On the other hand, the sector of Hamiltonian for $\mathbf{q} \neq 0$ collective modes contains zero-point energies of those modes. These energies in general depend on spin configurations or the values of ξ . So quantum fluctuations of collective coordinates effectively induce a ξ -dependent potential V_{qf} in the submanifold; this potential alone selects out a unique ground state as recently pointed out by Song *et al* [124] and Turner *et al* [161]. For rubidium atoms with a positive b_L , previous calculations show that the ground state is a uniaxial nematic in the absence of quadratic

4.5. Effective Hamiltonian for QFCSD

Zeeman coupling. Turner *et al* also pointed out that thermal fluctuations further enhance the amplitude of induced potentials and this order-from-disorder phenomenon is robust against finite temperatures[161].

We now study the dynamical consequences of both quadratic Zeeman coupling H_Q and zero-point quantum fluctuations H_{qf} . For simplicity, we are mainly focused on dynamics around

a) a *uniaxial nematic* at $\xi = 0$ or a condensate with rubidium atoms occupying hyperfine spin state $|2, 0\rangle$;

b) a *biaxial nematic* at $\xi = \pi/2$ or a condensate with rubidium atoms occupying hyperfine spin state $(|2, 2\rangle + |2, -2\rangle)/\sqrt{2}$.

The resultant Hamiltonian for oscillations around a state ξ ($\xi = 0$ or $\pi/2$) can be cast in the following form,

$$\begin{aligned}
 H_{qf} &= \sum_{\nu} \frac{\hat{P}_{\nu}^2}{2N_T m_{\nu}} + N_T (V_{qf}(\xi, X_{\xi}) + V_Q(\xi, X_{\nu})), \\
 V_{qf}(\xi, X_{\xi}) &= \frac{1}{2N_T} \sum_{\mathbf{q} \neq 0} \sum_{\nu} E_{\nu, \mathbf{q}}(\xi, X_{\xi}, q_B), \\
 V_Q(\xi, X_{\nu}) &= \frac{4Mq_B}{3} \cos^2(\xi + X_{\xi}) + 4Mq_B \sum_{\alpha} \kappa_{\alpha} X_{\alpha}^2. \quad (4.19)
 \end{aligned}$$

In Eq.(4.19), N_T is the number of lattice sites and M is the average number of atoms per site. The masses for five directions are calculated to be

$$\begin{aligned}
 m_p &= \frac{1}{a_L + c_L}, \\
 m_t &= \frac{2M}{q_B \kappa_{\xi} - 2Mc_L}, \\
 m_{\alpha} &= \frac{8MG_{\alpha\alpha}}{8Mb_L G_{\alpha\alpha} - 2Mc_L + \kappa_{\alpha} q_B G_{\alpha\alpha}^{-1}}. \quad (4.20)
 \end{aligned}$$

κ_t is a function of ξ and is $-4/3$ when $\xi = 0$, and $4/3$ when $\xi = \pi/2$. $E_{\nu, \mathbf{q}}(\xi, X_{\xi}, q_B)$ is the energy of a mode- ν ($\nu = x, y, z, t, p$) collective excitation with crystal momentum \mathbf{q} , and is a function of parameters ξ, X_{ξ} , and quadratic Zeeman coupling q_B . Only spin modes with $\nu = x, y, z, \xi$ contribute to the ξ -dependence of potential V_{qf} . Fluctuations of phase modes are independent of parameter ξ or Zeeman coupling q_B and are irrelevant for discussions of spin dynamics as a result of spin-phase separation. Note that V_{qf} is a function of ξ, q_B and X_{ξ} ; and V_Q is a function of ξ, q_B and X_{ν} , $\nu = x, y, z, \xi$.

4.6 Potentials Induced by Quantum Fluctuations

We first consider a situation where the quadratic Zeeman coupling is absent and the potential V_Q vanishes. As argued before, generally speaking $V_{qf}(\xi, 0) = V_{qf}(\xi + \pi/3, 0)$ and $V_{qf}(\xi, 0) = V_{qf}(-\xi, 0)$. The explicit form of V_{qf} calculated here indeed is consistent with this general requirement. We also find that the main contribution to V_{qf} is from fluctuations of wavelength $1/(m_{BN}v_\alpha)$ that is much longer than the lattice distance d_L . More specifically, the ξ -dependent induced potential can be written as a sum of polynomials of spin-wave velocities, i.e. $\sum_\alpha v_\alpha^{d+2}$ for d -dimension optical lattices. Spin-wave velocities are functions of c_L, b_L and t_L . We numerically integrate over all wavelengths and obtain the ξ -dependence of V_{qf} as shown in the inset of Fig.4.3.

Consequently, we find that in d -dimension lattices ($d = 2, 3$), the barrier height B_{qf} which is defined as $V_{qf}(\frac{\pi}{6}, 0) - V_{qf}(0, 0)$, the energy difference between $\xi = \pi/6$ and $\xi = 0$ satisfies the following simple scaling function,

$$B_{qf} = \frac{|Mc_L|^{\frac{d+2}{2}}}{t_L^{\frac{d}{2}}} g_d \left(\frac{b_L}{c_L}, \frac{M|c_L|}{t_L} \right). \quad (4.21)$$

Here $g_d(x, y)$ is a dimensionless function that can be studied numerically. This scaling function is either insensitive to the variation of y as for $d = 3$ [124] or independent of y as for $d = 2$. In 3d optical lattices, we find that the ξ -dependent energy potential is proportional to $\sum_\alpha v_\alpha^5 / (d_L^5 t_L^4)$, d_L is the lattice constant and t_L is the hopping integral. In 2d lattices, the ξ -dependent energy potential $V_{qf}(\xi)$ is proportional to $\sum_\alpha v_\alpha^4 / (d_L^4 t_L^3) \ln t_L d_L / v_\alpha$.

Eq.4.21 suggests that one can increase the quantum fluctuation-induced potential by increasing c_L . This is consistent with our intuition that stronger two-body interactions lead to higher quantum fluctuations. As pointed out in Sec.3.3, the microscopic origin of the zero-point spin fluctuations in condensates is the two-body spin-changing scattering, of which the energy scale is the spin-dependent coupling $|c_L|$ in the optical lattices.

Alternatively, one can enhance the quantum fluctuations by increasing the ratio $\frac{c_L}{t_L}$, which is a dimensionless quantity measuring the interaction strength. As a comparison, the interaction strength in single-component Bose gases is measured by the gas parameter $\sqrt{\rho a_s^3}$, in which ρ is the density and a_s is the scattering length. The ‘‘gas parameter’’ for spin dependent interaction strength in optical lattices is $\sqrt{M|c_L^3/t_L^3}$.

One striking consequence of Eq.4.21 is that one can enhance the quantum fluctuation induced potential very effectively by increasing the optical

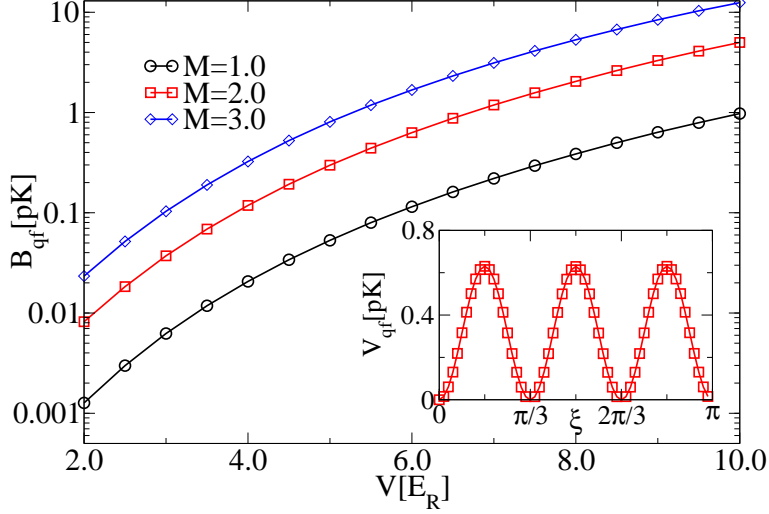


Figure 4.3: (Color online) Barrier height B_{qf} (in units of pK) as a function of optical potential depth V (in units of recoil energy E_R). Inset is for the ξ -dependence of V_{qf} , a potential induced by quantum fluctuations when $V = 6E_R$ and $M = 2.0$.

potential depth V . As shown in Fig.4.1 $|c_L|$ increases and t_L decreases as V increases, both of the changes are enhancing fluctuations. When V increases from $2E_R$ to $10E_R$, $|c_L|$ increases by 4 times, and t_L becomes one-fifth, so B_{qf} is estimated to be enhanced by 1000 times according to Eq.4.21.

We study the barrier height B_{qf} as a function of V , the potential depth of optical lattices. We find that in the absence of lattice potentials or in traps, for a density that is equivalent to one particle ($M = 1.0$) per lattice site the barrier height is of order of 10^{-5} to 10^{-4} pK and is negligible in experiments. When the optical lattice potential depth V is varied, the barrier height typically increases by four or five orders of magnitude. Particularly, as V increases from $2E_R$ to $10E_R$, mean field interaction energies a_L, b_L, c_L vary by less than a factor of three; however, for the same range of V , the barrier height B_{qf} varies from 10^{-3} pK to a few pK. The energy shift between the uniaxial state at $\xi = 0$ and biaxial state at $\xi = \pi/6$ is analogous to the Lamb shift observed in atoms[7]. In Fig.4.3, we show the barrier height B_{qf} of induced potential versus lattice potential depth V .

In Fig. 4.4, we further plot the effective potential $V_{eff} = V_Q + V_{qf}$ as a function of optical potential depth V . When V is less than V_c , the

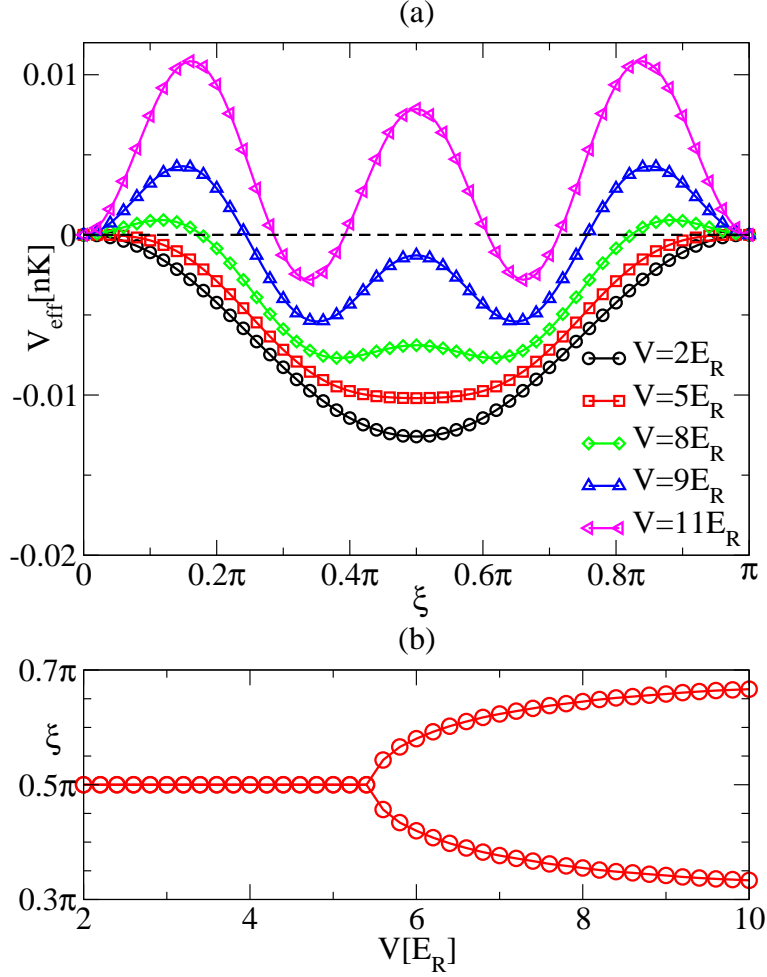


Figure 4.4: (Color online) (a) Effective potential $V_{\text{eff}} = V_Q + V_{qf}$ (in units of nK) as a function of ξ for various optical potential depth V (in units of recoil energy E_R) of 3D lattices. The quadratic Zeeman coupling strength is set to be $10pk(31mG)$ and number of atoms per lattice site M is equal to one. (b) Values of ξ at which global potential minima in (a) are found are plotted as a function of optical potential depth V .

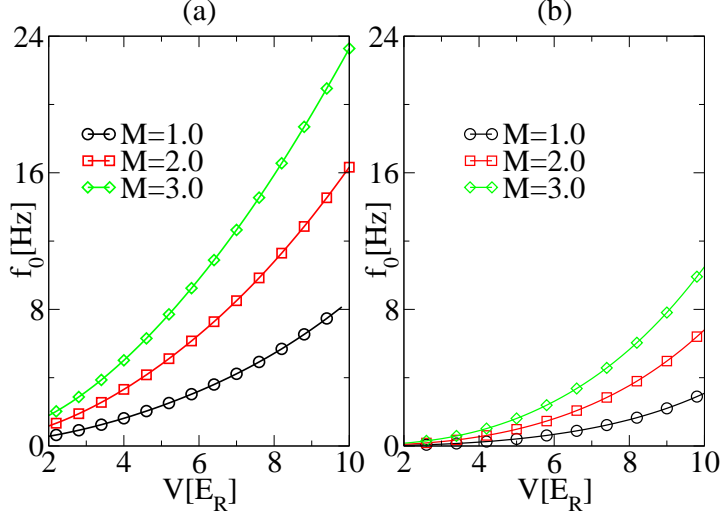


Figure 4.5: (Color online) (a),(b), frequencies $f_0 = \Omega_0/(2\pi)$ for population oscillations around $|2, 0\rangle$ state are shown as a function of potential depth V in (a) 2D and (b) 3D optical lattices for different atom number density M ; here the quadratic Zeeman coupling is absent.

biaxial nematic with $\xi = \pi/2$ is stable and as $V > V_c$, it becomes locally unstable. For ^{87}Rb atoms with one atom per lattice site ($M = 1.0$), V_c is about $5.5E_R$ (E_R is the recoil energy of optical lattices) when the quadratic Zeeman coupling is 10pK. Almost opposite behaviors are found for uniaxial nematics at $\xi = 0$. Values of ξ at which global potential minima are found are shown as a function of V_{eff} in Fig. 4.4b.

4.7 Oscillations Induced by Quantum Fluctuations

To understand the dynamical consequences of V_{qf} , we consider coherent dynamics around the uniaxial nematic state at $\xi = 0$ that is selected out by the fluctuation-induced potential V_{qf} or the biaxial nematic state at $\xi = \pi/2$ that is favored by the quadratic Zeeman potential V_Q . Particularly we are interested in oscillations along the X_t -direction around state $\xi = 0$ or $\pi/2$. These motions correspond to the following time evolution of condensates,

$$|t\rangle \approx (\cos \xi - \sin \xi X_0 F(t)) |2, 0\rangle +$$

4.7. Oscillations Induced by Quantum Fluctuations

$$\frac{1}{\sqrt{2}}(\sin \xi + \cos \xi X_0 F(t))(|2, 2\rangle + |2, -2\rangle);$$

$$F(t) = \cos \frac{\Omega}{2}t + i \frac{m_\xi \Omega}{4M} \sin \frac{\Omega}{2}t$$
(4.22)

where X_0 is the initial deviation from state $\xi = 0$ or $\pi/2$ and m_ξ is the effective mass given in Eq.(4.20). By solving the equation of motion in Eq.(4.19) including the quadratic Zeeman effects, we derive a general expression for oscillation frequencies $\Omega(= 2\pi f)$. The oscillation frequency $\Omega(q_B, V)$ in general is a function of the quadratic Zeeman coupling q_B , optical lattice potential depth V , and the number density M . For population oscillations around $\xi = 0$ or $\pi/2$, we obtain the following frequencies

$$\Omega = 2\sqrt{(\sigma \frac{8Mq_B}{3} + V_{qf}'')(\sigma \frac{2q_B}{3M} + |c_L|)}; \quad (4.23)$$

here $\sigma = \mp 1$ for $\xi = 0$ and $\pi/2$ respectively. V_{qf}'' is the curvature of potentials at $\xi = 0$ or $\pi/2$.

Note that both the real and imaginary part of $F(t)$ oscillate as a function of time; thus unless $\frac{m_\xi \Omega}{4M}$ is exactly equal to one which only occurs when atoms are noninteracting or the quadratic Zeeman coupling q_B is infinite, the magnitude of $F(t)$ oscillates as the time varies. Practically, in most cases we examine below, $m_\xi \Omega$ turns out to be much less than unity because both the curvature V_{qf}'' and the Zeeman coupling q_B are smaller than the inverse of effective mass m_ξ , or the spin interaction energy c_L ; thus oscillations of the imaginary part of $F(t)$ can be neglected. Oscillations along the direction of X_ξ therefore always lead to temporal oscillations in population of rubidium atoms in either $|2, 0\rangle$ or $|2, \pm 2\rangle$ states that can be observed in experiments.

We first examine the cases when the quadratic Zeeman coupling is absent i.e. $q_B = 0$. The frequency in this limit is a direct measure of quantum fluctuations and $\Omega_0 = \Omega(q_B = 0, V) = 2\sqrt{V_{qf}''|c_L|}$. In the absence of lattice potentials, or in traps we find that oscillation frequencies are about 10^{-3} Hz. At finite temperatures, thermal fluctuations do enhance oscillation frequencies by a factor of two to four; however, this is far from sufficient for the experimental study of *QFCSD* within the life time of these isotopes[39].

In optical lattices, we find that the enhancement of spin-dependent interactions b_L, c_L , and especially the rapid increasing of band mass m_{BN} can result in oscillation frequencies of order of a few Hz, which are about three to four orders of magnitude higher than those in traps. The scaling behavior

4.7. Oscillations Induced by Quantum Fluctuations

of Ω_0 is closely related to that of B_{qf} . Taking into account the expression for effective mass m_ξ , we find

$$\Omega_0 \sim \frac{M^{\frac{d+2}{4}} |c_L|^{\frac{d+4}{4}}}{t_L^{\frac{d}{4}}} g_d^{\frac{1}{2}} \left(\frac{b_L}{c_L}, \frac{M|c_L|}{t_L} \right). \quad (4.24)$$

In Fig. 4.5, we show the plot of $f_0 = \Omega_0/2\pi$, the oscillation frequency versus V in the absence of Zeeman coupling q_B .

Experimental studies of *QFCS*D can also be carried out by investigating dynamics of rubidium atoms in the presence of finite quadratic Zeeman coupling q_B . The submanifold dynamics now are driven by both quadratic Zeeman coupling and quantum fluctuations. There are three main modifications to the effective Hamiltonian H_{eff} . Firstly, according to Eq.(4.20), effective masses now depend on the quadratic Zeeman coupling q_B . Secondly, following discussions in the *appendix*, among four spin collective modes ($\nu = x, y, z, t$) and one phase mode ($\nu = p$), two of spin modes, x - and y -mode, can be gapped and one, z -mode, always remains gapless. Details of spectra of ξ -mode depend on the value of ξ ; excitations are unstable when κ_ξ is negative and are gapped when κ_ξ are positive. The energy gap of stable ξ -mode excitations depends on ξ and becomes maximal at $\xi = \pi/2$. Finally, a mean field quadratic Zeeman potential that depends on X_ξ and X_α , $\alpha = x, y, z$, is also present and modifies the spin dynamics. Oscillation frequencies Ω as a function of quadratic Zeeman coupling q_B for various potential depth V can be calculated explicitly using Eq.(4.23). Plots of these results are shown in Fig.4.6,4.7.

In the limit of weak quadratic Zeeman coupling, *QFCS*D can be most conveniently studied around the uniaxial nematic state at $\xi = 0$, or $|2, 0\rangle$ state. For rubidium atoms, this is the ground state when the quadratic Zeeman coupling is absent, and remains to be locally stable along the direction of X_t up to a finite q_{c1} . When the quadratic Zeeman coupling q_B is much smaller than q_{c1} , the effective potential V_{eff} is mainly due to the quantum-fluctuation induced one, V_{qf} . Above q_{c1} , a dynamical instability occurs and a perturbation along the X_ξ -direction around $|2, 0\rangle$ starts to grow exponentially. We find that in traps where $V = 0$, q_{c1} is about 10^{-2} pK; in optical lattices when V varies between $2E_R$ to $10E_R$, the value of q_{c1} increases from 0.1pK up to about 0.1nK. And as q_B approaches zero, the oscillation frequency $\Omega(q_B, V)$ saturates at the value Ω_0 shown in Fig.4.5. The q_B -dependence of frequencies for oscillations around $\xi = 0$ is shown in Fig.4.6; near $q_B = q_{c1}$, the frequencies scale as $\sqrt{q_{c1} - q_B}$. Alternatively, one can also study oscillations around states at which global potential minima

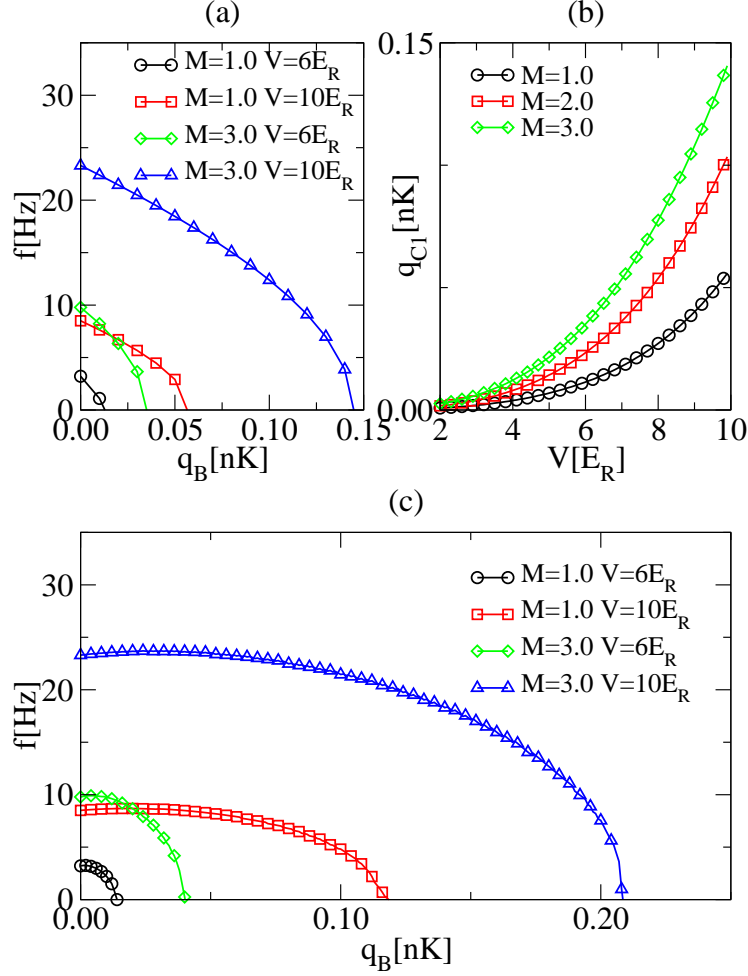


Figure 4.6: (Color online) Frequencies $f = \Omega/(2\pi)$ for population oscillations as a function of quadratic Zeeman coupling q_B (in units of nK) for various potential depth V in 2D optical lattices with M atoms per lattice site. (a) for oscillations along the X_t -direction around state $|2, 0\rangle$; dynamics are unstable above a threshold $q_{c1}(V)$. The V -dependence of q_{c1} (in units of nK) is shown in (b). (c) is for oscillations around states with $\xi = \xi_m (< \pi/2)$ at which global potential minima shown in Fig.4.4(a) are found. (see also Eq.(4.22))

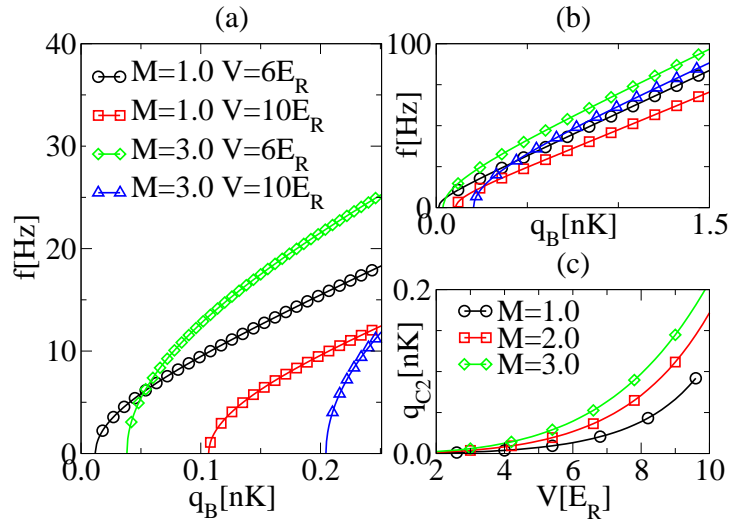


Figure 4.7: (Color online) (a), (b) Frequencies $f = \Omega/(2\pi)$ for oscillations along the X_t -direction around biaxial nematic state $|2, 2\rangle + |2, -2\rangle$ versus quadratic Zeeman coupling q_B (in units of nK) for various optical potential depth V in 2D optical lattices with M atoms per lattice site. (a) is for population oscillations close to the threshold q_{c2} and (b) is for away from q_{c2} . Oscillations are unstable below a threshold q_{c2} ; in (c), q_{c2} (in units of nK) as a function of V is shown.

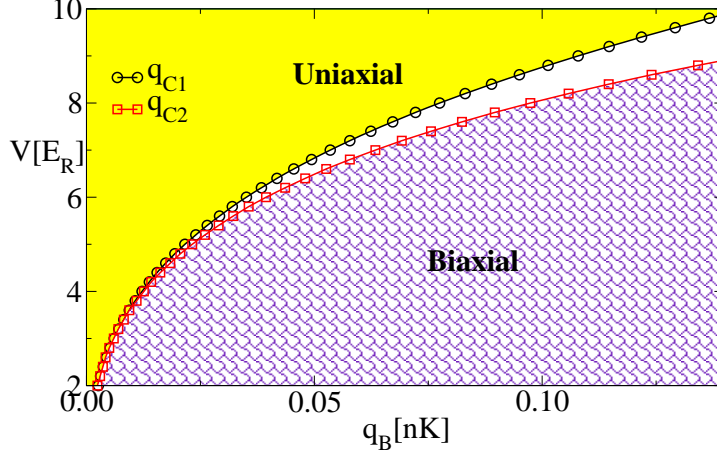


Figure 4.8: (Color online) Regions of dynamical stability in the $V - q_B$ plane for three particles per lattice site ($M = 3.0$). Oscillations around uniaxial nematic or state $|2, 0\rangle$ (biaxial nematic or state $|2, 2\rangle + |2, -2\rangle$) are locally stable along the X_ξ -direction in the yellow shaded (purple patterned) area; dynamical instabilities occur when $q_B > q_{c1}(V)$ ($q_B < q_{c2}(V)$). q_B is in units of nK.

of V_{eff} are found; similar q_B -dependence is shown in Fig.4.6c.

At relatively high frequencies, convenient oscillations to investigate are the ones along the X_t direction around the biaxial nematic state at $\xi = \pi/2$ point or $(|2, 2\rangle + |2, -2\rangle)/\sqrt{2}$ state. This state becomes stable when q_B is larger than q_{c2} and oscillations are well defined only in this limit. When q_B is smaller than this critical value, the dynamics are mainly driven by quantum fluctuations and oscillations are unstable. In the vicinity of q_{c2} , the oscillation frequency again scales as $\sqrt{q_B - q_{c2}}$. When q_B is much bigger than q_{c2} but smaller than c_L , the frequency is proportional to $\sqrt{q_B}$; in this limit, the potential V_{eff} is already dominated by the quadratic Zeeman term, or V_Q , but the effective mass is mainly induced by spin dependent interactions.

When the quadratic Zeeman coupling further increases well above the value of c_L , relatively fast dynamics are now mainly driven by the external coupling and the frequency Ω approaches $8q_B/3$, which is equal to the quadratic Zeeman splitting between state $|2, 0\rangle$ and $|2, \pm 2\rangle$. In this limit, scattering between atoms during a short period of $2\pi/\Omega$ becomes

negligible; the population oscillations due to scattering or interactions are therefore significantly suppressed as here hyperfine spin two atoms are effectively *noninteracting*. Indeed, following the expression for $F(t)$ in Eq.(4.22) and Eq.(4.20),(4.23), one finds that the amplitude of population oscillations scales as $1/q_B$ at large q_B limit and $F(t)$ becomes $\exp(i4q_B t/3)$ when q_B approaches infinite, i.e., a pure phase factor with a constant modulus.

In Fig.4.7, we show that the q_B -dependence of oscillation frequencies both close to the threshold q_{c2} and away from q_{c2} . As we have mentioned before, *QFCS*D is rather sensitive to the variation in V . q_{c1} and q_{c2} as functions of V are shown in Fig. 4.6,4.7.

So far we have studied coherent dynamics driven by potentials induced by quantum fluctuations at zero temperature. In the following section, we analyze the effect of temperatures, or thermal fluctuations.

4.8 Effects of Thermal Fluctuations

We now turn to the effect of temperatures and focus on three-dimension optical lattices. At a finite temperature, collective modes including spin waves are thermally excited. The occupation number of α th spin-wave excitations with momentum $\hbar q$ and energy $E_{\alpha,q}$ is

$$n(\alpha, q) = \frac{1}{e^{\frac{E_{\alpha,q}}{kT}} - 1}. \quad (4.25)$$

The free energy density (or per lattice site) of a condensate characterized by ξ is

$$F(\xi, T, V) = \frac{1}{N_T} \sum_{\alpha,q} \left(\frac{E_{\alpha,q}}{2} + kT \ln(1 - e^{-\frac{E_{\alpha,q}}{kT}}) \right). \quad (4.26)$$

Just as in the zero temperature case because of the ξ -dependence of spin wave velocities, the free energy density also depends on the values of ξ and the main contribution to the ξ -dependence of free energy density is again from fluctuations of wavelength $1/(m_{BN}v_\alpha)$, or of a characteristic energy T_* that is of an order of $|c_L|$ (or b_L). Thermal fluctuations become more important than quantum ones when temperatures are much higher than T_* . The other temperature effect is from the temperature dependence of spin wave velocities v_α . Because of the thermal depletion, spin wave velocities v_α ($\alpha = x, y, z$) decrease as temperatures increase and become zero when the BEC temperature T_{BEC} is approached. Therefore the temperature

4.8. Effects of Thermal Fluctuations

dependence of free energy are determined by two dimensionless quantities, T/T_* and T/T_{BEC} . In all cases we are going to study below, T_* (of order of $-c_L$) is less or much less than T_{BEC} .

We study the asymptotics of free energy in low temperature ($T \ll T_*$) and high temperature ($T \gg T_*$) limits. When $T \ll T_*$, only modes with energy much smaller than T_* are thermally occupied. Therefore contributions from these thermal excitations can be calculated by substituting quasi-particle spectra $E_{\alpha,q}$ approximately with phonon-like spectra $v_\alpha q$. One then obtains the following expression for the free energy per lattice site (up to a constant)

$$F(\xi, T, V) = V_{qf} \left(1 - \left(\frac{T}{T_{BEC}}\right)^{\frac{3}{2}}\right)^{\frac{5}{2}} - \frac{\pi^2 kT}{90} \sum_{\alpha} \left(\frac{d_L kT}{v_\alpha}\right)^3. \quad (4.27)$$

The barrier height, $B_{th}(T, V) = F(\xi = \frac{\pi}{6}, T, V) - F(\xi = 0, T, V)$, can be calculated accordingly and the asymptotics at low temperatures is

$$B_{th}(T, V) - B_{th}(0, V) \sim \frac{|c_L|^{5/2}}{t_L^{3/2}} \left(\frac{kT}{|c_L|}\right)^4. \quad (4.28)$$

Here we have neglected the term depending on T/T_{BEC} because we are interested in temperatures much less than T_{BEC} . (Such a term is only important at very low temperatures that are of an order of $|c_L|(|c_L|/T_{BEC})^{3/5}$ ($\ll T_*$)). Therefore, the low temperature enhancement of B_{th} is mainly from the "black-body" radiation of spin wave excitations.

When $T \gg T_*$, spin modes with energy much bigger than T_* are thermally occupied. For modes of energy T_* , we can approximate $n(\alpha, q)$ with a classical result $n(\alpha, q) = kT/E_{\alpha,q}$. Our scaling analysis of the free energy per lattice site shows that in this limit,

$$F(\xi, T, V) = -\frac{2kT}{3\pi} \sum_{\alpha} \left(\frac{v_\alpha}{4d_L t_L}\right)^3 \left(1 - \left(\frac{T}{T_{BEC}}\right)^{\frac{3}{2}}\right)^{\frac{3}{2}}. \quad (4.29)$$

The barrier height, $B_{th}(T, V) = F(\xi = \frac{\pi}{6}, T, V) - F(\xi = 0, T, V)$, can be calculated accordingly and asymptotics at high temperatures are

$$B_{th}(T, V) \sim \frac{c_L^{5/2}}{t_L^{3/2}} \frac{kT}{c_L} \left(1 - \left(\frac{T}{T_{BEC}}\right)^{\frac{3}{2}}\right)^{\frac{3}{2}}. \quad (4.30)$$

The above result shows that at relatively high temperatures thermal spin wave fluctuations enhance induced potentials and this enhancement is characterized by a linear function of $kT/|c_L|$ or kT/T_* . However, because of the thermal depletion of condensates at finite temperatures, there is an overall suppression given by a factor $1 - (T/T_{BEC})^{3/2}$. The competition between these two effects results in a maxima in the free energy density. That is at temperatures larger than T_* but much smaller than T_{BEC} , the free energy increases linearly as a function of temperature until the thermal depletion becomes significant. The maximal enhancement is therefore about T_{BEC}/T_* . At further higher temperatures, the free energy density decreases and near T_{BEC} , its temperature dependence is mainly determined by a factor $(1 - (T/T_{BEC})^{3/2})^{3/2}$ as shown in Eq.(4.30).

Evidently, the magnitude of maximal enhancement is very much dependent on the ratio between T_{BEC} and T_* . In optical lattices, the magnitude of BEC transition temperatures for, on average, one or two particles per lattice is mainly set by the band width t_L while T_* is determined by $|c_L|$. This ratio and therefore the enhancement is quite sensitive to the optical lattice potential depth V . We find that the enhancement in the absence of lattice potentials is substantial and thermal fluctuations increase the induced potential by about a factor of fifty. This is consistent with a previous calculation[161]. However, when the lattice potential depth increases, c_L increases but t_L decreases, the thermal enhancement becomes much less significant. At $V = 10E_R$, we find that the thermal effect only increases the potential by a few tens of percent and the potential can be predominately due to quantum fluctuations.

4.9 Effects of Spin Exchange Losses

For $F = 2$ rubidium atoms, the life time is mainly due to spin exchange losses that take place at a relatively short time scale of about 200ms[39, 87]. Note that three-body recombination usually occurs at a much longer time scale and has little effect on the time evolution studied here. Spin exchange losses put a very serve constraint on possible observations of *full* coherent oscillations driven by quantum fluctuations at frequencies well below 5Hz. To overcome this difficulty, we suggest to apply a quadratic Zeeman coupling close to q_{c1} (q_{c2}) and study time evolution of state $|2, 0\rangle$ or $\frac{1}{\sqrt{2}}(|2, 2\rangle + |2, -2\rangle)$. Regions of dynamical stability of these states can be obtained by studying small oscillations around them as shown in section III. Results are summarized in Fig.4.8.

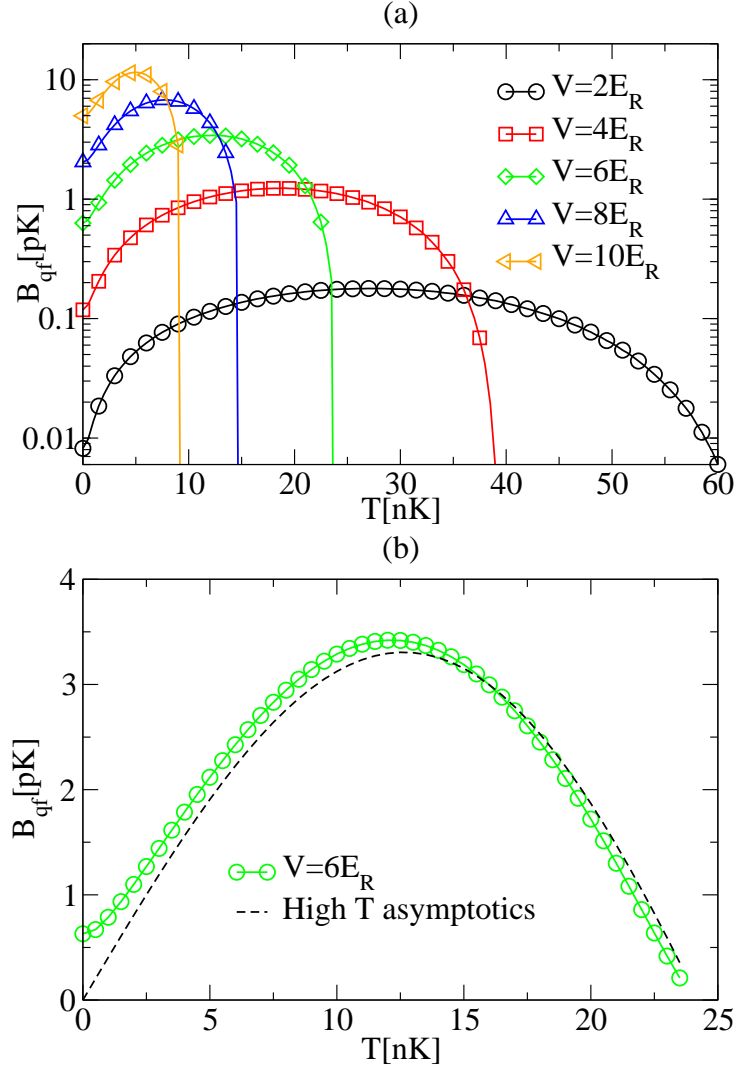


Figure 4.9: (Color online) Induced free energy barrier height as a function of temperature for different lattice potentials. The dashed line in (b) is a plot for the high temperature asymptotics derived in Eq.(4.29). Note that thermal enhancement of barrier height is much less significant in deep optical lattices.

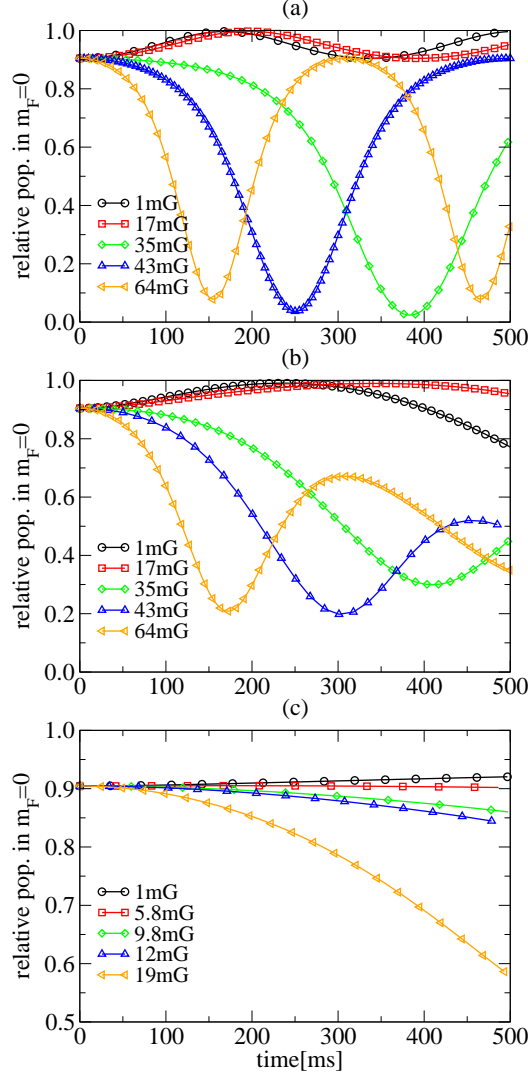


Figure 4.10: (Color online) Estimated time evolution of rubidium population at $|2, 0\rangle$ hyperfine spin state when the quadratic Zeeman coupling or Zeeman field varies. (a) and (b) are for optical lattices with potential depth $V = 10E_R$ and (c) is for $V = 6E_R$. In (a), we assume the density is uniform and there are no spin losses while (b) and (c) are for traps with inhomogeneous density and a finite loss rate $1/\tau = (200ms)^{-1}$. In (a),(b),(c), magnetic fields which yield dynamical critical quadratic Zeeman coupling $q_{c1}(\sim q_{c2})$ are $35mG$, $35mG$ and $10mG$ respectively.

Dynamical stabilities of $|2, 0\rangle$ state below the threshold q_{c1} , or instabilities of $(|2, 2\rangle + |2, -2\rangle)/\sqrt{2}$ state below threshold q_{c2} are directly induced by quantum fluctuations. Coherent quantum dynamics around state $|2, 0\rangle$ ($(|2, 2\rangle + |2, -2\rangle)/\sqrt{2}$) below and above dynamical critical coupling q_{c1} (q_{c2}) are qualitatively different and it is therefore plausible to probe these dynamics that are driven mainly by quantum fluctuations at relative low frequencies. To explore this possibility, we have studied strongly damped population oscillations around a condensate $|2, 0\rangle$ or a uniaxial state, at different quadratic Zeeman couplings when the spin exchange loss time is set to be 200ms. For this part of calculations we also take into account the density inhomogeneity of rubidium atoms in traps. Main results are shown in Fig.4.10 for different magnetic fields; at a given field, the corresponding quadratic Zeeman coupling is given as $q_B = 3(\mu_B B/2)^2/(6.8\text{GHz})$.

Our major findings are three-folded and outlined below. Firstly, for a condensate with small deviations from $|2, 0\rangle$ state, because of fast spin exchange losses complete coherent oscillations around $|2, 0\rangle$ are hard to observe. Secondly, dynamics can be dramatically modified by a finite quadratic Zeeman coupling. When the coupling is much less than q_{c1} (defined for the density at the center of a trap), dynamics become slower when the quadratic Zeeman coupling increases. Beyond q_{c1} , dynamics become faster while the quadratic Zeeman coupling increases. These behaviors are consistent with results for the case of uniform density shown in the previous section; there, the oscillation frequency becomes zero at a dynamical critical coupling.

Thirdly (and perhaps most importantly), the population of atoms at state $|2, 0\rangle$ always *grows* initially at short time scales when the quadratic Zeeman coupling is zero or smaller than q_{c1} , as a direct consequence of dynamical stabilities of a $|2, 0\rangle$ -condensate. By contrast, beyond q_{c1} the population of atoms at state $|2, 0\rangle$ always *decreases* initially at short time scales as a result of dynamical instabilities in this limit. These two distinct short-time behaviors of population at state $|2, 0\rangle$ are signatures of a transition from quantum-fluctuation driven dynamics to a mainly quadratic Zeeman coupling driven dynamics. In the presence of strong spin losses, observing these distinct short-time asymptotics is an effective way to probe many-body quantum fluctuations in condensates we have considered. At very large quadratic Zeeman coupling, we have found expected rapid oscillations corresponding to mean field coherent dynamics and we don't show those results here. Finally, we also estimate the time-dependence of population oscillations at finite temperatures using thermal-fluctuation induced potentials discussed in a previous section. Thermal fluctuations usually speed up the coherent dynamics around state $|2, 0\rangle$ when the quadratic Zeeman cou-

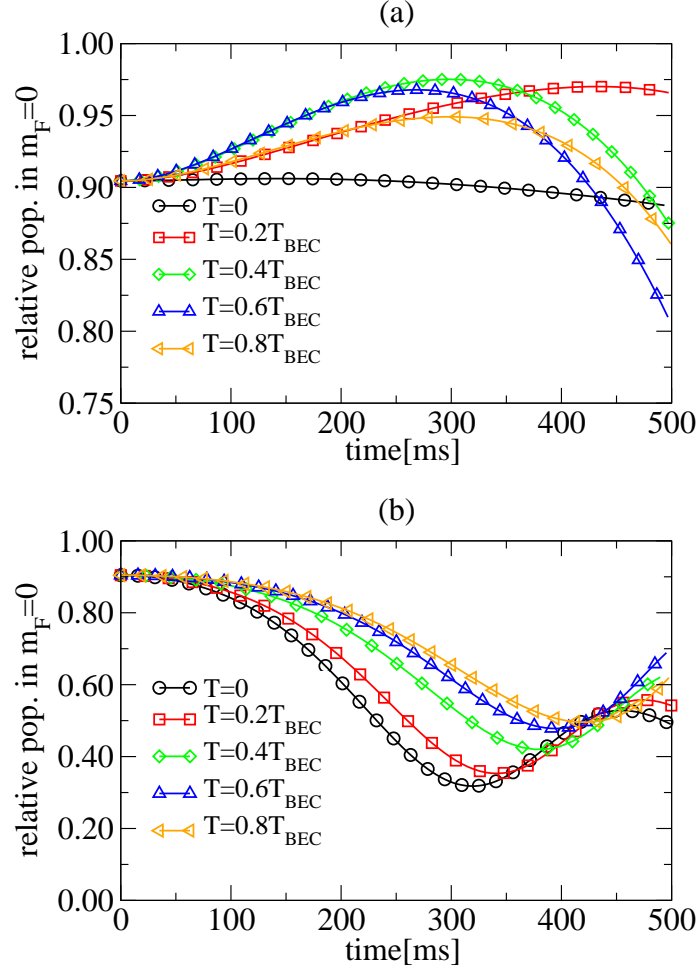


Figure 4.11: (Color online) Estimated time evolution of population at $|2, 0\rangle$ state at different temperatures. (a) is for a magnetic field of $13mG$ that is below the dynamical critical field corresponding to q_{c1} and (b) is for $38mG$ field which is above q_{c1} . The optical lattice potential depth is $V = 8E_R$, $T_{BEC} = 10.9nK$ and the spin exchange life time is again set to be $200ms$. Density inhomogeneity in traps has also been taken into account to obtain these plots.

pling is sufficiently weak (smaller than q_{c1}); on the other hand, they can also slow down coherent dynamics around state $|2, 2\rangle + |2, -2\rangle$ when a quadratic Zeeman coupling larger than q_{c2} is present. These results are shown in Fig.4.11. In obtaining these results, we have extrapolated the linear dynamical analysis into a regime where oscillation amplitude is substantial. So strictly speaking, results for $35mG$, $44mG$, $65mG$ magnetic fields shown in Fig.4.10(b) are qualitative. However, short-time asymptotics that are the focuses of our discussions here are accurate.

4.10 Estimates of Condensate Fraction

In this section, we estimate the condensate in optical lattices both at zero temperature and finite temperatures. An important reason for such an estimation is to verify the validity of perturbative calculation that we have carried out in the previous section. The perturbative calculation or Bogoliubov approximation only works well when depletion fraction is much smaller than one. The major results are summarized in Fig.4.12. In the range when $2 < \frac{V}{E_R} < 10$ the quantum depletion is smaller than $\frac{1}{5}$, and our perturbative calculation should suffice. Another reason to estimate the condensation fraction is to understand how the fluctuation-induced barrier depends on temperature, which is studied in the previous section.

To study the condensate depletion in the optical lattice, we start from the effective Hamiltonian. Five collective modes on top of a nematic state are described by the following:

$$\mathcal{H} = \sum_{\nu,q} E_{\nu,q} \left(\tilde{\theta}_{\nu,q}^\dagger \tilde{\theta}_{\nu,q} + \frac{1}{2} \right). \quad (4.31)$$

Here $\tilde{\theta}_{\nu,q}^\dagger$ and $\tilde{\theta}_{\nu,q}$ are bosonic creation and annihilation operators for the ν -th mode. These operators can be obtained by Bogoliubov transformations:

$$\tilde{\theta}_{\nu,q} = u_{\nu,q} \theta_{\nu,q} + v_{\nu,q} \theta_{\nu,-q}^\dagger, \quad (4.32)$$

$$\tilde{\theta}_{\nu,q}^\dagger = u_{\nu,q}^* \theta_{\nu,q}^\dagger + v_{\nu,q}^* \theta_{\nu,-q}. \quad (4.33)$$

The coefficients $u_{\nu,q}$ and $v_{\nu,q}$ are given:

$$u_{\nu,q} = \frac{1}{\sqrt{2}} \left(\sqrt{1 + \frac{m_{BN} v_{\nu,q}^2}{E_{\nu,q}}} + 1 \right)^{1/2}, \quad (4.34)$$

$$v_{\nu,q} = \frac{1}{\sqrt{2}} \left(\sqrt{1 + \frac{m_{BN} v_{\nu,q}^2}{E_{\nu,q}}} - 1 \right)^{1/2}. \quad (4.35)$$

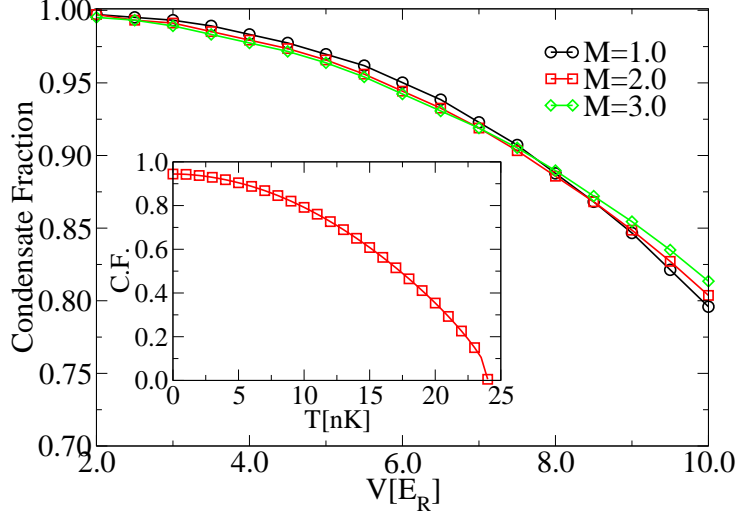


Figure 4.12: (Color online) Condensation fraction versus optical lattice potential depth V (in units of E_R). The inset shows the condensate fraction at different temperatures when V is equal to $6E_R$.

Condensate deletions from the ν -th mode with crystal momentum \mathbf{q} are

$$\langle \theta_{\nu,q}^\dagger \theta_{\nu,q} \rangle = (u_{\nu,q}^2 + v_{\nu,q}^2) \langle \tilde{\theta}_{\nu,q}^\dagger \tilde{\theta}_{\nu,q} \rangle + v_{\nu,q}^2. \quad (4.36)$$

Here $\langle \tilde{\theta}_{\nu,q}^\dagger \tilde{\theta}_{\nu,q} \rangle$ is the occupation number of the ν th mode and it is given by the Bose-Einstein statistics:

$$\langle \tilde{\theta}_{\nu,q}^\dagger \tilde{\theta}_{\nu,q} \rangle = \frac{1}{\exp(E_{\nu,q}/kT) - 1}. \quad (4.37)$$

Putting all these together, we reach the final equation to determine the condensate density:

$$M - M_0(T) = \frac{1}{N_T} \sum_{\nu,q \neq 0} \left(v_{\nu,q}^2 + \frac{u_{\nu,q}^2}{e^{\frac{E_{\nu,q}}{kT}} - 1} \right). \quad (4.38)$$

M is the atom number density or number of atoms per lattice site and M_0 is the condensed number density. The first term in the summation gives quantum depletion number due to the two body scattering and the second term gives the thermal depletion number. We solve the above equation numerically and the results are shown in Fig.4.1.

4.11. Conclusion

At zero temperature, quantum depletion is given by the term $v_{\nu,q}^2$ which captures the effect of interactions or two body scattering processes. Our estimate shows that

$$\begin{aligned}
 1 - \frac{M_0}{M} &\sim \sum_{\nu=p,\xi,x,y,z} \frac{1}{M} \left(\frac{m_{BN}v_\nu}{t_L d_L} \right)^3 \\
 &\sim \frac{1}{M} \left(\frac{M a_L}{t_L} \right)^{3/2}.
 \end{aligned} \tag{4.39}$$

We have noticed that major contributions are from the phase fluctuations since $a_L \gg |b_L|, |c_L|$. In optical lattices when the potential depth V increases, the bandwidth t_L decreases exponentially as a function of V and a_L increases; as a result, quantum depletion grows as $(\frac{a_L}{t_L})^{3/2}$.

At finite temperatures, M_0 decreases as temperature T increases and becomes zero at the transition temperature T_{BEC} . In the weakly interacting limit ($t_L \gg a_L, b_L, |c_L|$), the condensate fraction is approximately equal to

$$\frac{M_0(T)}{M_0(T=0)} = 1 - \left(\frac{T}{T_{BEC}} \right)^{\frac{3}{2}}, \tag{4.40}$$

and $T_{BEC} \sim 5M_0^{2/3}t_L$ in optical lattices.

4.11 Conclusion

In conclusion, we have demonstrated that unlike the usual mean-field-interaction driven coherent dynamics, *QFCSD* is a novel class of coherent dynamics fully driven by quantum fluctuations. These dynamics are conveniently tunable in optical lattices where oscillation frequencies can be varied by three to four order of magnitude. Frequencies of oscillations driven by quantum fluctuations have both distinct lattice-potential dependence and quadratic Zeeman-coupling dependence that can be studied experimentally. For rubidium atoms, *QFCSD* can be directly probed either at frequencies of a few Hz or when the quadratic Zeeman coupling is about 10^{-1} nK. One of potential applications of *QFCSD* perhaps is the possibility of performing precise measurements of strongly correlated quantum fluctuations and critical exponents near quantum critical points. Current studies of critical correlations are based on analyzing statistics of interference fringes[162, 74]. Given the great control of coherent dynamics recently demonstrated for cold atoms[10], we would like to believe that quantum-fluctuation controlled dynamics might

4.11. Conclusion

be an alternative and promising path towards probing critical correlations. Finally, we have also investigated the effects of finite temperatures, spin exchange losses and studied time evolution of condensates mainly driven by quantum fluctuations.

Chapter 5

Half Quantum Vortex (HQV) in $F = 1$ Superfluids of Ultracold Atoms

5.1 Introduction

Topological excitations such as quantized vortices have been fascinating for quite a few decades and recently have also been well studied in Bose-Einstein condensates (BECs) of ultracold atoms [49, 50, 51, 163, 164, 165, 166, 167, 168]. In spinor condensates the rich magnetic structure can give rise to many exotic topological defects such as quantum vortices with fractionalized circulations, monopoles and skyrmions. The existence of stable topological defects is related to the topology of magnetic order parameters. In a conventional superfluid, the complex-valued scalar order parameter has a topology equivalent to a unit circle S_1 which supports quantum vortices; in spinor condensates, the vector order parameter can have complicated topologies such as $\frac{SO(3) \times U(1)}{T}$ [125] in the cyclic phase of $F = 2$ spinor condensates mentioned in Chap.3 or $\frac{S_2 \times S_1}{Z_2}$ [123] in nematic phase of $F = 1$ spinor systems which is the focus of this chapter. Topological defects other than the integer quantized vortices were previously studied in other physical systems such as superfluid helium-3 [169, 170] and liquid crystals [171].

In this chapter we are going to examine half quantum vortices (HQVs) in $F = 1$ spinor systems, especially the emergent topological order and fractionalization phenomena due to strong spin fluctuations in two-dimension superfluids. Quantum number fractionalization has been one of the most fundamental and exciting concepts studied in modern many-body physics and topological field theories [172, 173, 174, 175]. In more recent theoretical studies of strongly correlated two-dimension electrons [176, 177, 178, 179, 180, 181], spin-charge separated fractionalized excitations in spin liquids and the underlying topological order have also been focuses of many investigations although their experimental realization is still under exten-

sive debate[182]. Very recently, low dimensional fractionalized quantum states have further been proposed to be promising candidates for carrying out fault tolerant quantum computation[183]. Given the availability of low dimensional cold gases[74], in this chapter we propose to explore fractionalization phenomena in superfluids of ultracold sodium atoms which can potentially be studied in experiments[38]. Particularly, we investigate fluctuation-driven fractionalization of circulation quantum and topological order in two-dimension quantum gases where spin correlations are short ranged.

Fractionalized phases in spinor gases characterized by the topological order are previously studied in [128] and [129, 131], where a novel spin singlet condensate with distinct symmetries and excitations has been found. It breaks the $U(1)$ gauge symmetry but not the $SO(3)$ rotational symmetry; spin-charge separation have been also found in the spin single condensate in some one-dimension Mott states[129, 131].

In the first part of this chapter I describe the structure and interactions of HQVs in the spinor condensates using mean field theory. In the following part I study the HQVs with strong fluctuations in 2D spinor superfluids. Finally I study the nucleation of the HQVs in 2D spinor superfluids in rotating traps.

5.2 HQV in Spinor Bose-Einstein Condensates

Topological excitations such as quantized vortices have been fascinating for quite a few decades and recently have also been thoroughly studied in Bose-Einstein condensates (BECs) of ultracold atoms [49, 50, 51, 163, 184, 164, 165, 166, 167, 168]. For vortices in single-component BECs, the circulation of supercurrent velocity \mathbf{v}_s along a closed curve Γ around a vortex line

$$\mathcal{C} = \int_{\Gamma} d\mathbf{l} \cdot \mathbf{v}_s \quad (5.1)$$

is quantized in units of $\frac{2\pi\hbar}{m}$ (m is the atomic mass), with $\mathcal{C} = \pm 1, \pm 2, \dots$ as a consequence of *analyticity* of single-valued wavefunctions of coherent quantum states. Furthermore, only a vortex with circulation $\mathcal{C} = \pm 1$ or an elementary vortex is energetically stable. A secondary vortex with circulation $\mathcal{C} = \pm 2, \pm 3, \dots$ spontaneously splits into a few elementary ones which interact via long-range repulsive potentials.

A configuration with its circulation smaller than the elementary value ($\mathcal{C} = 1$) has to be described by a singular wavefunction and it always turns

out to be energetically catastrophic. A most obvious example is a two-dimension configuration, where the condensate phase angle $\Phi(r, \theta)$ rotates slowly and uniformly by 180° in the $r - \theta$ plane around a vortex center but jumps from π to 2π when the polar angle θ is equal to 2π . The π -phase jump here effectively induces a singular *cut* in the wavefunction. The corresponding circulating velocity field is simply

$$\mathbf{v}_s(r, \theta) = \frac{\hbar}{2mr} \mathbf{e}_\theta \quad (5.2)$$

, leading to $\mathcal{C} = 1/2$ that is one-half of an elementary value. The energy of a *cut* per unit length along $\theta = 2\pi$ line where the phase jumps is finite and therefore the overall energy of a *cut* in an individual fractionalized vortex scales as L , L is the size of system, while the energy for an integer vortex only scales as a logarithmic function of L . Consequently, a *cut* that connects two singular fractionalized vortices mediates a linear long rang *attractive* potential that confines all fractionalized excitations(see Fig.5.1(a)). So in a single-component condensate, vortices with $\mathcal{C} = \pm 1$ are fundamental ones which do not further split into smaller constituent elements as a result of confinement of fractionalized vortices.

Hyperfine-spin degrees of freedom can drastically change the above arguments about elementary vortices. In condensates of sodium (^{23}Na) or rubidium (^{87}Rb) atoms in optical traps [38], hyperfine spins of cold atoms are correlated because of condensation. A *pure* spin defect (or a spin disclination in the case of ^{23}Na) where spins of cold atoms slowly rotate but no supercurrents flow, can carry a *cut*, i.e. a line along which a π -phase jump occurs as a result of Berry's phases induced by spin rotations [149]. Such a spin defect can then terminate a *cut* emitted from a singular half-quantum vortex (HQV) configuration, which consequently leads to a linear confining potential between the spin defect and HQV(see Fig.5.1(c) and (d)). For instance, a HQV with $\mathcal{C} = 1/2$ confined to a spin defect does exist as a fundamental excitation in spin nematic condensates [123, 185].

In this section we will explore the magnetic structure of a single HQV and interactions between HQVs. I will also present the simulation of dynamical creation of fractionalized HQVs in a rotating BEC of sodium atoms, and briefly formulate an experimental procedure for the realization of such exotic topological excitations.

5.2.1 Magnetic Properties and Energetics of HQV

Unlike conventional integer vortices, HQVs have a rich magnetic structure. We will demonstrate that far away from its core a HQV has vanishing lo-

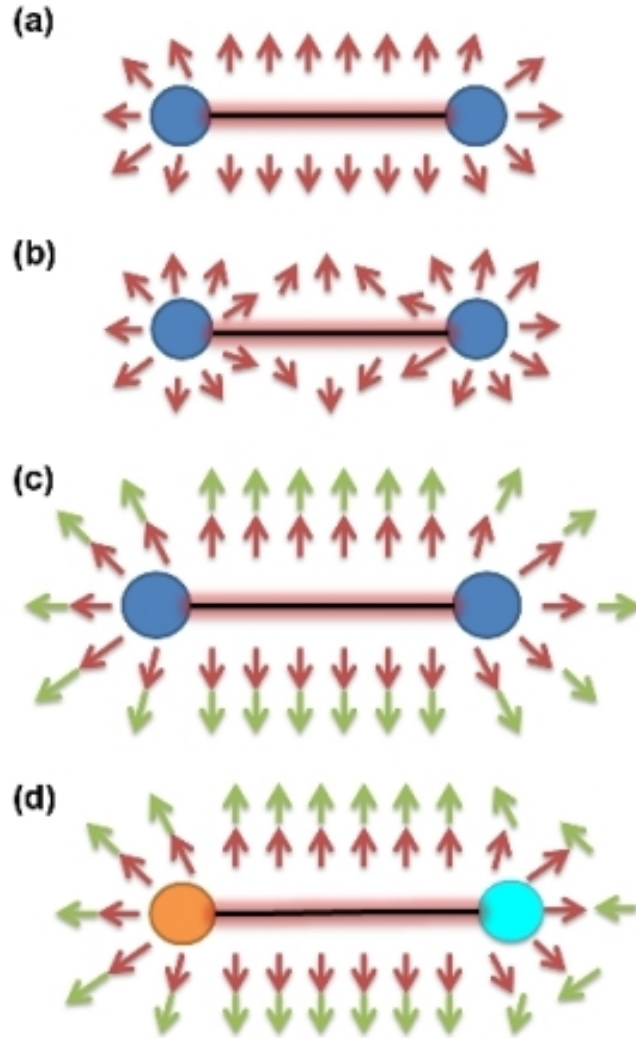


Figure 5.1: Two quantum vortices separated at a distance. (a) A HQV in a single-component BEC. (b) Two IQVs in a single-component BEC. (c) Two HQVs (both are positive types) in a spinor BEC. (d) Two HQVs (one positive and one negative) in a spinor BEC. Red arrows represent the phase vectors, and green arrows represent the spin vectors.

cal spin densities but is accompanied by slowly rotating spin quadrupole moments; within the core, spin densities are nonzero.

The Hamiltonian for interacting sodium atoms is

$$H = \int d\mathbf{r} \psi_\alpha^\dagger(\mathbf{r}) \frac{-\hbar^2 \nabla^2}{2m} \psi_\alpha(\mathbf{r}) + \frac{c_2}{2} \int d\mathbf{r} \hat{\mathbf{S}}^2(\mathbf{r}) + \frac{c_0}{2} \int d\mathbf{r} \hat{\rho}^2(\mathbf{r}). \quad (5.3)$$

Here $\psi_\alpha^\dagger(\psi_\alpha)$, $\alpha = x, y, z$ are creation (annihilation) operators for sodium atoms in hyperfine states $|\alpha\rangle$; they are defined as linear superpositions of creation operators for three spin-one states, $|1, m_F\rangle$, $m_F = 0, \pm 1$. $\psi_x^\dagger = (\psi_1^\dagger - \psi_{-1}^\dagger)/\sqrt{2}$, $\psi_y^\dagger = (\psi_1^\dagger + \psi_{-1}^\dagger)/i\sqrt{2}$ and $\psi_z^\dagger = \psi_0^\dagger$. $c_{0,2}$ are interaction parameters that depend on two-body s -wave scattering lengths $a_{0,2}$ for total spin 0,2: $c_0 = 4\pi\hbar^2(a_0 + 2a_2)/3m$ and $c_2 = 4\pi\hbar^2(a_2 - a_0)/3m$. For condensates of ^{23}Na atoms, $a_0 \simeq 50 a_B$ and $a_2 \simeq 55 a_B$ (a_B is the Bohr radius). $\hat{\mathbf{S}}_\alpha = -i\epsilon_{\alpha\beta\gamma} \Psi_\beta^* \Psi_\gamma$ and $\hat{\rho} = \psi_\alpha^\dagger \psi_\alpha$ are local spin-density and density operators (see Chap.2).

Let's first find out the mean field ground state of the system. Generally, a condensate wavefunction

$$\Psi_\alpha = \langle \psi_\alpha^\dagger \rangle \quad (5.4)$$

for spin-one atoms is a complex vector. For sodium atoms, interactions favor states with a zero spin density. This leads to a spin nematic ground state which does not break the time reversal symmetry and

$$\Psi = \exp(i\Phi) \sqrt{\rho} \mathbf{n}. \quad (5.5)$$

Here \mathbf{n} is a unit vector with three components n_α , and ρ is the number density of sodium atoms. This spin nematic state is invariant under an inversion of \mathbf{n} and a π -phase shift [123]

$$\mathbf{n} \rightarrow -\mathbf{n} \quad (5.6)$$

$$\Phi \rightarrow \Phi + \pi \quad (5.7)$$

The spinor condensate specified in Eq.5.5 is a spontaneously symmetry breaking state which breaks both the gauge symmetry and rotational symmetry. Although local spin densities $\langle \hat{\mathbf{S}}(\mathbf{r}) \rangle$ in a nematic state vanish, a nematic condensate carries a spin quadrupole moment defined as

$$Q_{\alpha\beta}(\mathbf{r}) = \langle \hat{\mathbf{S}}_\alpha \hat{\mathbf{S}}_\beta \rangle - \frac{1}{3} \delta_{\alpha\beta} \langle \hat{\mathbf{S}}^2 \rangle, \quad (5.8)$$

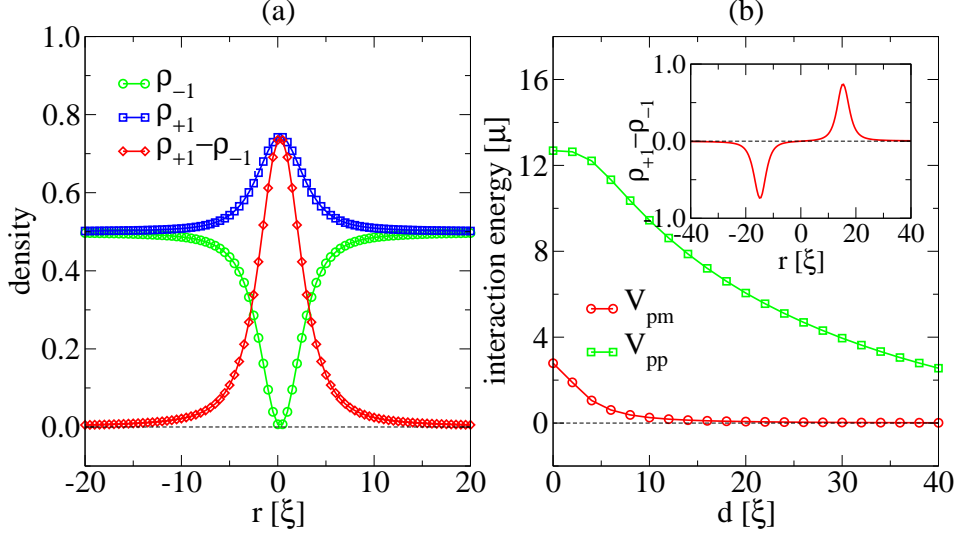


Figure 5.2: (color online). (a) Density ($\rho_{\pm 1} = |\psi_{\pm 1}|^2$) and spin-density ($\rho_+ - \rho_-$) profiles of an individual *plus* half-quantum vortex (HQV) centered at $r = 0$. (b) Interaction potentials (in units of chemical potential μ) between two HQVs as a function of separation distance d . V_{pm} is the potential between a *plus* HQV and a *minus* HQV; V_{pp} is the strong repulsive potential between two *plus* HQVs. Inset is for spin densities in a pair of *plus-minus* HQVs separated at $d = 30\xi$, ξ is the healing length.

which can be calculated and is specified by the nematic unit director \mathbf{n} introduced above:

$$Q_{\alpha\beta} = \rho \left(\mathbf{n}_\alpha \mathbf{n}_\beta - \frac{1}{3} \delta_{\alpha\beta} \right). \quad (5.9)$$

From the experimental point of view, the nematic spin vector has a special meaning that all the atoms in the condensate are in the $m'_F = 0$ level where m'_F is the spin projection along the \mathbf{n} axis.

After we examining the ground states, let's turn to the HQV. Without loss of generality, we assume that the HQV is centered at the origin and oriented along the z -direction, and nematic directors lying in a perpendicular $r - \theta$ plane rotate by 180° forming a spin-disclination. The corresponding condensate wavefunction far way from the vortex core is

$$\Psi(\theta, r \rightarrow \infty) = \exp\left(\frac{i\theta}{2}\right) \sqrt{\rho} \left(\cos \frac{\theta}{2}, \sin \frac{\theta}{2}, 0 \right). \quad (5.10)$$

5.2. HQV in Spinor Bose-Einstein Condensates

The 180° rotation of nematic director $\mathbf{n}(\theta) = (\cos \frac{\theta}{2}, \sin \frac{\theta}{2}, 0)$ around the vortex illustrates that a π -spin disclination where spin quadrupole moments $Q_{\alpha\beta}(\theta)$ slowly rotate is indeed confined to this HQV. In the Zeeman basis of $|1, m_F\rangle$ states, $m_F = 0, \pm 1$, the above vortex state is equivalent to

$$\psi_{+1} = \exp(i\theta)f(r)\sqrt{\frac{\rho}{2}}, \quad (5.11)$$

$$\psi_{-1} = -g(r)\sqrt{\frac{\rho}{2}}, \quad (5.12)$$

$$\psi_0 = 0. \quad (5.13)$$

When it is far away from the vortex core, $f(r \rightarrow \infty) = g(r \rightarrow \infty) = 1$.

The core structure can be studied by numerically solving the multiple-component Gross-Pitaevskii (GP) equation

$$\left[-\frac{\hbar^2}{2m}\nabla^2 + (c_0 + c_2)\rho_{\pm 1} + (c_0 - c_2)\rho_{\mp 1} \right] \psi_{\pm 1} = 0, \quad (5.14)$$

here $\rho_{m_F} = |\psi_{m_F}|^2$. The corresponding boundary conditions when $r \rightarrow \infty$ are set by the asymptotic behaviors of a HQV far away from the core as discussed before Eq.(5.14). Notice that the last term in Eq.(5.14) indicates that mutual interactions between $|1, \pm 1\rangle$ atoms induced by scattering are repulsive since $c_0 - c_2$ is positive.

The numerical solution of the above GP equation is presented in Fig.5.2(a). The results show that within the core, $|1, 1\rangle$ atoms state are completely depleted while $|1, -1\rangle$ atoms are not. This is because supercurrents are only present in $|1, 1\rangle$ component; in fact the density of $|1, -1\rangle$ atoms has an additional small bump at the center of core, to further take advantage of the depletion of $|1, 1\rangle$ atoms in the same region to minimize the overall repulsive interactions between $|1, \pm 1\rangle$ atoms. So the core has a nonzero local spin density $\langle \hat{\mathbf{S}}_z(\mathbf{r}) \rangle (= |\psi_1|^2 - |\psi_{-1}|^2)$ with excess atoms at $|1, -1\rangle$ state and we define it as a *minus* HQV. Similarly, one can construct a *plus* HQV with an identical vorticity (i.e. $\nabla \times \mathbf{v}_s$) but with excess $|1, 1\rangle$ atoms in its core (See Fig.5.2(a)). Generally, HQVs have distinct spatial magnetic structures: a HQV core carries excess spins while far away from the core spin quadrupole moments slowly rotate around the vortex.

Interactions between two HQVs very much depend on species of HQVs involved. When both are *plus* ones (or *minus*) as in Fig.5.1(c), the corresponding interaction potential $V_{pp(mm)}$ is a logarithmic long-range one due to interference between coherent supercurrents. However, the interaction between a *plus* and a *minus* HQV V_{pm} (as in Fig.5.1(d)) is repulsive and short

5.2. HQV in Spinor Bose-Einstein Condensates

ranged only extending over a scale of vortex cores. In this case, supercurrents flow in different components and they don't interfere; the short-range interaction is entirely due to inter-component interactions between $|1, 1\rangle$ and $|1, -1\rangle$ atoms. Indeed, the amplitude of potential V_{pm} is proportional to, when it is small, $c_0 - c_2$ which characterizes mutual interactions between $|1, \pm 1\rangle$ atoms. An integer vortex or a pair of *plus-minus* HQVs centered at a same point therefore is unstable and further fractionalizes into elementary HQVs. In Fig.5.2, we summarize results of an individual HQV and two HQVs.

It is also useful to describe the interaction between two HQVs in the language of nematic spin vectors \mathbf{n} and phase θ instead of Zeeman basis. The leading term of the interaction energy is mainly from the kinetic part E_{kin} which can be easily split into two parts when far away from the cores,

$$E_{kin} \simeq \int d\mathbf{r} \frac{\hbar^2}{2m} |\nabla\Psi|^2 \quad (5.15)$$

$$\simeq \int d\mathbf{r} \frac{\hbar^2\rho}{2m} (|\nabla\theta|^2 + |\nabla\mathbf{n}|^2). \quad (5.16)$$

The first term is the supercurrent's kinetic energy which also exists in the conventional quantum vortices. The second term is from spin gradient which is unique in spinor condensates. This formulation suggests that we can separate the spin part and the phase part when evaluating energies. The interaction energy from the phase part or the supercurrent has the same form of conventional vortices (see [68]):

$$\mathcal{C}_1\mathcal{C}_2 \frac{\pi\hbar^2 L_z \rho}{2m} \log \frac{R}{d}. \quad (5.17)$$

Here two vortices with circulation \mathcal{C}_1 and \mathcal{C}_2 are parallel to each other and L_z is the length of the system along the vortex line. And we also assume the separation d is much larger than the healing length ξ and much smaller than the system's radical size R . The interaction energy from the spin gradient term is much more complicated. However in the simple example shown above in which the spin vector \mathbf{n} is always pinned down in a plane, we can use the same formula by introducing the circulation number $\tilde{\mathcal{C}}_1$ and $\tilde{\mathcal{C}}_2$ for spin vectors. Therefore the interaction between two HQVs is

$$V_{int}(d) \simeq \frac{\pi\hbar^2 L_z \rho}{2m} \log \frac{R}{d} (\mathcal{C}_1\mathcal{C}_2 + \tilde{\mathcal{C}}_1\tilde{\mathcal{C}}_2). \quad (5.18)$$

For example, in Fig.5.1(c), we have $\mathcal{C}_1 = \mathcal{C}_2 = \tilde{\mathcal{C}}_1 = \tilde{\mathcal{C}}_2 = \frac{1}{2}$, leading to logarithmic repulsion between two HQVs. In Fig.5.1(d), we have $\mathcal{C}_1 = \mathcal{C}_2 =$

$\tilde{\mathcal{C}}_1 = -\tilde{\mathcal{C}}_2 = \frac{1}{2}$, leading to an cancelation of the logarithmic part. In this case the interaction between two HQVs are mainly coming from the contact of the core structures, therefore are short-ranged.

5.2.2 HQV Lattice in Rotating Traps

To dynamically create HQVs, we numerically solve the time-dependent coupled GP equations of spin-one BEC

$$\begin{aligned}
 (i - \gamma)\hbar\frac{\partial\psi_{\pm 1}}{\partial t} &= \left[-\frac{\hbar^2}{2m}\nabla^2 + V_{tr} - \mu \mp \lambda - \Omega L_z + c_0\rho\right. \\
 &\quad \left.+ c_2(\rho_{\pm 1} + \rho_0 - \rho_{\mp 1}) + W_{\pm}\right]\psi_{\pm 1} + c_2\psi_0^2\bar{\psi}_{\mp 1}, \\
 (i - \gamma)\hbar\frac{\partial\psi_0}{\partial t} &= \left[-\frac{\hbar^2}{2m}\nabla^2 + V_{tr} - \mu - \Omega L_z + c_0\rho\right. \\
 &\quad \left.+ c_2(\rho_1 + \rho_{-1})\right]\psi_0 + 2c_2\psi_1\psi_{-1}\bar{\psi}_0,
 \end{aligned} \tag{5.19}$$

where $\rho = \sum_{m_F} \rho_{m_F}$ is the total condensate density, $V_{tr}(\mathbf{r})$ is a spin-independent confining potential of an optical trap, and $W_{\pm}(\mathbf{r})$ are pulsed magnetic trapping potentials which we further apply in order to create HQVs. μ and λ are the Lagrange multipliers used to preserve the total number and magnetization of atoms respectively; γ is a phenomenological damping parameter which is necessary for studies of quasi-stationary states [166].

We restrict ourselves to a cigar-shaped potential with the aspect ratio $\lambda = \omega_{\perp}/\omega_z \sim 14$ which was also used in early experiments [50]. We consider a two-dimension cylindrical trap which is characterized by two dimensionless parameters $C_0 = \frac{8\pi N(a_0 + 2a_2)}{3L_z}$ and $C_2 = \frac{8\pi N(a_2 - a_0)}{3L_z}$, with L_z the size of system along the z -axis and $N = 3 \times 10^6$ the total number of sodium atoms. When combined with a nonaxisymmetric dipole potential that can be created using stirring laser beams [50, 51], the optical trapping potential in a *rotating frame* is given by $V_{tr}(\mathbf{r}) = m\omega_{\perp}^2\{(1+\epsilon)x^2 + (1-\epsilon)y^2\}/2$. Here $\omega_{\perp} = 2\pi \times 250$ Hz, and anisotropic parameter is set to be $\epsilon = 0.025$. We also include an additional magnetic trapping potential: $W_{\pm}(\mathbf{r}) = \mp\beta m\omega_{\perp}^2(x^2 + y^2)/2$, which could be realized in an Ioffe-Pritchard trap via a Zeeman splitting $m_F g_F \mu_B B$ with the Landé factor $g_F = -1$ for sodium atoms.

We start our numerical simulations with an initial state where $|1, \pm 1\rangle$ are equally populated. Experimentally, it was demonstrated that when the bias field is small and the gradient field along the z -axis of the trap is almost canceled, such a state can be prepared and the $|1, \pm 1\rangle$ components are completely miscible (however, with the immiscibility between $|1, \pm 1\rangle$ and $|1, 0\rangle$ components) [38]. We then study the time evolution of this initial

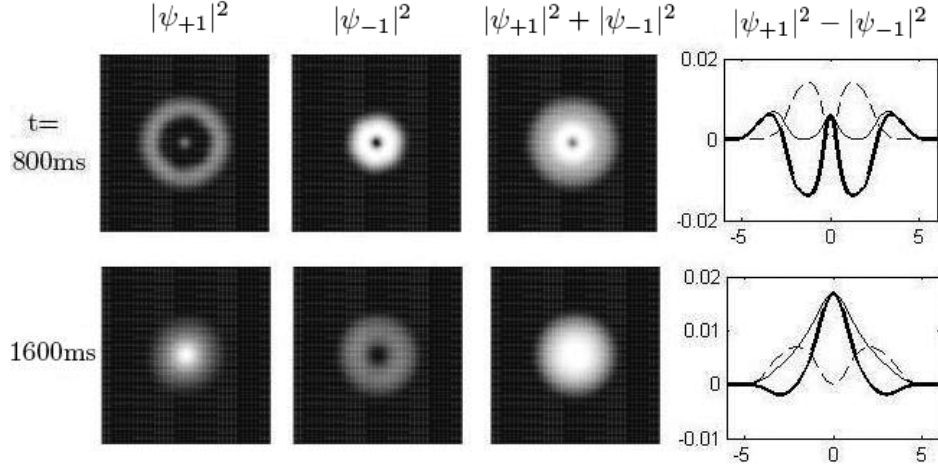


Figure 5.3: Creation of a half-quantum vortex. Density profiles of $|\psi_{+1}|^2$, $|\psi_{-1}|^2$, $|\psi_{+1}|^2 + |\psi_{-1}|^2$, and spin-density profile $|\psi_{+1}|^2 - |\psi_{-1}|^2$ (bold line) are shown. The rotating frequency is suddenly decreased from an initial value $\Omega = 0.65\omega_{\perp}$ to $\Omega = 0.3\omega_{\perp}$ at $t = 800$ ms. The bottom panel shows that a single half-quantum vortex is formed at $t = 1600$ ms after the magnetic trapping potential has been adiabatically switched off.

state using the Crank-Nicolson implicit scheme [166]. The unit of length is $a_h = \sqrt{\hbar/2m\omega_{\perp}} = 0.48 \mu\text{m}$ and the period of the trap is $\omega_{\perp}^{-1} = 4$ ms; the interaction parameters are $C_0 = 500$ and $C_2 = 450$ and the damping rate is $\gamma = 0.03$. Further, we include symmetry breaking effects in our simulations by allowing the trap center to randomly jump within a region $[-\delta, \delta] \times [-\delta, \delta]$ ($\delta = 0.001h$, where h is the grid size), which is crucial for vortices to enter the condensate one by one [168] rather than in opposing pairs [166, 167].

However, without additional pulsed magnetic potentials, our results indicate that dynamic instabilities for creation of integer vortices in rotating BECs occur almost at same frequencies as for HQVs and a triangular integer-vortex lattice is formed (see Fig.5.4(a)). This integer-vortex lattice is locally stable with respect to the non-magnetic perturbations, by applying an additional optical trapping potential with an oscillating trapping frequency to effectively *shake* them, indicating their metastability. For this reason, a time-dependent magnetic trapping potential with harmonic form is applied; and we find that when a pulsed magnetic field with $\beta > 0.005$ is applied, HQV lattices could be formed. Here we set $\beta = 0.1$, which is suitable for both generating a single HQV and demonstrating the dynamical evolution

of HQV lattices formation. After the magnetic trapping potentials are on, $|1, 1\rangle$ component further spreads to the edge, while $|1, -1\rangle$ component remains at the center of the trap and surfaces of equally populated $|1, \pm 1\rangle$ components become mismatched with two different Thomas-Fermi radii.

First, we dynamically create a single half-quantum vortex in condensates, which can be used for the study of dynamics of a HQV. We switch on abruptly a rotating drive with $\Omega = 0.65\omega_{\perp}$ and the trap anisotropy ϵ is increased rapidly from zero to its final value 0.025 in 20 ms. At $t = 800$ ms, only one vortex in $|1, -1\rangle$ component appears. Afterwards, We decrease Ω to $0.3\omega_{\perp}$ suddenly, and switch off the magnetic trapping potential adiabatically within 200 ms. We then find a stable single HQV formed at $t = 1600$ ms as shown in Fig.5.3. The $0.3\omega_{\perp}$ frequency used after $t = 1600$ ms is within the stable region estimated earlier [186] and our simulations of dynamics are consistent with the energetic analysis.

Fractionalized-vortex lattices can be created in a similar setup. The main experimental procedure and results of our simulations for creation of HQV lattices are presented in Fig.5.4. After a rotation with frequency $\Omega = 0.7\omega_{\perp}$ starts abruptly and anisotropy ϵ is set to its final value 0.025, we can see that the cloud is initially elongated and at the same time rotates with the trap. At about 150 ms, surface ripples due to quadrupole excitations occur in $|1, 1\rangle$ component of the condensate, while no surface oscillations appear on the surface of $|1, -1\rangle$ component. At $t = 240$ ms, we find that the density profile of $|1, 1\rangle$ component is along a short-axis while the $|1, -1\rangle$ component is along a long-axis due to repulsive interactions between two components, and the surface of $|1, -1\rangle$ component is not always buried in the inner region of $|1, 1\rangle$. The surfaces of two components oscillate independently and are decoupled dynamically. At $t = 430$ ms, we find that two *plus* HQVs with excess $|1, 1\rangle$ atoms inside cores have nucleated at the center. Correspondingly, we observe two small regions near the center where $|1, -1\rangle$ atoms are completely depleted and the density of $|1, 1\rangle$ atoms remains high. At $t = 800$ ms, two components are phase separated, but the structure of HQV cores remains almost unchanged. Finally, we switch off the additional magnetic potential adiabatically within 200 ms and a HQV lattice with interlaced square configuration becomes visible. In this structure, to minimize strong repulsive interactions $V_{pp(mm)}$ between *plus* or *minus* HQVs, the vorticity is evenly distributed among *plus* and *minus* HQVs, or between $|1, \pm 1\rangle$ components. This also indicates that spatially each *plus* HQV prefers to be adjacent to *minus* HQVs and *vice versa* to avoid stronger interactions V_{pp}, V_{mm} and to take advantage of relative weaker interactions V_{pm} (See Fig.5.2). To further minimize repulsive interactions V_{pm} between nearest neighboring vortices,

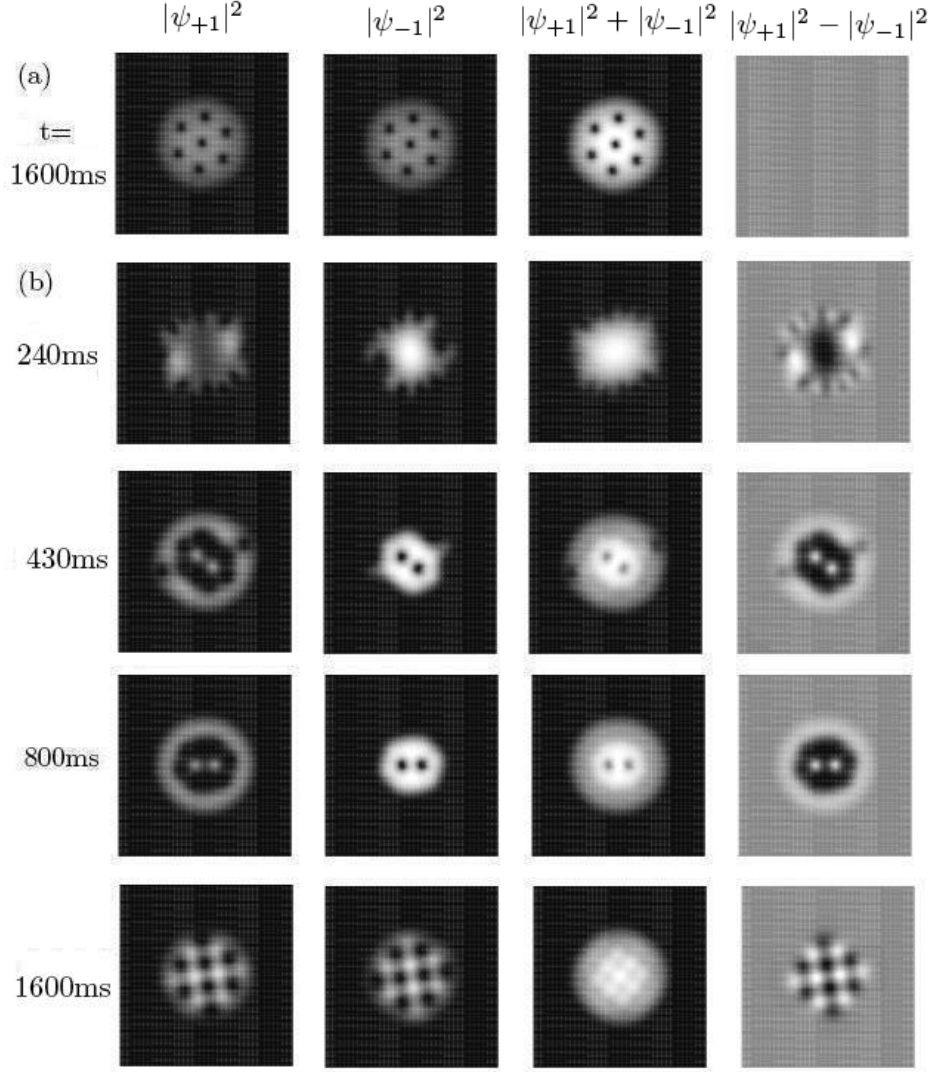


Figure 5.4: (a) Creation of a triangular integer-vortex lattice in a rotating optical trap at $t = 1600$ ms. (b) Creation of half-quantum vortex lattices when an additional pulsed magnetic trapping potential is applied. Here time evolution of various condensate densities is shown. The optical trap rotates at $\Omega = 0.7\omega_{\perp}$ with a magnetic trapping potential on until $t = 800$ ms; afterwards, the magnetic trap is adiabatically switched off within 200 ms. The bottom panel shows the half-quantum vortex lattice formation at $t = 1600$ ms; a square lattice in the spin-density profile is clearly visible.

a *plus* HQV is displaced away from adjacent *minus* HQVs by a maximal distance. Generally because of the asymmetry between V_{pp} and V_{pm} , a bipartite vortex lattice should be favored over frustrated geometries such as triangular lattices where a *plus* HQV could be adjacent to another *plus* HQV resulting in much stronger repulsion. In our simulations of ^{23}Na atoms in rotating traps with $c_0 \simeq 30c_2$, square vortex lattices have always been found. Equilibrium energetics of rectangular or square lattices were also considered in the quantum Hall regime [187, 188], in two-component BECs coupled by an external driving field where vortex molecules are formed [189], and also observed in condensates of pseudo-spin-1/2 rubidium atoms [190]. Here we have mainly focused on *dynamical creation* of HQV lattices confined to a spin-density-wave structure at relatively low frequencies; this structure can be conveniently probed by taking absorption images of ballistically expanding cold atoms in a Stern-Gerlach field [38].

5.3 HQV in 2D Superfluid of Ultracold $F = 1$ Atoms

In this section we will examine the fluctuation-driven vortex fractionalization and topological order in 2D nematic superfluids of cold sodium atoms. The Monte Carlo simulations suggest that a *softened* π -spin disclination be confined to a half-quantum vortex when spin correlations are short ranged. Both this result and direct calculations of winding-number operators indicate that a *non-local* topological spin order emerges simultaneously as cold atoms become a superfluid below a critical temperature. We have also obtained fluctuation-dependent critical frequencies for half-quantum vortex nucleation in rotating optical traps and discussed probing these excitations in experiments. In the following we will first introduce the system and Hamiltonian, and get an insight from a gauge field formulation, then we will present the results from numerical simulations and finally the nucleation of HQVs in rotations traps.

5.3.1 Effective Hamiltonian

We employ the Hamiltonian introduced previously for $F=1$ sodium atoms in optical lattices[129, 128],

$$\mathcal{H} = \sum_k \frac{b_L}{2} \hat{\rho}_k^2 + \frac{c_L}{2} \hat{S}_k^2$$

5.3. HQV in 2D Superfluid of Ultracold $F = 1$ Atoms

$$- t_L \sum_{\langle kl \rangle} (\psi_{k,\alpha}^\dagger \psi_{l,\alpha} + h.c.) - \sum_k \mu \hat{\rho}_k. \quad (5.20)$$

Here k is the lattice site index and $\langle kl \rangle$ are the nearest neighbor sites. μ is the chemical potential and t_L is the one-particle hopping amplitude. Two coupling constants are $b_L(c_L) = b(c) \frac{4\pi\hbar^2}{m} \int d\mathbf{r} (\phi_w^*(\mathbf{r})\phi_w(\mathbf{r}))^2$; b, c are effective s-wave scattering lengths, ϕ_w is the Wannier function for atoms in a periodic potential. Operators ψ_α^\dagger , $\alpha = x, y, z$ create hyperfine spin-one atoms in $\frac{1}{\sqrt{2}}(|1\rangle - |-1\rangle)$, $-i\frac{1}{\sqrt{2}}(|1\rangle + |-1\rangle)$ and $|0\rangle$ states respectively. The spin and number operators are defined as $\hat{S}_\alpha = -i\epsilon_{\alpha\beta\gamma}\psi_\beta^\dagger\psi_\gamma$, and $\hat{\rho} = \psi_\alpha^\dagger\psi_\alpha$. Spin correlations are mainly induced by interaction $c_L\hat{S}^2$. Minimization of this spin-dependent interaction requires that the order parameter $\Psi_\alpha (= \langle \psi_{k,\alpha}^\dagger \rangle)$ be a *real* vector up to a global phase, i.e. $\Psi = \sqrt{N}\mathbf{n} \exp(i\chi)$ where \mathbf{n} is a unit director on a two-sphere, $\exp(i\chi)$ represents a phase director and N is the number of atoms per site. All low energy degrees of freedom are characterized by configurations where \mathbf{n} and χ vary slowly in space and time[128]. Low lying collective modes include spin-wave excitations with energy dispersion $\omega(q) = v_s q$, $v_s = \sqrt{c_L t_L} a$ and phase-wave excitations with $\omega(q) = v_p q$, $v_p = \sqrt{b_L t_L} a$ (here a is the lattice constant). In one-dimensions, low energy *quantum* fluctuations destroy spin order leading to quantum spin disordered superfluids[123]. In two-dimensions, the amplitude of quantum spin fluctuations is of order of c_L/t_L and is negligible in shallow lattices as t_L is order-of-magnitude bigger than c_L . At finite temperatures, spin correlations are mainly driven by *long wave length* thermal fluctuations, analogous to quantum 1D cases. This aspect was also paid attention to previously and normal-superfluid transitions were investigated[191].

We therefore study the following Hamiltonian which effectively captures long wave length thermal fluctuations

$$H = -J \sum_{\langle kl \rangle} (\mathbf{n}_k \cdot \mathbf{n}_l) (\Phi_k \cdot \Phi_l); \quad (5.21)$$

here states at each site are specified by two unit directors: a nematic director, $\mathbf{n} = (\cos \phi_0 \sin \theta_0, \sin \phi_0 \sin \theta_0, \cos \theta_0)$ and a phase director, $\Phi = (\cos \chi, \sin \chi)$. $J = 2Nt_L$ is the effective coupling between two neighboring sites and depends on N , the number of atoms per site. The model is invariant under the following *local* Ising gauge transformation: $\mathbf{n}_i \rightarrow s_i \mathbf{n}_i$, $\Phi \rightarrow s_i \Phi_i$, and $s_i = \pm 1$. In the following, we present results of our simulations on 2D superfluids, especially spin structures, energetics of HQVs and nucleation of HQVs in rotating optical traps using the effective Hamiltonian in Eq.5.21.

5.3.2 HQV and Topological Order - A Gauge Field Description

In this section we are aiming at providing an intuitive and qualitative picture of the emergent degrees of freedom. And this can be done by introducing a Z_2 lattice gauge field model in which the *softened* spin disclination is represented by an excitation in the Z_2 gauge fields. The Z_2 lattice gauge model has also been introduced for spin singlet condensates in low dimensional optical lattices [128, 129], where the Z_2 gauge field is to represent that an even or odd number of spin singlets are formed between two neighbor sites. The quantitative analysis is carried out in the next section via a full monte carlo simulation of Eq.5.21 which supports the intuitive picture obtained in this section.

We start from the following classical Hamiltonian introduced in the last section:

$$H = -J \sum_{\langle ij \rangle} (\Phi_i \cdot \Phi_j)(\mathbf{n}_i \cdot \mathbf{n}_j) \quad (5.22)$$

Here Φ_i and Φ_j are phase vectors and their inner product is given by $\cos(\Phi_i - \Phi_j)$. \mathbf{n}_i is the nematic spin vector at site i . The summation runs over all the nearest neighbor sites $\langle ij \rangle$. J is a positive coupling constant which measures the strength of the phase and nematic vector twisting energy.

Let's first look at the continuum limit of the system where only fluctuations of long wavelengths are concerned. In this case we can treat \mathbf{n} and Ψ as a smoothed function of space coordinates:

$$\Phi_i \cdot \Phi_j \simeq 1 - \frac{a^2}{2} \frac{(\Phi_i - \Phi_j)^2}{a^2} \simeq 1 - \frac{a^2}{2} \left(\frac{\partial \Phi}{\partial x} \right)^2 \quad (5.23)$$

$$\mathbf{n}_i \cdot \mathbf{n}_j \simeq 1 - \frac{a^2}{2} \frac{(\mathbf{n}_i - \mathbf{n}_j)^2}{a^2} \simeq 1 - \frac{a^2}{2} \left(\frac{\partial \mathbf{n}}{\partial x} \right)^2 \quad (5.24)$$

The effective Hamiltonian in the continuum limit is (up to a constant)

$$H \simeq \int d^2x \left(\frac{J}{2} |\nabla \mathbf{n}|^2 + \frac{J}{2} |\nabla \Phi|^2 \right). \quad (5.25)$$

The above equation shows at large lengths scales, the spin vector and phase vectors are decoupled. It also shows that the spin vectors can be described by the O(3) non-linear sigma model and the phase vectors are described by the O(2) non-linear sigma model or XY model. According to renormalization

group method, in two-dimension space there is a quasi-long order in O(2) model and no long-range order in the O(3) model(see appendix). In other words, spin wave excitations open up an energy gap and they will not appear in our low energy effective theory.

Although the nonlinear sigma model captures the long-wavelength physics of spin and phase fluctuations, HQVs are missing in the continuum model in which spin and phase are decoupled. To obtain a low energy effective Hamiltonian which allows for HQV structures, we can introduce a gauge field by using the Hubbard-Stratonovich transformation[192]. We introduce a real-valued auxiliary gauge field σ_{ij} defined on bonds $\langle ij \rangle$ in the lattice. The effective Hamiltonian with the gauge field can be defined as [128]:

$$\begin{aligned}
 H(\sigma) = & \frac{J}{2} \sum_{\langle ij \rangle} \sigma_{ij}^2 + (\Phi_i \cdot \Phi_j)^2 + (\mathbf{n}_i \cdot \mathbf{n}_j)^2 \\
 & + J \sum_{\langle ij \rangle} \sigma_{ij} (\Phi_i \cdot \Phi_j) + \sigma_{ij} (\mathbf{n}_i \cdot \mathbf{n}_j)
 \end{aligned} \tag{5.26}$$

It can be shown that the gauge field Hamiltonian listed above is equivalent to the original one. In fact, an integration of the σ field in the new Hamiltonian will recover the original Hamiltonian as

$$e^{-\beta H} \sim \int D[\sigma] e^{-\beta H(\sigma)}. \tag{5.27}$$

The integration on the right hand side is performed straightforwardly by noticing that it can be decoupled to independent Gaussian integrals.

We can define a local gauge transformation associated with the Z_2 symmetry in the nematic representation. The Hamiltonian is invariant under the following transformation:

$$\mathbf{n}_i \rightarrow r_i \mathbf{n}_i \tag{5.28}$$

$$\Phi_i \rightarrow r_i \Phi_i, \tag{5.29}$$

$$\sigma_{ij} \rightarrow r_i r_j \sigma_{ij} \tag{5.30}$$

Here $r_i = \pm 1$.

An effective Hamiltonian \tilde{H} includes phase vectors and gauge fields can be obtained by integrating the spin degrees of freedom. Since an exact analytical expression is impossible in this case, let's estimate this integral using the molecule field approximation. Namely the correlation between n_i and n_j can be replaced by a vector coupled to a effective field which is the average of all the other nematic vectors in the system. We assume that

5.3. HQV in 2D Superfluid of Ultracold $F = 1$ Atoms

$\langle \mathbf{n}_i \rangle = x \mathbf{e}_z$, where $-1 \leq x \leq 1$. The correlation term can be approximated as:

$$\mathbf{n}_i \cdot \mathbf{n}_j = \langle \mathbf{n}_i \rangle \cdot \mathbf{n}_j + \langle \mathbf{n}_j \rangle \cdot \mathbf{n}_i - \langle \mathbf{n}_i \rangle \cdot \langle \mathbf{n}_j \rangle. \quad (5.31)$$

For simplicity let's first choose the gauge field to be $\sigma_{ij} = \sigma$. The Hamiltonian of the nematic spin fields is

$$H_n = \sum_i 2Jx^2 n_{i,z}^2 - 4J\sigma x n_{i,z} - Jx^4 - 2J\sigma x^2 \quad (5.32)$$

$$= \sum_i -n_{i,z} (4J\sigma x - 2Jx^2 n_{i,z}) - \dots \quad (5.33)$$

Here $(4J\sigma x - 2Jx^2 n_{i,z})$ plays a role of an effective field coupling to nematic spin vector. The value of x can be determined from the self consistent equation

$$\begin{aligned} x &= \langle n_{i,z} \rangle_T \\ &= \frac{\int dn_{i,z} n_{i,z} \exp [\beta J (4\sigma x - 2x^2 n_{i,z}) n_{i,z}]}{\int dn_{i,z} \exp [\beta J (4\sigma x - 2x^2 n_{i,z}) n_{i,z}]} \end{aligned} \quad (5.34)$$

Numerical solutions of the above self consistent equation are shown in Fig.5.5. There are two different phases in this system, and a phase transition occurs when we tune the parameter to across the boundary line. A ferromagnetic phase with $n_z \neq 0$ appears at low temperatures or for large σ values where the thermal fluctuations are too small to destroy the spin orders and the effective molecule field is large enough to hold the spin order; a paramagnetic phase appears in the opposite limit: high temperatures and low σ field. The phase transition line separated two phases is exactly given by the following:

$$\beta J_c \sigma = \frac{3}{4}. \quad (5.35)$$

After the integration of spin degrees of freedom the free energy of the system now is

$$F = \sum_{\langle ij \rangle} \frac{J}{2} (\Phi_i \cdot \Phi_j - \sigma)^2 + F_n(\beta J, \sigma) \quad (5.36)$$

$$F_n = \sum_i -T \ln \left(\int dn_{i,z} e^{-\beta H_n} \right) \quad (5.37)$$

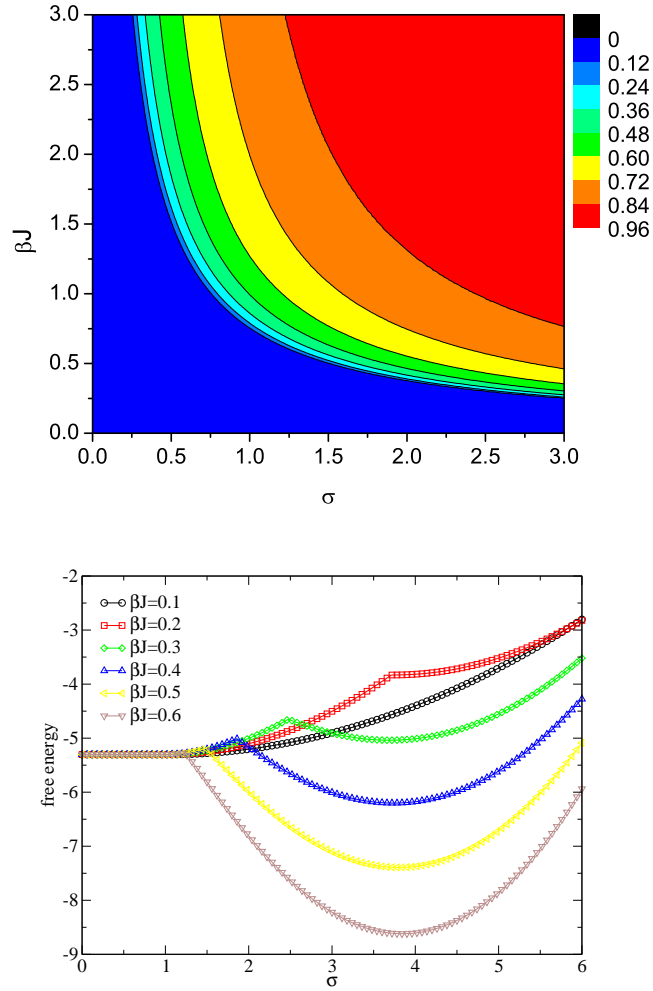


Figure 5.5: (a) Solution of the self consistent equation at different temperatures βJ and for gauge field of different strength σ . (b) Free energy as a function of σ at different temperatures.

5.3. HQV in 2D Superfluid of Ultracold $F = 1$ Atoms

Here F_n is the free energy due to the fluctuations of the spin vectors. Given βJ and σ , one first solve Eq.5.34 to get values of x , then H_n and F_n can be evaluated by the above equations, thus F_n is function of βJ and σ only. The overall free energy F as a function of βJ and σ can be obtained by minimizing with F with respect to $\Phi_i \cdot \Phi_j$ first with a given σ .

The resultant free energy as a function of σ at different temperatures is plotted in Fig. 5.5. The free energy's dependence on σ is very different at low temperatures and high temperatures. The average value of the sigma field $\langle \sigma \rangle$ determined from the local minimum of free energy can be nonzero at low temperatures. This result suggests that there is a nonzero coupling between the gauge field and phase vectors at low temperatures. In another words, it suggest a nonzero $\sigma_{ij}(\Phi_i \cdot \Phi_j)$ coupling term other the usual $(\Phi_i \cdot \Phi_j)^2$ phase correlation term in the low energy effective Hamiltonian \tilde{H} .

In the above heuristic argument we consider the uniform gauge field $\sigma_{ij} = \langle \sigma \rangle$ which we believe to describe be the low energy states. One may expect that a gauge field with $\sigma_{ij} = \pm \sigma$ is close to uniform gauge field in their free energy, since a gauge transformation can change the sign of σ_{ij} . In this case, the sign of the gauge field $s_{ij} = \frac{\sigma_{ij}}{\langle \sigma \rangle}$ appear to be relevant low energy degrees of freedom. One can obtain the effective Hamiltonian in terms of s_{ij} and Φ_i as [128]

$$\tilde{H} = - \sum_{\langle ij \rangle} \left[\tilde{J}_2 (\Phi_i \cdot \Phi_j)^2 + \tilde{J} s_{ij} (\Phi_i \cdot \Phi_j) \right] + \tilde{K} \sum_{\square} \prod_{ij \in \square} s_{ij}. \quad (5.38)$$

Here \tilde{J} , \tilde{J}_2 and \tilde{K} are renormalized coupling constants. The last term is the energy of pure gauge fields defined as the product of s_{ij} on four edges of a plaquette.

In the language of the gauge field model, a HQV can be viewed as a combination of a gauge defect and a π phase winding. In Fig.5.6 we plot the phase vectors and the gauge fields around a single HQV. A gauge defect located at the center is put in the center by setting $\sigma_{ij} = -1$ along the line from the vortex core to the system's boundary. The phase vectors on one side of the cut are anti-parallel to the ones on the other side, such a configuration won't raise too much energy. In fact, the energy cost of adding a HQV in this system is approximately

$$\pi \tilde{J}_2 d^2 \log \frac{R}{\xi_2} + \frac{\pi}{4} \tilde{J} d^2 \log \frac{R}{\xi} + \tilde{K}. \quad (5.39)$$

Here R is the system's size, d is the lattice constant, and ξ is the core size of the vortex. The \tilde{K} term is coming from the gauge defect located at the

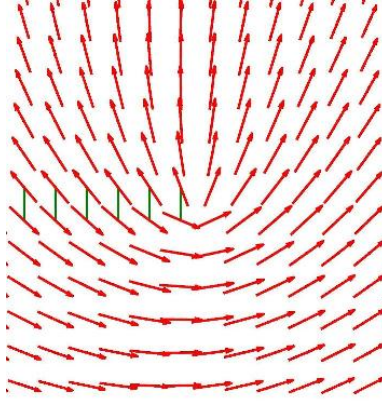


Figure 5.6: A HQV in the Z_2 lattice gauge model. Phase vectors Φ_i are plotted as red arrows. Gauge fields with $\sigma_{ij} = -1$ are marked in green lines and $\sigma_{ij} = 1$ are not marked.

center and is originating from the spin fluctuations in the original picture. Note that in the condensate case, energy cost of a HQV due to the spin vectors is also logarithmic function of the system size (Eq.5.16). The finite contribution of spin fluctuations in the 2D superfluids is consistent with short-ranged spin correlations.

The presence of gauge defects in a system can be characterized by the Wilson-loop variable W_C :

$$W_C = \prod_{\langle ij \rangle \in C} s_{ij}. \quad (5.40)$$

Here C is a closed loop and $\langle ij \rangle$ are edges on the loop. For a given gauge field, $W_C = 1$ if there is even numbers of gauge defects within the closed loop and $W_C = -1$ otherwise. The expectation value of the Wilson-loop variable is used to characterize the confinement or deconfinement of the gauge fields, namely according to whether the variable increases with the circumference of the loop (known as “perimeter law”), or with the area enclosed within the closed loop (known as “area law”). In the gauge field confinement phase, an individual gauge defect can not move freely in the system. The gauge defect is bounded to either another gauge defect or a phase defect. In the latter case, such a combination leads to a HQV. Previous studies on the effective gauge model Eq.5.38 [193] shows that there is indeed a gauge confinement phase when the temperature is not too high.

The above heuristic arguments illustrated the central idea in this sec-

tion: a HQV can be stabilized by a gauge defect in two-dimension spinor superfluid. Considering the gauge defect, a quantity defined globally (such as quantum circulation), is actually coming from short-ranged spin correlations, it implies there exists a nontrivial global order or topological order in spin correlations. In the next section, we will carry out a monte carlo simulation to quantitatively study HQV and the associated topological order.

5.3.3 HQV and Topological Order - Monte Carlo Simulations

An early analysis suggests that around a HQV, both phase and nematic directors rotate slowly by 180° [123]; in nematic coordinates (θ, ρ) , a HQV in condensates is represented by $\Psi(\theta, \rho) = \sqrt{N(\rho)} \exp(i\theta/2)\mathbf{n}(\theta)$, with $\mathbf{n} = (\cos(\theta/2), \sin(\theta/2), 0)$. The question here is whether, when nematic directors are not ordered, a spin disclination is still present in a HQV. To fully take into account $2D$ thermal fluctuations, we carry out Monte Carlo simulations on a square lattice of 128×128 sites and study spatial correlations between a HQV and a π -spin disclination, and topological order.

We first identify critical temperatures of the normal-superfluid phase transition by calculating correlations and the phase rigidity. The gauge-invariant quadrupole-quadrupole correlation functions we have studied are

$$f^{s,p}(\mathbf{r}_1, \mathbf{r}_2) = \langle Q_{\alpha\beta}^{s,p}(\mathbf{r}_1) Q_{\alpha\beta}^{s,p}(\mathbf{r}_2) \rangle. \quad (5.41)$$

Here $Q_{\alpha\beta}^s(\mathbf{r}_1) = \mathbf{n}_{1,\alpha}\mathbf{n}_{1,\beta} - (1/3)\delta_{\alpha\beta}$, $\alpha = x, y, z$; $Q_{\alpha\beta}^p(\mathbf{r}_1) = \Phi_{1,\alpha}\Phi_{1,\beta} - (1/2)\delta_{\alpha\beta}$, $\alpha = x, y$. In simulations, we have studied these correlation functions and found that the phase correlation length for $f^p(\mathbf{r}_1, \mathbf{r}_2)$ becomes divergent at a temperature $0.35J$ which is identified as a critical temperature T_c . We also calculate the phase rigidity or the renormalized phase coupling J_p

$$J_p = \frac{\partial^2 F}{\partial \delta\chi^2}; \quad (5.42)$$

here $\delta\chi$ is a small phase difference applied across the opposite boundaries of the lattice and F is the corresponding free energy. We indeed find that it approaches zero at T_c while at $T = 0$ J_p takes a bare value J . Meanwhile, the spin correlation function $f^s(\mathbf{r}_1, \mathbf{r}_2)$ remains to be short ranged across T_c . By extrapolating our data to lower temperatures, we find that the spin correlation length diverges only at $T = 0$ (see Fig.5.7a). Our simulations for

5.3. HQV in 2D Superfluid of Ultracold $F = 1$ Atoms

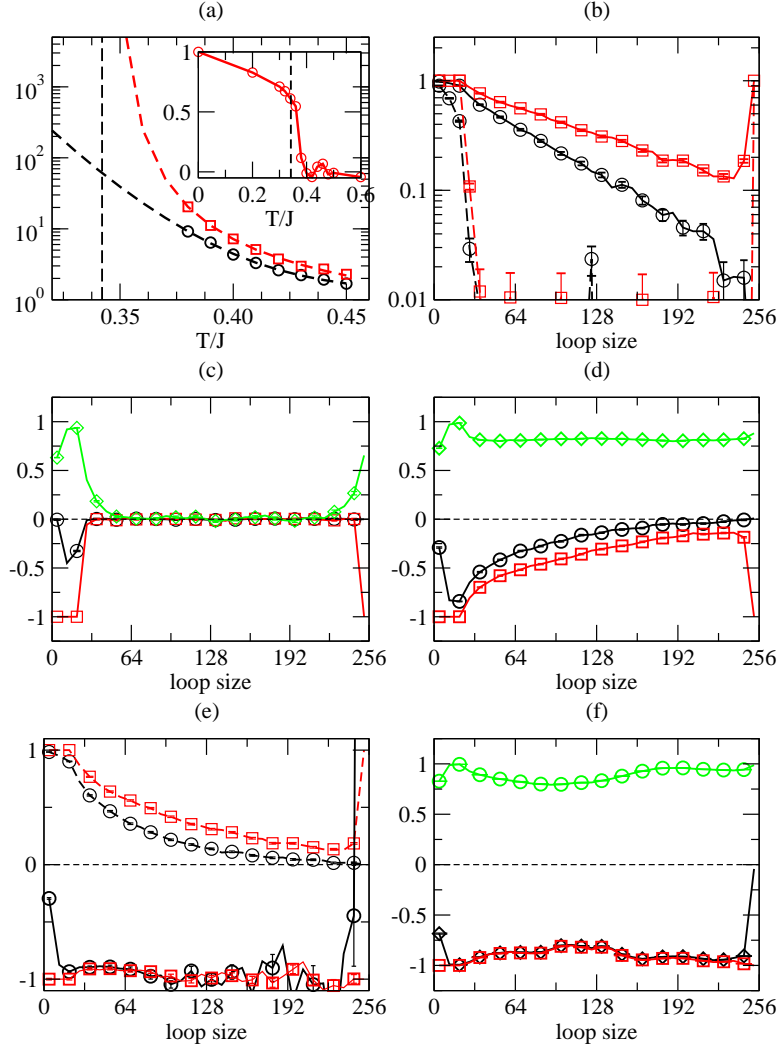


Figure 5.7: a) Spin(circle) and phase(square) correlation lengths versus temperatures; inset is for the renormalized phase coupling constant J_p (in units of J). Dashed lines are the fits to $\exp(A/\sqrt{T-T_c})$ for phase correlations with $T_c \approx 0.35J$ and $\exp(B/T)$ for spin correlations. b) Thermal average $\langle W_s \rangle$ (circle) and $\langle W_p \rangle$ (square) versus the loop perimeter at $T = 0.33J$ (solid line) and $T = 0.45J$ (dashed line). c)-f): $\langle W_{s,p} \rangle_{hv}$ and $\langle C \rangle_{hv}$ (diamond) averaged over configurations with half-vortex boundary conditions. c)-d), f) are for $T/J = 0.45, 0.33, 0.20$ respectively; in e), we also show $\langle W_{s,p} \rangle_{hv}$ normalized in terms of back ground values $\langle W_{s,p} \rangle_{bg}$ at $T = 0.33J$. The background values $\langle W_{s,p} \rangle_{bg}$ (dashed lines) are obtained by averaging over configurations with a uniform phase distribution at the boundary.

correlation lengths are consistent with the continuum limit of the model in Eq.5.22 which is equivalent to an XY model and an $O(3)$ nonlinear-sigma model.

In order to keep track of the winding of nematic directors in a wildly fluctuating back ground, we introduce the following gauge invariant π -rotation checking operator, which is essentially a product of sign-checking operators

$$\begin{aligned} W_s &= \prod_{\langle kl \rangle \in \mathcal{C}} \text{sign}(\mathbf{n}_k \cdot \mathbf{n}_l), \\ W_p &= \prod_{\langle kl \rangle \in \mathcal{C}} \text{sign}(\Phi_k - \Phi_l). \end{aligned} \quad (5.43)$$

Here the product is carried out along a closed square-shape path \mathcal{C} centered at the origin of a $2D$ lattice. $W_{s,p}$ can be either $+1$ or -1 ; and $W_{s(p)}$ is minus one when \mathcal{C} encloses a π -spin disclination (HQV). The gauge invariant circulation of supercurrent velocity (in units of $\pi\hbar/m$) is defined as

$$C = \frac{1}{\pi} \sum_{\langle kl \rangle \in \mathcal{C}} \text{sign}(\mathbf{n}_k \cdot \mathbf{n}_l) \sin(\Phi_k - \Phi_l). \quad (5.44)$$

This quantity is equal to one in a HQV.

In our simulations, we investigate the winding number $\langle W_{s,p} \rangle_{hv}$ averaged over configurations where phase directors rotate by 180° around the boundary of the lattice and the center plaquette. At temperatures above the normal-superfluid transition temperature T_c , both winding numbers $W_{s,p}$ and circulation C are averaged to zero within our numerical accuracy (see Fig.5.7). And our choice of boundary conditions does not lead to a vortex or disclination configuration in the absence of phase rigidity. Below T_c , the circulation C is averaged to one indicating that the boundary conditions effectively project out HQV configurations. Meanwhile, we observe loop-perimeter dependent $\langle W_{s,p} \rangle_{hv}$ which can be attributed to the background fluctuations of HQV or disclination pairs. The loop-perimeter dependence of $\langle W_{s,p} \rangle_{hv}$ here is almost identical to that for uniform boundary conditions, i.e. the back ground value. After normalizing $\langle W_{s,p} \rangle_{hv}$ in terms of background winding numbers $\langle W_{s,p} \rangle_{bg}$, we find both $\frac{\langle W_s \rangle_{hv}}{\langle W_s \rangle_{bg}}$ and $\frac{\langle W_p \rangle_{hv}}{\langle W_p \rangle_{bg}}$ approach -1 (see Fig.5.7). We thus demonstrate that a softened disclination is spatially correlated with a HQV. At the temperatures we carry out these simulations the spin correlation length is sufficiently short compared to the size of the lattice. At further lower temperatures, the spin correlation length becomes longer than the lattice size and fluctuations of pairs of disclination-

anti-disclination are strongly suppressed; $\langle W_{s,p} \rangle_{hv}$ are equal to -1 for almost all loops, which corresponds to a mean field result.

Results in Fig.5.7 indicate that a HQV is confined to a softened spin disclination and *vice versa* to form a fundamental excitation. Thus, π -disclinations like HQVs have logarithmically divergent energies and are fully suppressed in ground states. Our results also illustrate that although the average local spin quadrupole moments $Q_{\alpha\beta}^s$ vanish because of strong fluctuations, an overall π -rotation of nematic directors in disclinations is still conserved because of a coupling to the superfluid component. This coupling between a HQV and disclination can also be attributed[137] to a coupling between Higgs matter and discrete gauge fields[194]. Furthermore, the absence of unbound π -disclinations in superfluids indicates a topological order, similar to the one introduced previously for an isotropic phase of liquid crystal[193]. Consequently, once a conventional phase order appears below a critical temperature, a topological spin order simultaneously emerges while spin correlations remain short ranged.

The emergent topological order can be further verified by examining the average of product-operator $W_{s,p}$ over all configurations (with open boundaries). Above the normal-superfluid transition temperature T_c , we again find that $W_{s,p}$ both are averaged to zero within our numerical accuracy implying proliferation of unbound HQVs or disclinations. Below T_c , we study the loop-perimeter dependence of average winding numbers $\langle W_{s,p} \rangle$ and find that both $\ln\langle W_p \rangle$ and $\ln\langle W_s \rangle$ are linear functions of loop-perimeter analogous to the Wilson-loop-product of deconfining gauge fields[195]; if there were unbound disclinations, one should expect that $\ln\langle W_p \rangle$ is proportional to, instead of the loop-perimeter, the loop-area which represents the number of unbound disclinations enclosed by the loop.

5.3.4 Critical Frequency for HQV Nucleation

Let us now turn to the nucleation of those excitations in rotating traps[50]. To understand the critical frequency for nucleation, we study the free energy of a vortex, in a rotating frame, as a function of the distance r from the axis of a cylindrical optical trap (the axis is along the z -direction),

$$F_{h.v.}(r) = F_{h.v.}^0(r) - \Omega L_z(r). \quad (5.45)$$

Here $F_{h.v.}^0(r)$ is the free energy of a HQV located at distance r from the trap axis in the absence of rotation, $L_z(r)$ is the angular momentum of the vortex state and Ω is the rotating frequency. In a 2D lattice without a trapping

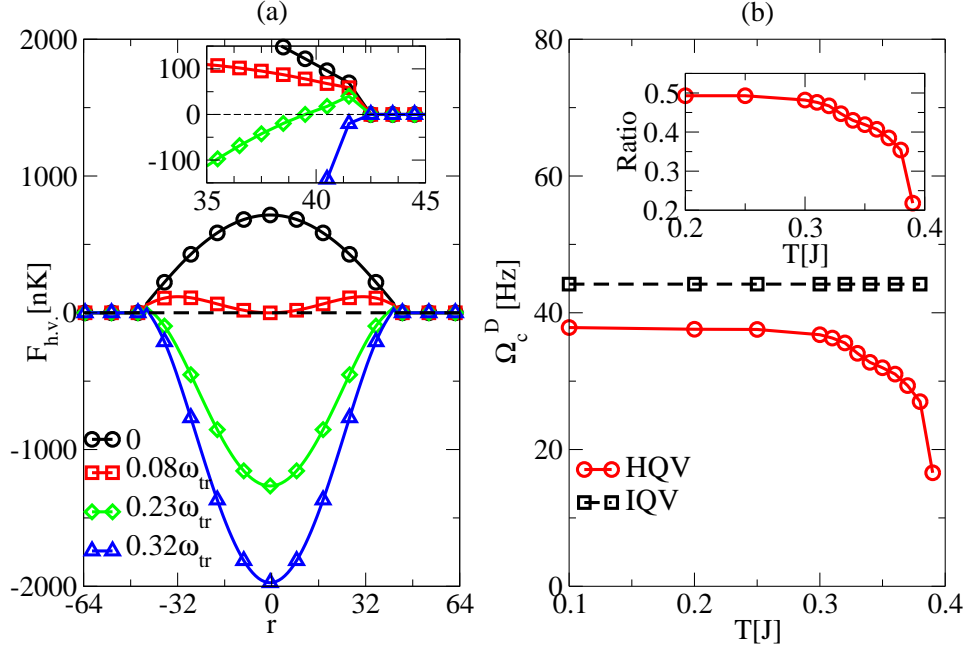


Figure 5.8: a) The free energy of a HQV at a distance r from the trap center at rotation frequencies 0, 0.08, 0.23 and 0.32 (in units of trap frequency $\omega_{tr} = 120\text{Hz}$) at $T = 0.33J$. Details near the edge are shown in the inset. At the center, the exchange coupling is $J = 154nk$. b) The critical frequency Ω_c^D (solid line) varies from $0.32\omega_{tr}$ (or 38Hz) to $0.17\omega_{tr}$ (or 20Hz) as the temperature T increases. As a reference, we also show Ω_c^D versus T for integer quantum vortices (dashed line). Inset is the temperature-dependence of the ratio between the HQV energy $F_{h.v.}^0$ and the IQV energy F_v^0 .

potential, the energy of a HQV is $F_{h.v.}^0 = (\pi J_p/4 + \pi J_s/4) \ln(L/a)$, with contributions from phase winding and spin twisting; here $J_{p,s}$ are renormalized phase and spin coupling respectively and L is the size of system. For an integer-quantum vortex (IQV), the energy is $F_v^0 = \pi J_p \ln(L/a)$. The ratio between $F_{h.v.}^0$ and F_v^0 depends on the ratio J_s/J_p or spin fluctuations; in the limit L approaches infinity, the ratio $F_{h.v.}^0/F_v^0$ changes discontinuously from $1/2$ at $T = 0$ where $J_p \approx J_s = J$ to $1/4$ at finite low temperatures in $2D$ where J_s vanishes. In simulations of a finite trap (see below), because of a finite size effect we find that this ratio varies from $1/2$ to $1/4$ smoothly as temperatures increase from 0 to T_c .

To study nucleation of half-quantum vortices in an optical trap, we as-

5.3. HQV in 2D Superfluid of Ultracold $F = 1$ Atoms

sume a nearly harmonic trapping potential $V(r) = 1/2m\omega_{tr}^2 r^2$, with ω_{tr} being the trap frequency. The average number of particles per site $N(r)$ has a Thomas-Fermi profile; $N(r) = N_0(1 - r^2/R_{TF}^2)$, here N_0 is the number density at the center and R_{TF} is the Thomas-Fermi radius. Furthermore, the optical lattice potential along the axial direction is sufficiently deep so that atoms are confined in a two-dimension xy plane; the in-plane lattice potential depth is set to be $5E_R$ (E_R is the photon recoil energy) and $t_L = 77nk$, $b_L = 187nk$ and $c_L = 10nk$. For $N_0 = 1.2$ and trap frequency $\omega_{tr} = 120Hz$, we find that $R_{TF} = 43a$ and $L_{h.o.} = 4a$ where $L_{h.o.} (= 1/\sqrt{2m\omega_{tr}})$ is the harmonic oscillator length. The coupling J_{kl} depends on the distance from the center of trap and at the center, the coupling is about $154nk$. In non-rotating or slowly rotating traps, the free energy maximum is located at the center and there should be no vortices in the trap. As frequencies are increased, a local energy minimum appears at the center and becomes degenerate with the no-vortex state at a thermodynamic critical frequency (which is about $0.08\omega_{tr}$ at $T = 0.33J$); however because of a large energy barrier separating the two degenerate states as shown in Fig.5.8, vortices are still prohibited from entering the trap.

Further speeding up rotations results in an energetically lower and spatially narrower barrier. Within the range of temperatures studied, thermal activation turns out to be insignificant within an experimental time scale ($\sim 100ms$) because of low attempt frequencies. So only when the spatial width of barrier becomes comparable to a hydrodynamic breakdown length[196], the barrier can no longer be felt and vortices start to penetrate into the trap. The hydrodynamic breakdown length L_B is about $(L_{h.o.}^4/2R_{TF})^{1/3}$, which in our case turns out to be about $2a$ (a is the lattice constant). We use this criterion to numerically determine the dynamical critical frequency for vortex nucleation Ω_c^D ; for IQVs, the estimated Ω_c^D is a flat function of T (see Fig.5.8b) which is qualitatively consistent with earlier estimates[197, 198]. For HQVs, however, as $F_{h.v.}^0$ depends on the amplitude of spin fluctuations, Ω_c^D varies from about $0.32\omega_{tr}$ at $T = 0$ where $J_s \approx J_p$ due to a finite size effect, to about $0.17\omega_{tr}$ at temperatures close to T_c where $J_s \approx 0$. Note when J_s approaches zero as in the thermodynamic limit, Ω_c^D ($\sim 0.17\omega_{tr}$) for HQVs is about one-half of the critical frequency for IQVs (about $0.37\omega_{tr}$ for the trap studied here).

The interaction between two HQVs with the same vorticity at a separation distance d contains two parts. One, $V_{cc}(> 0)$ is from interactions between two supercurrent velocity fields which is logarithmic as a function of d ; and the other, V_{ss} is from interaction between two spin twisting fields accompanying HQVs. For a disclination-anti disclination pair, in the dilute

limit one finds that $V_{cc} \sim -V_{ss}$ resulting in a cancelation of long-range interactions. The resultant short-range repulsions lead to square vortex lattices found in numerical simulations[199]. For fluctuation-driven fractionalized vortices, V_{ss} is almost zero and the overall interactions are always logarithmically repulsive. HQVs nucleated in a rotating trap should therefore form a usual triangular vortex lattice.

Individual vortex lines can be probed either by studying a precession of eigenaxes of surface quadrupole mode in rotating superfluids[200, 201, 202]. In the later approach, one studies the angular momentum carried per particle in a HQV state. When a HQV is nucleated in the trap, superfluids are no longer irrotational and the angular momentum per particle is $\hbar/2$ rather than \hbar per particle for an integer vortex state. When a surface quadrupole oscillation across a rotating superfluid is excited, larger axes of quadrupole oscillation start to precess just as in the case of integer vortices. However, the precession rate is only one half of the value for an integer vortex state which can be studied in experiments.

5.4 Conclusion

In conclusion, 2D superfluids of sodium atoms can have a non-local topological spin order associated with half quantum vortices. In rotating traps, fluctuation-driven fractionalized vortices can nucleate at a critical frequency which is about half of that for integer vortices. In the future, it is interesting to explore 2D-3D dimension transition that can be realized in optical lattices. When a superfluid of cold atoms in a 3D lattice is gradually separated into independent layers of 2D superfluids, possible phase transitions accompanied by the emergence of the topological order may occur. It is also expected that across this phase transition there is interesting vortex lattice transition connecting square lattices in 3D condensates and triangular lattices in 2D superfluids.

Chapter 6

Conclusion

In conclusion, we have studied fluctuation-driven phenomena in spinor superfluids of ultracold systems. We have shown that fluctuations in spinor systems of ultracold atoms studied in the thesis have completely changed the picture suggested by mean field analysis and have given rise to several novel fluctuation-driven phenomena.

In hyperfine $F = 2$ nematic condensates, quantum fluctuations can change the mean field prediction in magnetic correlations and spin dynamics dramatically. It is shown that zero-point quantum fluctuations completely lift the accidental continuous degeneracy that is found in mean field analysis of quantum spin nematic phases of hyperfine spin-two cold atoms. Two distinct spin nematic states with higher symmetries are selected by quantum fluctuations. In ultracold experiments, it is possible to probe quantum fluctuations directly via studying coherent spin dynamics of ultracold atoms in optical lattices. We have carried out a detailed study of fluctuation-driven spin dynamics. Unlike the mean field coherent dynamics, quantum fluctuation-controlled spin dynamics are very sensitive to the variation of quantum fluctuations. They have peculiar dependence of Zeeman fields and potential depths in optical lattices. In particular this novel type of spin coherent dynamics can be potentially explored under accessible experimental conditions. Our results not only point out the fundamental limitations of previous measurement based on mean field coherent dynamics, but also provide a new type of tool to investigate fluctuation-driven phenomena. In the future, it would be interesting to use fluctuation-driven dynamics to investigate correlated fluctuations and various universal scaling properties near quantum critical points.

In another spinor system, 2D nematic superfluids of cold sodium atoms, spin structures of fluctuation-driven fractionalized vortices and topological spin order are studied. Monte Carlo simulations suggest a softened π -spin disclination structure in a half quantum vortex when spin correlations are short ranged; in addition, calculations indicate that a unique non-local topological spin order emerges simultaneously as cold atoms become a superfluid below a critical temperature. We have also proposed an experimental study

of half quantum vortices in rotating optical traps where the critical frequencies for vortex nucleation are fluctuation dependent. In the future, it would be interesting to explore 2D-3D dimension transition that can be realized in optical lattices. Interesting phase transitions should occur when a superfluid of cold atoms in a 3D lattice is gradually separated into independent layers of 2D superfluids.

Bibliography

- [1] Landau, L. D. and Lifshitz, L. M. *Quantum Mechanics Non-Relativistic Theory*. Butterworth-Heinemann, 3 edition, January (1981).
- [2] Einstein, A., Podolsky, B., and Rosen, N. *Physical Review Online Archive (Prola)* **47**(10), 777–780 May (1935).
- [3] *The Born-Einstein Letters*. Walker & Company, (1971).
- [4] Mazo, R. M. *Brownian Motion: Flucuations, Dynamics, and Applications*. Oxford University Press, USA, April (2002).
- [5] Casimir, H. B. G. and Polder, D. *Physical Review Online Archive (Prola)* **73**(4), 360–372 Feb (1948).
- [6] Einstein, A. and Stern, O. *Annalen der Physik* **40**(3) March (1913).
- [7] Lamb, W. E. and Retherford, R. C. *Physical Review Online Archive (Prola)* **72**(3), 241–243 Aug (1947).
- [8] Peskin, M. E. and Schroeder, D. V. *An introduction to quantum field theory*. Addison-Wesley Pub. Co, (1996).
- [9] Klimchitskaya, G. L., Mohideen, U., and Mostepanenko, V. M. *Reviews of Modern Physics* **81**(4), 1827–1885 Dec (2009).
- [10] Obrecht, J. M., Wild, R. J., Antezza, M., Pitaevskii, L. P., Stringari, S., and Cornell, E. A. *Physical Review Letters* **98**(6), 063201 Feb (2007).
- [11] Coleman, S. and Weinberg, E. *Physical Review D* **7**(6), 1888–1910 Mar (1973).
- [12] Villain, J., Bidaux, R., Carton, J. P., and Conte, R. *Journal de Physique* **41**(11) (1980).
- [13] Shender, E. F. *Soviet Physics - JETP* **56**(1), 178–184 (1982).

Bibliography

- [14] Henley, C. L. *Physical Review Letters* **62**(17), 2056–2059 Apr (1989).
- [15] Shender, E. F. and Holdsworth, P. C. W. *Fluctuations and Order: The New Synthesis*. Springer-Verlag, Berlin, 1 edition, March (1996).
- [16] Mermin, N. D. and Wagner, H. *Physical Review Letters* **17**(22), 1133–1136 Nov (1966).
- [17] Hohenberg, P. C. *Physical Review Online Archive (Prola)* **158**(2), 383–386 Jun (1967).
- [18] Einstein, A. *Annalen der Physik* **17**(8) (1905).
- [19] Anderson, M. H., Ensher, J. R., Matthews, M. R., Wieman, C. E., and Cornell, E. A. *Science* **269**(5221), 198–201 July (1995).
- [20] Bradley, C. C., Sackett, C. A., Tollett, J. J., and Hulet, R. G. *Physical Review Letters* **75**(9), 1687–1690 Aug (1995).
- [21] Davis, K. B., Mewes, M. O., Andrews, M. R., van Druten, N. J., Durfee, D. S., Kurn, D. M., and Ketterle, W. *Physical Review Letters* **75**(22), 3969–3973 Nov (1995).
- [22] Griffin, A., Snoke, D. W., and Stringari, S., editors. *Bose-Einstein Condensation*. Cambridge University Press, July (1996).
- [23] Fried, D. G., Killian, T. C., Willmann, L., Landhuis, D., Moss, S. C., Kleppner, D., and Greytak, T. J. *Physical Review Letters* **81**(18), 3811–3814 Nov (1998).
- [24] Robert, A., Sirjean, O., Browaeys, A., Poupard, J., Nowak, S., Boiron, D., Westbrook, C. I., and Aspect, A. *Science* **292**(5516), 461–464 April (2001).
- [25] Modugno, G., Ferrari, G., Roati, G., Brecha, R. J., Simoni, A., and Inguscio, M. *Science* **294**(5545), 1320–1322 November (2001).
- [26] Griesmaier, A., Werner, J., Hensler, S., Stuhler, J., and Pfau, T. *Physical Review Letters* **94**(16), 160401 Apr (2005).
- [27] Stellmer, S., Tey, M. K., Huang, B., Grimm, R., and Schreck, F. *Physical Review Letters* **103**(20), 200401 Nov (2009).
- [28] Courteille, P., Freeland, R., Heinzen, D., van Abeelen, F., and Verhaar, B. *Physical Review Letters* **81**(1), 69–72 Jul (1998).

Bibliography

- [29] Roberts, J. L., Claussen, N. R., Burke, J. P., Greene, C. H., Cornell, E. A., and Wieman, C. E. *Physical Review Letters* **81**(23), 5109–5112 Dec (1998).
- [30] Weber, T., Herbig, J., Mark, M., Nagerl, H.-C., and Grimm, R. *Science* **299**(5604), 232–235 January (2003).
- [31] DeMarco, B. and Jin, D. S. *Science* **285**(5434), 1703–1706 September (1999).
- [32] Roati, G., Riboli, F., Modugno, G., and Inguscio, M. *Physical Review Letters* **89**(15), 150403 Sep (2002).
- [33] Truscott, A. G., Strecker, K. E., McAlexander, W. I., Partridge, G. B., and Hulet, R. G. *Science* **291**(5513), 2570–2572 March (2001).
- [34] Schreck, F., Khaykovich, L., Corwin, K. L., Ferrari, G., Bourdel, T., Cubizolles, J., and Salomon, C. *Physical Review Letters* **87**(8), 080403 Aug (2001).
- [35] Hadzibabic, Z., Stan, C. A., Dieckmann, K., Gupta, S., Zwierlein, M. W., Görlitz, A., and Ketterle, W. *Physical Review Letters* **88**(16), 160401 Apr (2002).
- [36] Stamper-Kurn, D. M., Andrews, M. R., Chikkatur, A. P., Inouye, S., Miesner, H. J., Stenger, J., and Ketterle, W. *Physical Review Letters* **80**(10), 2027–2030 Mar (1998).
- [37] Görlitz, A., Gustavson, T. L., Leanhardt, A. E., Löw, R., Chikkatur, A. P., Gupta, S., Inouye, S., Pritchard, D. E., and Ketterle, W. *Physical Review Letters* **90**(9), 090401 Mar (2003).
- [38] Stenger, J., Inouye, S., Stamper-Kurn, D. M., Miesner, H. J., Chikkatur, A. P., and Ketterle, W. *Nature* **396**(6709), 345–348 November (1998).
- [39] Schmaljohann, H., Erhard, M., Kronjäger, J., Kottke, M., van Staa, S., Cacciapuoti, L., Arlt, J. J., Bongs, K., and Sengstock, K. *Physical Review Letters* **92**(4), 040402 Jan (2004).
- [40] Myatt, C. J., Burt, E. A., Ghrist, R. W., Cornell, E. A., and Wieman, C. E. *Physical Review Letters* **78**(4), 586–589 (1997).
- [41] Granade, S. R., Gehm, M. E., O’Hara, K. M., and Thomas, J. E. *Physical Review Letters* **88**(12), 120405 Mar (2002).

Bibliography

- [42] Köhler, T., Góral, K., and Julienne, P. S. *Reviews of Modern Physics* **78**(4), 1311–1361 Dec (2006).
- [43] Pupillo, G., Micheli, A., Büchler, H. P., and Zoller, P. In *Cold molecules: Creation and applications*, Krems, R., Friedrich, B., and Stwalley, W. C., editors. CRC Press, Taylor & Francis Group June (2009).
- [44] Jin, D. S., Ensher, J. R., Matthews, M. R., Wieman, C. E., and Cornell, E. A. *Physical Review Letters* **77**(3), 420–423 Jul (1996).
- [45] Mewes, M. O., Andrews, M. R., van Druten, N. J., Kurn, D. M., Durfee, D. S., Townsend, C. G., and Ketterle, W. *Physical Review Letters* **77**(6), 988–991 Aug (1996).
- [46] Vogels, J. M., Xu, K., Raman, C., Shaeer, J. R. A., and Ketterle, W. *Physical Review Letters* **88**(6), 060402+ Jan (2002).
- [47] Cataliotti, F. S., Burger, S., Fort, C., Maddaloni, P., Minardi, F., Trombettoni, A., Smerzi, A., and Inguscio, M. *Science* **293**(5531), 843–846 August (2001).
- [48] Albiez, M., Gati, R., Fölling, J., Hunsmann, S., Cristiani, M., and Oberthaler, M. K. *Physical Review Letters* **95**(1), 010402 Jun (2005).
- [49] Matthews, M. R., Anderson, B. P., Haljan, P. C., Hall, D. S., Wieman, C. E., and Cornell, E. A. *Physical Review Letters* **83**(13), 2498–2501 Sep (1999).
- [50] Madison, K. W., Chevy, F., Wohlleben, W., and Dalibard, J. *Physical Review Letters* **84**(5), 806–809 Jan (2000).
- [51] Abo-Shaeer, J. R., Raman, C., Vogels, J. M., and Ketterle, W. *Science* **292**(5516), 476–479 April (2001).
- [52] Andrews, M. R., Townsend, C. G., Miesner, H. J., Durfee, D. S., Kurn, D. M., and Ketterle, W. *Science* **275**(5300), 637–641 January (1997).
- [53] Mewes, M. O., Andrews, M. R., Kurn, D. M., Durfee, D. S., Townsend, C. G., and Ketterle, W. *Physical Review Letters* **78**(4), 582–585 Jan (1997).
- [54] Anderson, B. P. and Kasevich, M. A. *Science* **282**(5394), 1686–1689 November (1998).

Bibliography

- [55] Bloch, I., Hänsch, T. W., and Esslinger, T. *Physical Review Letters* **82**(15), 3008–3011 Apr (1999).
- [56] Hagley, E. W., Deng, L., Kozuma, M., Wen, J., Helmerson, K., Rolston, S. L., and Phillips, W. D. *Science* **283**(5408), 1706–1709 March (1999).
- [57] Deng, L., Hagley, E. W., Wen, J., Trippenbach, M., Band, Y., Julienne, P. S., Simsarian, J. E., Helmerson, K., Rolston, S. L., and Phillips, W. D. *Nature* **398**(6724), 218–220 March (1999).
- [58] Chang, M. S., Hamley, C. D., Barrett, M. D., Sauer, J. A., Fortier, K. M., Zhang, W., You, L., and Chapman, M. S. *Physical Review Letters* **92**(14), 140403 Apr (2004).
- [59] Burger, S., Bongs, K., Dettmer, S., Ertmer, W., Sengstock, K., Sanpera, A., Shlyapnikov, G. V., and Lewenstein, M. *Physical Review Letters* **83**(25), 5198–5201 Dec (1999).
- [60] Denschlag, J., Simsarian, J. E., Feder, D. L., Clark, C. W., Collins, L. A., Cubizolles, J., Deng, L., Hagley, E. W., Helmerson, K., Reinhardt, W. P., Rolston, S. L., Schneider, B. I., and Phillips, W. D. *Science* **287**(5450), 97–101 January (2000).
- [61] Khaykovich, L., Schreck, F., Ferrari, G., Bourdel, T., Cubizolles, J., Carr, L. D., Castin, Y., and Salomon, C. *Science* **296**(5571), 1290–1293 May (2002).
- [62] Strecker, K. E., Partridge, G. B., Truscott, A. G., and Hulet, R. G. *Nature* **417**(6885), 150–153 May (2002).
- [63] Tinkham, M. *Introduction to superconductivity*. McGraw-Hill Publishing Co, (1996).
- [64] Gross, E. *Il Nuovo Cimento (1955-1965)* **20**(3), 454–477 May (1961).
- [65] Pitaevsk, L. P. *Soviet Physics JETP-USSR* **13**(2) (1961).
- [66] Dalfovo, F., Giorgini, S., Pitaevskii, L. P., and Stringari, S. *Reviews of Modern Physics* **71**(3), 463–512 Apr (1999).
- [67] Leggett, A. J. *Reviews of Modern Physics* **73**(2), 307–356 Apr (2001).
- [68] Pethick, C. J. and Smith, H. *Bose-Einstein Condensation in Dilute Gases*. Cambridge University Press, (2008).

Bibliography

- [69] Pitaevskii, L. and Stringari, S. *Bose-Einstein Condensation (The International Series of Monographs on Physics)*. Oxford University Press, USA, June (2003).
- [70] Jaksch, D., Bruder, C., Cirac, J. I., Gardiner, C. W., and Zoller, P. *Physical Review Letters* **81**(15), 3108–3111 Oct (1998).
- [71] Greiner, M., Mandel, O., Esslinger, T., Hansch, T. W., and Bloch, I. *Nature* **415**(6867), 39–44 January (2002).
- [72] Paredes, B., Widera, A., Murg, V., Mandel, O., Fölling, S., Cirac, I., Shlyapnikov, G. V., Hansch, T. W., and Bloch, I. *Nature* **429**(6989), 277–281 May (2004).
- [73] Kinoshita, T., Wenger, T., and Weiss, D. S. *Science* **305**(5687), 1125–1128 August (2004).
- [74] Hadzibabic, Z., Krüger, P., Cheneau, M., Battelier, B., and Dalibard, J. *Nature* **441**(7097), 1118–1121 June (2006).
- [75] Schweikhard, V., Tung, S., and Cornell, E. A. *Physical Review Letters* **99**(3), 030401 Jul (2007).
- [76] Fano, U. *Physical Review Online Archive (Prola)* **124**(6), 1866–1878 Dec (1961).
- [77] Feshbach, H. *Annals of Physics* **5**(4), 357–390 December (1958).
- [78] Feshbach, H. *Annals of Physics* **19**(2), 287–313 August (1962).
- [79] Cornish, S. L., Claussen, N. R., Roberts, J. L., Cornell, E. A., and Wieman, C. E. *Physical Review Letters* **85**(9), 1795–1798 Aug (2000).
- [80] Donley, E. A., Claussen, N. R., Cornish, S. L., Roberts, J. L., Cornell, E. A., and Wieman, C. E. *Nature* **412**(6844), 295–299 July (2001).
- [81] Roberts, J. L., Claussen, N. R., Cornish, S. L., Donley, E. A., Cornell, E. A., and Wieman, C. E. *Physical Review Letters* **86**(19), 4211–4214 May (2001).
- [82] Papp, S. B., Pino, J. M., Wild, R. J., Ronen, S., Wieman, C. E., Jin, D. S., and Cornell, E. A. *Physical Review Letters* **101**(13), 135301 (2008).

Bibliography

- [83] Pollack, S. E., Dries, D., Junker, M., Chen, Y. P., Corcovilos, T. A., and Hulet, R. G. *Physical Review Letters* **102**(9), 090402 (2009).
- [84] Kraemer, T., Mark, M., Waldburger, P., Danzl, J. G., Chin, C., Engeser, B., Lange, A. D., Pilch, K., Jaakkola, A., Nägerl, H. C., and Grimm, R. *Nature* **440**(7082), 315–318 March (2006).
- [85] Pollack, S. E., Dries, D., and Hulet, R. G. *Science* **326**(5960), 1683–1685 December (2009).
- [86] Ferlaino, F., Knoop, S., Berninger, M., Harm, W., Dchar39Incao, J. P., Nägerl, H. C., and Grimm, R. *Physical Review Letters* **102**(14), 140401 Apr (2009).
- [87] Chang, M.-S., Qin, Q., Zhang, W., You, L., and Chapman, M. S. *Nature Physics* **1**(2), 111–116 October (2005).
- [88] Schmaljohann, H., Erhard, M., Kronjäger, J., Sengstock, K., and Bongs, K. *Applied Physics B* **79**(8), 1001–1007 December (2004).
- [89] Hall, D. S., Matthews, M. R., Wieman, C. E., and Cornell, E. A. *Physical Review Letters* **81**(8), 1543–1546 Aug (1998).
- [90] Matthews, M. R., Anderson, B. P., Haljan, P. C., Hall, D. S., Holland, M. J., Williams, J. E., Wieman, C. E., and Cornell, E. A. *Physical Review Letters* **83**(17), 3358–3361 Oct (1999).
- [91] Stamper-Kurn, D. M., Miesner, H. J., Chikkatur, A. P., Inouye, S., Stenger, J., and Ketterle, W. *Physical Review Letters* **83**(4), 661–665 Jul (1999).
- [92] Higbie, J. M., Sadler, L. E., Inouye, S., Chikkatur, A. P., Leslie, S. R., Moore, K. L., Savalli, V., and Kurn, D. M. S. *Physical Review Letters* **95**(5), 050401 Jul (2005).
- [93] Sadler, L. E., Higbie, J. M., Leslie, S. R., Vengalattore, M., and Stamper-Kurn, D. M. *Nature* **443**(7109), 312–315 September (2006).
- [94] Liu, Y., Jung, S., Maxwell, S. E., Turner, L. D., Tiesinga, E., and Lett, P. D. *Physical Review Letters* **102**(12), 125301 (2009).
- [95] Kuwamoto, T., Araki, K., Eno, T., and Hirano, T. *Physical Review A* **69**(6), 063604 Jun (2004).

Bibliography

- [96] Widera, A., Gerbier, F., Fölling, S., Gericke, T., Mandel, O., and Bloch, I. *Physical Review Letters* **95**(19), 190405 Nov (2005).
- [97] Widera, A., Gerbier, F., Folling, S., Gericke, T., Mandel, O., and Bloch, I. *New J. Phys.* **8**(8), 152 August (2006).
- [98] Mur-Petit, J., Guilleumas, M., Polls, A., Sanpera, A., Lewenstein, M., Bongs, K., and Sengstock, K. *Physical Review A* **73**(1), 013629 (2006).
- [99] Kronjäger, J., Becker, C., Navez, P., Bongs, K., and Sengstock, K. *Physical Review Letters* **97**(11), 110404 September (2006).
- [100] Black, A. T., Gomez, E., Turner, L. D., Jung, S., and Lett, P. D. *Physical Review Letters* **99**(7), 070403 (2007).
- [101] Mertes, K., Merrill, J., Carretero-González, R., Frantzeskakis, D., Kevrekidis, P., and Hall, D. *Physical Review Letters* **99**(19), 190402 November (2007).
- [102] Klempt, C., Topic, O., Gebreyesus, G., Scherer, M., Henninger, T., Hyllus, P., Ertmer, W., Santos, L., and Arlt, J. J. *Physical Review Letters* **103**(19), 195302 (2009).
- [103] Leslie, S. R., Guzman, J., Vengalattore, M., Sau, J. D., Cohen, M. L., and Kurn, D. M. S. *Physical Review A* **79**(4), 043631 (2009).
- [104] Leanhardt, A. E., Shin, Y., Kielpinski, D., Pritchard, D. E., and Ketterle, W. *Physical Review Letters* **90**(14), 140403 Apr (2003).
- [105] Ho, T. L. and Yip, S. K. *Physical Review Letters* **84**(18), 4031–4034 May (2000).
- [106] Mueller, E., Ho, T.-L., Ueda, M., and Baym, G. *Physical Review A* **74**(3), 033612 September (2006).
- [107] Ho, T. L. *Physical Review Letters* **81**(4), 742–745 Jul (1998).
- [108] Ohmi, T. and Machida, K. *Journal of the Physical Society of Japan* **67**(6), 1822–1825 (1998).
- [109] Ho, T. L. and Yin, L. *Physical Review Letters* **84**(11), 2302–2305 Mar (2000).
- [110] Josephson, B. *Physics Letters* **1**(7), 251–253 July (1962).

Bibliography

- [111] Zhang, W., Zhou, D. L., Chang, M. S., Chapman, M. S., and You, L. *Physical Review A* **72**(1), 013602 Jul (2005).
- [112] Koashi, M. and Ueda, M. *Physical Review Letters* **84**(6), 1066–1069 Feb (2000).
- [113] Law, C. K., Pu, H., and Bigelow, N. P. *Physical Review Letters* **81**(24), 5257–5261 Dec (1998).
- [114] He, Y. Z., Chen, Z. F., Li, Z. B., and Bao, C. G. *Physical Review A* **80**(2), 023620 (2009).
- [115] Zhai, Q., Chang, L., Lu, R., and You, L. *Physical Review A* **79**(4), 043608 (2009).
- [116] Plimak, L., Weis, C., Walser, R., and Schleich, W. *Optics Communications* **264**(2), 311–320 August (2006).
- [117] Diener, R. B. and Ho, T.-L. (2006).
- [118] Pu, H., Law, C. K., Raghavan, S., Eberly, J. H., and Bigelow, N. P. *Physical Review A* **60**(2), 1463–1470 Aug (1999).
- [119] Chang, L., Zhai, Q., Lu, R., and You, L. *Physical Review Letters* **99**(8), 080402 August (2007).
- [120] Luo, M., Bao, C., and Li, Z. *Physical Review A* **77**(4), 043625 April (2008).
- [121] Gawryluk, K., Brewczyk, M., Gajda, M., and Rzazewski, K. *Physical Review A* **76**(1), 013616 July (2007).
- [122] Takahashi, M., Ghosh, S., Mizushima, T., and Machida, K. *Physical Review Letters* **98**(26), 260403 June (2007).
- [123] Zhou, F. *Physical Review Letters* **87**(8), 080401 Aug (2001).
- [124] Song, J. L., Semenov, G., and Zhou, F. *Physical Review Letters* **98**(16), 160408 April (2007).
- [125] Semenov, G. and Zhou, F. *Physical Review Letters* **98**(10), 100401 March (2007).
- [126] Mermin, N. D. *Rev. Mod. Phys.* **51**(3), 591–648 Jul (1979).

Bibliography

- [127] Cui, X., Wang, Y., and Zhou, F. *Physical Review A* **78**(5), 050701 Nov (2008).
- [128] Demler, E. and Zhou, F. *Physical Review Letters* **88**(16), 163001 Apr (2002).
- [129] Zhou, F. and Snoek, M. *Annals of Physics* **308**(2), 692–738 December (2003).
- [130] Imambekov, A., Lukin, M., and Demler, E. *Physical Review A* **68**(6), 063602 Dec (2003).
- [131] Zhou, F. *EPL (Europhysics Letters)* **63**(4), 505–511 (2003).
- [132] Snoek, M. and Zhou, F. *Physical Review B* **69**(9), 094410 Mar (2004).
- [133] Zhou, F., Snoek, M., Wiemer, J., and Affleck, I. *Physical Review B* **70**(18), 184434 Nov (2004).
- [134] Zhou, F. and Semenoff, G. W. *Physical Review Letters* **97**(18), 180411 (2006).
- [135] Snoek, M., Song, J. L., and Zhou, F. *Physical Review A* **80**(5), 053618 November (2009).
- [136] Powell, S. and Sachdev, S. *Physical Review A* **76**(3), 033612 September (2007).
- [137] Song, J. L. and Zhou, F. *Physical Review A* **77**(3), 033628 Mar (2008).
- [138] Koch, T., Lahaye, T., Metz, J., Frohlich, B., Griesmaier, A., and Pfau, T. *Nature Physics* **4**(3), 218–222 February (2008).
- [139] Vengalattore, M., Leslie, S. R., Guzman, J., and Stamper-Kurn, D. M. *Physical Review Letters* **100**(17), 170403 May (2008).
- [140] Crubellier, A., Dulieu, O., Masnou-Seeuws, F., Elbs, M., Knöckel, H., and Tiemann, E. *The European Physical Journal D - Atomic, Molecular, Optical and Plasma Physics* **6**(2), 211–220 May (1999).
- [141] Ciobanu, C. V., Yip, S. K., and Ho, T. L. *Physical Review A* **61**(3), 033607 Feb (2000).
- [142] Klausen, N. N., Bohn, J. L., and Greene, C. H. *Physical Review A* **64**(5), 053602 Oct (2001).

Bibliography

- [143] van Kempen, E. G. M., Kokkelmans, Heinzen, D. J., and Verhaar, B. J. *Physical Review Letters* **88**(9), 093201 Feb (2002).
- [144] Barnett, R., Turner, A., and Demler, E. *Physical Review Letters* **97**(18), 180412 (2006).
- [145] Barnett, R., Turner, A., and Demler, E. *Physical Review A* **76**(1), 013605 July (2007).
- [146] Mermin, N. D. and Stare, C. *Physical Review Letters* **30**(22), 1135–1138 May (1973).
- [147] Mermin, N. D. *Physical Review A* **9**(2), 868–872 Feb (1974).
- [148] Halperin, B. I., Lubensky, T. C., and Ma, S. K. *Physical Review Letters* **32**(6), 292–295 Feb (1974).
- [149] Thouless, D. J. *Topological Quantum Numbers in Nonrelativistic Physics*. World Scientific Pub Co Inc, (1998).
- [150] Andrews, M. R., Kurn, D. M., Miesner, H. J., Durfee, D. S., Townsend, C. G., Inouye, S., and Ketterle, W. *Physical Review Letters* **79**(4), 553–556 Jul (1997).
- [151] Miesner, H. J., Kurn, D. M. S., Stenger, J., Inouye, S., Chikkatur, A. P., and Ketterle, W. *Physical Review Letters* **82**(11), 2228–2231 Mar (1999).
- [152] Hall, D. S., Matthews, M. R., Ensher, J. R., Wieman, C. E., and Cornell, E. A. *Physical Review Letters* **81**(8), 1539–1542 Aug (1998).
- [153] Tsai, C. C., Freeland, R. S., Vogels, J. M., Boesten, H. M. J. M., Verhaar, B. J., and Heinzen, D. J. *Physical Review Letters* **79**(7), 1245–1248 Aug (1997).
- [154] Wynar, R., Freeland, R. S., Han, D. J., Ryu, C., and Heinzen, D. J. *Science* **287**(5455), 1016–1019 February (2000).
- [155] Fölling, S., Gerbier, F., Widera, A., Mandel, O., Gericke, T., and Bloch, I. *Nature* **434**(7032), 481–484 March (2005).
- [156] Campbell, G. K., Mun, J., Boyd, M., Medley, P., Leanhardt, A. E., Marcassa, L. G., Pritchard, D. E., and Ketterle, W. *Science* **313**(5787), 649–652 August (2006).

Bibliography

- [157] Stöferle, T., Moritz, H., Schori, C., Köhl, M., and Esslinger, T. *Physical Review Letters* **92**(13), 130403 Mar (2004).
- [158] Grimm, R., Weidemuller, M., and Ovchinnikov, Y. B. **42**, 95–170 (2000).
- [159] Deutsch, I. H. and Jessen, P. S. *Phys. Rev. A* **57**(3), 1972–1986 Mar (1998).
- [160] McKay, D. and DeMarco, B. Nov (2009).
- [161] Turner, A., Barnett, R., Demler, E., and Vishwanath, A. *Physical Review Letters* **98**(19), 190404 May (2007).
- [162] Polkovnikov, A., Altman, E., and Demler, E. *Proceedings of the National Academy of Sciences of the United States of America* **103**(16) (2006).
- [163] Haljan, P. C., Coddington, I., Engels, P., and Cornell, E. A. *Physical Review Letters* **87**(21), 210403 Nov (2001).
- [164] Feder, D. L., Svidzinsky, A. A., Fetter, A. L., and Clark, C. W. *Physical Review Letters* **86**(4), 564–567 Jan (2001).
- [165] Dalfovo, F. and Stringari, S. *Physical Review A* **63**(1), 011601 Dec (2000).
- [166] Tsubota, M., Kasamatsu, K., and Ueda, M. *Physical Review A* **65**(2), 023603 Jan (2002).
- [167] Lundh, E., Martikainen, J. P., and Suominen, K. A. *Physical Review A* **67**(6), 063604 Jun (2003).
- [168] Parker, N. G. and Adams, C. S. *Physical Review Letters* **95**(14), 145301 Sep (2005).
- [169] Leggett, A. J. *Reviews of Modern Physics* **47**(2), 331–414 (1975).
- [170] Salomaa, M. M. and Volovik, G. E. *Reviews of Modern Physics* **59**(3), 533–613 Jul (1987).
- [171] Chandrasekhar, S. *Liquid Crystals*. Cambridge University Press, 2 edition, January (1993).
- [172] Su, W. P., Schrieffer, J. R., and Heeger, A. J. *Physical Review B* **22**(4), 2099–2111 Aug (1980).

Bibliography

- [173] Tsui, D. C., Stormer, H. L., and Gossard, A. C. *Physical Review Letters* **48**(22), 1559–1562 May (1982).
- [174] Laughlin, R. B. *Physical Review Letters* **50**(18), 1395–1398 May (1983).
- [175] Jackiw, R. and Rebbi, C. *Physical Review D* **13**(12), 3398–3409 Jun (1976).
- [176] Anderson, P. W. *Science* **235**(4793), 1196–1198 March (1987).
- [177] Rokhsar, D. S. and Kivelson, S. A. *Physical Review Letters* **61**(20), 2376–2379 Nov (1988).
- [178] Wen, X. G. *Physical Review B* **43**(13), 11025–11036 May (1991).
- [179] Read, N. and Sachdev, S. *Physical Review Letters* **66**(13), 1773–1776 Apr (1991).
- [180] Senthil, T. and Fisher, M. P. A. *Physical Review B* **62**(12), 7850–7881 Sep (2000).
- [181] Moessner, R. and Sondhi, S. L. *Physical Review Letters* **86**(9), 1881–1884 Feb (2001).
- [182] Bonn, D. A., Wynn, J. C., Gardner, B. W., Lin, Y.-J., Liang, R., Hardy, W. N., Kirtley, J. R., and Moler, K. A. *Nature* **414**(6866), 887–889 December (2001).
- [183] Kitaev, A. *Annals of Physics* **303**(1), 2–30 January (2003).
- [184] Fetter, A. L. and Svidzinsky, A. A. *Journal of Physics: Condensed Matter* **13**(12), R135–R194 (2001).
- [185] Leonhardt, U. and Volovik, G. *JETP Letters* **72**(2), 46–48 July (2000).
- [186] Isoshima, T. and Machida, K. *Physical Review A* **66**(2), 023602 Aug (2002).
- [187] Kita, T., Mizushima, T., and Machida, K. *Physical Review A* **66**(6), 061601 Dec (2002).
- [188] Mueller, E. J. and Ho, T. L. *Physical Review Letters* **88**(18), 180403 Apr (2002).

- [189] Kasamatsu, K., Tsubota, M., and Ueda, M. *Physical Review Letters* **91**(15), 150406 Oct (2003).
- [190] Schweikhard, V., Coddington, I., Engels, P., Tung, S., and Cornell, E. A. *Physical Review Letters* **93**(21), 210403 Nov (2004).
- [191] Mukerjee, S., Xu, C., and Moore, J. E. *Physical Review Letters* **97**(12), 120406 Sep (2006).
- [192] Hubbard, J. *Physical Review Letters* **3**(2), 77–78 Jul (1959).
- [193] Lammert, P. E., Rokhsar, D. S., and Toner, J. *Physical Review Letters* **70**(11), 1650–1653 Mar (1993).
- [194] Fradkin, E. and Shenker, S. H. *Physical Review D* **19**(12), 3682–3697 Jun (1979).
- [195] Wilson, K. G. *Physical Review D* **10**(8), 2445–2459 Oct (1974).
- [196] Feder, D. L., Clark, C. W., and Schneider, B. I. *Physical Review A* **61**(1), 011601 Dec (1999).
- [197] Mizushima, T., Isoshima, T., and Machida, K. *Physical Review A* **64**(4), 043610 Sep (2001).
- [198] Simula, T. P., Virtanen, S. M. M., and Salomaa, M. M. *Physical Review A* **66**(3), 035601 Sep (2002).
- [199] Ji, A. C., Liu, W. M., Song, J. L., and Zhou, F. *Physical Review Letters* **101**(1), 010402 July (2008).
- [200] Vinen, W. F. *Nature* **181**(4622) (1958).
- [201] Zambelli, F. and Stringari, S. *Physical Review Letters* **81**(9), 1754–1757 Aug (1998).
- [202] Chevy, F., Madison, K. W., and Dalibard, J. *Physical Review Letters* **85**(11), 2223–2227 Sep (2000).

Appendix A

Band Structure in Optical Lattices

An optical lattice is made of pairs of counter propagating laser beams. The standing wave pattern formed by laser beams can provide a periodical potential for atoms loaded in optical lattices. In a simple theoretical model, the potential strength is proportional to the local intensity of the electric field which has a sinusoidal spatial dependence. For a cubic lattice in 3D, the following periodical potential is used in the calculation of the band structure.

$$V(\mathbf{r}) = V_0 \left[\sin^2 \left(\frac{2\pi}{\lambda} x \right) + \sin^2 \left(\frac{2\pi}{\lambda} y \right) + \sin^2 \left(\frac{2\pi}{\lambda} z \right) \right] \quad (\text{A.1})$$

Three counter-propagating laser beams are slightly mismatched in their frequencies to avoid interference between laser fields of different directions. λ is the wavelength of the laser, and V_0 is the depth of optical lattice which is proportional to the intensity of laser fields. V_0 is often measured in units of the recoil energy associated with the laser beams as $E_R = \frac{\hbar^2}{2m\lambda^2}$. Here for simplicity we assume V_0 is the same for all three directions. In experiments they can be varied independently to generate other geometries such as quasi 2D to support the system studied in Chap.5.

A single atom loaded in an optical lattice can be described by the Schrodinger equation:

$$\left[-\frac{\hbar^2 \nabla^2}{2m} + V(r) \right] \psi(r) = E\psi(r). \quad (\text{A.2})$$

The solution to the above problem has the form of Bloch waves and can be labeled by a crystal momentum \mathbf{k} and a band index n .

$$\psi_{\alpha}(\mathbf{r}) = e^{i\mathbf{k}\cdot\mathbf{r}} u_{n,\mathbf{k}}(\mathbf{r}) \quad (\text{A.3})$$

$$E = E_n(\mathbf{k}) \quad (\text{A.4})$$

Here $u_{n,\mathbf{k}}(\mathbf{r})$ is a periodic function with a period $\lambda/2$ and is normalized as

$$\int_{\text{u.c.}} dr |u_{n,k}^2(r)| = 1. \quad (\text{A.5})$$

Here the integration is performed within the unit cell(u.c.).

The Wannier function forming a convenient basis in deep optical lattices can be constructed from Bloch waves as

$$w_{n,R}(r) = \int_{k \in \text{BZ}} dk e^{ik(r-R)} u_{n,k}(r). \quad (\text{A.6})$$

It can be easily shown that Wannier functions labeled by the localization center R and the band index n forms an orthogonal basis,

$$\int_{\text{u.c.}} dr w_{n,R}^*(r) w_{n',R'}(r) = \delta_{R,R'} \delta_{n,n'}. \quad (\text{A.7})$$

In the second quantization form one can also introduce creation (annihilation) operators $\psi_{n,R}^\dagger$ ($\psi_{n,R}$) for Wannier functions

$$\begin{aligned} \psi^\dagger(r) &= \sum_{nR} w_{n,R}(r) \psi_{n,R}^\dagger \\ \psi_{n,R}^\dagger &= \int d\mathbf{r} w_{n,R}^*(r) \psi^\dagger(r) \\ [\psi_{n,R}, \psi_{n',R'}^\dagger] &= \delta_{n,n'} \delta_{R,R'} \end{aligned} \quad (\text{A.8})$$

One can rewrite the following many-body Hamiltonian of interacting bosons by using the expansion given in Eq.A.8:

$$\begin{aligned} H &= \int d\mathbf{r} \left[\psi^\dagger(r) \left(-\frac{\hbar^2 \nabla^2}{2m} - \mu + V(r) \right) \psi(r) \right. \\ &\quad \left. + \frac{2\pi \hbar^2 a_s}{m} \psi^\dagger(r) \psi^\dagger(r) \psi(r) \psi(r) \right] \\ &\simeq -t_L \sum_{\langle RR' \rangle} \left(\psi_{R'}^\dagger \psi_R + \text{h.c.} \right) - \mu_L \sum_R \psi_R^\dagger \psi_R \\ &\quad + \frac{a_L}{2} \sum_R \psi_R^\dagger \psi_R^\dagger \psi_R \psi_R. \end{aligned} \quad (\text{A.9})$$

When only the lowest band is concerned we can obtain the above single band Hubbard model in which only the leading terms are kept. Other terms such as next-nearest neighbor hopping and interaction from atoms occupying different sites turns out to be much smaller than the leading terms in deep optical lattices.

Such a single band model serves as starting point of many calculations in this thesis. Two important parameters of this model t_L and a_L are given

by

$$\begin{aligned}
 t_L &= \int_{\text{u.c.}} d\mathbf{r} w_{n=0,R}^*(r) w_{n=0,R'}(r) \\
 &= \int d\mathbf{k} E_{n=0}(\mathbf{k}) e^{i\mathbf{k}\cdot(\mathbf{R}-\mathbf{R}')} \\
 a_L &= \frac{4\pi a_s}{m} \int_{\text{u.c.}} d\mathbf{r} |w_{n=0,R}^4(r)|. \tag{A.10}
 \end{aligned}$$

Using the methods outlined above, one can determine t_L and a_L as a function of potential depth V in optical lattice, as shown in Fig.4.1.

Notice that in Eq.A.6 there is undetermined k -dependent phase factor in the Bloch waves $u_{n,\mathbf{k}}(\mathbf{r})$. The Wannier function actually depends on this choice. In our calculation, we choose the so-called maximum localized Wannier function which can reduce overlapping terms such as $\int dr |w_{n,R}^2 w_{n,R'}^2|$ that may appear in the lattice model.

Appendix B

The β -function of the Nonlinear Sigma Model

We derive the β function of $O(3)$ nonlinear sigma model in this section. Let's consider a unit vector $|\vec{s}| = 1$ which has three components (s_1, s_2, s_3) .

$$H = \frac{J}{2} \int d^d \mathbf{x} (\nabla \vec{s}(\mathbf{x}))^2 \quad (\text{B.1})$$

It is convenient to rescale the Hamiltonian by introducing a coupling constant $g = \frac{1}{\beta J}$,

$$\beta H = \frac{1}{2g} \int d^d \mathbf{x} (\nabla \vec{s}(\mathbf{x}))^2 \quad (\text{B.2})$$

The coupling constant has a dimension of $(\text{length})^{d-2}$, and one can also introduce a dimensionless constant u as

$$g = u a_0^{d-2}, \quad (\text{B.3})$$

here a is the smallest length scale in the system and it is inverse proportional to the momentum cutoff Λ .

Let's consider small fluctuations around the mean field ground state $s = (1, 0, 0)$ in terms of two small parameters s_3 and θ :

$$s_1 = \sqrt{1 - s_3^2} \cos(\theta) \quad (\text{B.4})$$

$$s_2 = \sqrt{1 - s_3^2} \sin(\theta) \quad (\text{B.5})$$

$$(\text{B.6})$$

The energy density \mathcal{H} can be written in terms of θ and s_3 as:

$$\beta \mathcal{H}(x) = \frac{1}{2g} \left[(\nabla s_3)^2 + (1 - s_3^2) (\nabla \theta)^2 + \frac{(s_3 \nabla s_3)^2}{1 - s_3^2} \right] \quad (\text{B.7})$$

Appendix B. The β -function of the Nonlinear Sigma Model

Notice the fluctuations of the s_3 field has a magnitude of $\sim \sqrt{g}$. Hence we can rescale the s_3 field as

$$\sqrt{g}\psi = s_3, \quad (\text{B.8})$$

and expand the Hamiltonian according to the orders of g

$$\mathcal{H}(x) \simeq \frac{1}{2}(\nabla\psi)^2 + \frac{1}{2g}(\nabla\theta)^2 - \frac{1}{2}\psi^2(\nabla\theta)^2 \quad (\text{B.9})$$

$$+ \frac{g}{2}(\psi\nabla\psi)^2 + \frac{g^2}{2}\psi^2(\psi\nabla\psi)^2 + O(g^3) \quad (\text{B.10})$$

Let's now perform the integration over the ‘‘fast’’ fields or fields with momentum within the shell $b\Lambda < |p| < \Lambda$. To obtain the leading order contributions in terms of g , we can assume that the θ field is smooth and we only need to integrate over the ψ field within the shell:

$$\int_{b\Lambda < |p| < \Lambda} \mathcal{D}\psi e^{-\beta H[\psi, \theta]} = \quad (\text{B.11})$$

$$\int_{b\Lambda < |p| < \Lambda} \mathcal{D}\psi(p) e^{-\frac{1}{2} \int d^d x \left[(\nabla\psi)^2 + \frac{1}{g}(\nabla\theta)^2 - \psi^2(\nabla\theta)^2 + O(g) \right]} \quad (\text{B.12})$$

After the Fourier transformation of ψ field, we can perform a Gaussian integral and then rewrite the result in the exponential form.

$$\int_{b\Lambda < |p| < \Lambda} \mathcal{D}\psi(p) e^{-\frac{1}{2} \int \frac{d^d p}{(2\pi)^d} [p^2 - (\nabla\theta)^2] |\psi(p)|^2} \quad (\text{B.13})$$

$$\simeq \prod_{b\Lambda < |p| < \Lambda} \left[\frac{2\pi}{p^2 - (\nabla\theta)^2} \right]^{\frac{1}{2}} \quad (\text{B.14})$$

$$\simeq \exp \left[\frac{1}{2} \int_{b\Lambda < |p| < \Lambda} \frac{d^d p}{(2\pi)^d} \log \frac{2\pi}{p^2 - (\nabla\theta)^2} \right] \quad (\text{B.15})$$

$$\simeq \exp \left[\frac{1}{2} \int_{b\Lambda < |p| < \Lambda} \frac{d^d p}{(2\pi)^d} \left(\log \frac{2\pi}{p^2} + \frac{(\nabla\theta)^2}{p^2} \right) \right] \quad (\text{B.16})$$

The coarse grained Hamiltonian \mathcal{H}' up to the first order of g is

$$\begin{aligned} \beta\mathcal{H}'(x) &= -\frac{1}{2} \int_{b\Lambda < |p| < \Lambda} \frac{d^d p}{(2\pi)^d} \log \frac{2\pi}{p^2} + \frac{1}{2}(\nabla\psi)^2 - \frac{1}{2}\psi^2(\nabla\theta)^2 \\ &+ \frac{1}{2} \left[\frac{1}{g} - \int_{b\Lambda < |p| < \Lambda} \frac{d^d p}{(2\pi)^d} \frac{1}{p^2} \right] (\nabla\theta)^2 + O(g) \end{aligned} \quad (\text{B.17})$$

Appendix B. The β -function of the Nonlinear Sigma Model

When we rescale the Hamiltonian, the new cutoff Λ' is reduced and the new length scale a' is increased ($b < 1$), indicating the system is dilated.

$$\Lambda' = b\Lambda, a'_0 = \frac{a_0}{b} \quad (\text{B.18})$$

The coupling term g' in the coarse grained Hamiltonian H' can be written as:

$$\frac{1}{u'a_0^{d-2}} = \frac{1}{ua_0^{d-2}} - \int_{b\Lambda < |p| < \Lambda} \frac{d^d p}{(2\pi)^d} \frac{1}{p^2} \quad (\text{B.19})$$

By differentiating the above equation with the length scale a_0 , one can obtain the renormalization group function or β -function for the coupling constant u .

$$\begin{aligned} \beta(u) &= a_0 \frac{du}{da_0} \\ &= (2-d)u + \frac{u^2}{2\pi} + O(u^3) \end{aligned} \quad (\text{B.20})$$

The β function of u is very different for $d \leq 2$ and $d > 2$. In the former cases, the coupling constant goes to infinite as one increases the length scale indicating the spins are always short-ranged ($T > 0$). On the other hand, in $d > 2$ cases, the system has two different phases separated by the fixed point u_c ($\beta(u_c) = 0$).

At $d = 2$, one can also estimate the spin correlation length ξ by solving the equation of the beta function:

$$\xi = a_0 \exp\left(\frac{2\pi}{u}\right) = a_0 \exp\left(\frac{2\pi J}{T}\right), \quad (\text{B.21})$$

here a_0 and J are the lattice constant and the coupling constant of the lattice model.